Stress Corrosion Cracking Behavior of Oxide Dispersion Strengthened Ferritic Steel in Supercritical Pressurized Water

Hwanil Je

Graduate School of Energy Science

Kyoto University

2013

Contents

Chapter 3. Stress Corrosion Cracking Susceptibility of ODS ferritic steel in Supercritical Pressurized
        Water Dissolved with Different Hydrogen and Oxygen Contents

Chapter 4. Stress Corrosion Cracking Behavior of Austenitic Stainless Steel and Ferritic/Martensitic
        Steel in Different Water Chemistry of Supercritical Pressurized Water.

Chapter 1

Introduction

1.1 Current status of global energy and its prediction

The World Energy Outlook 2012 (WEO2012) of International Energy Agency (IEA) [1] suggested the New Policies Scenario of world energy, because the global energy map is changing by the resurgence in oil and gas production in the United States, the retreat from nuclear power in some countries, continued rapid growth in the use of wind and solar technologies and by the global spread of unconventional gas production. According to the outlook, global energy demand grows by more than one-third over the period to 2035 in the New Policies Scenario, with China, India and the Middle East accounting for 60% of the increase. The world population may have grown to 9 billion people, the emerging economies of Brazil, Russia, India and China may well be the world's largest economies, and as their wealth increases, their energy demand will be added to the current increasing world demand. Existing supplies of fossil fuels are limited, with some already predicting that the peak of oil production has been reached. Added to this, over-dependence and over-use of these fuels has led to the detrimental global warming and climate change we experience today.

BP Statistical Review of World Energy 2013 [2] announced that world primary energy consumption has increased, as shown in Fig. 1.1. With the assumed expansion of the global economy and an increase of the world's population, more energy will be needed to satisfy growing demand for energy services.
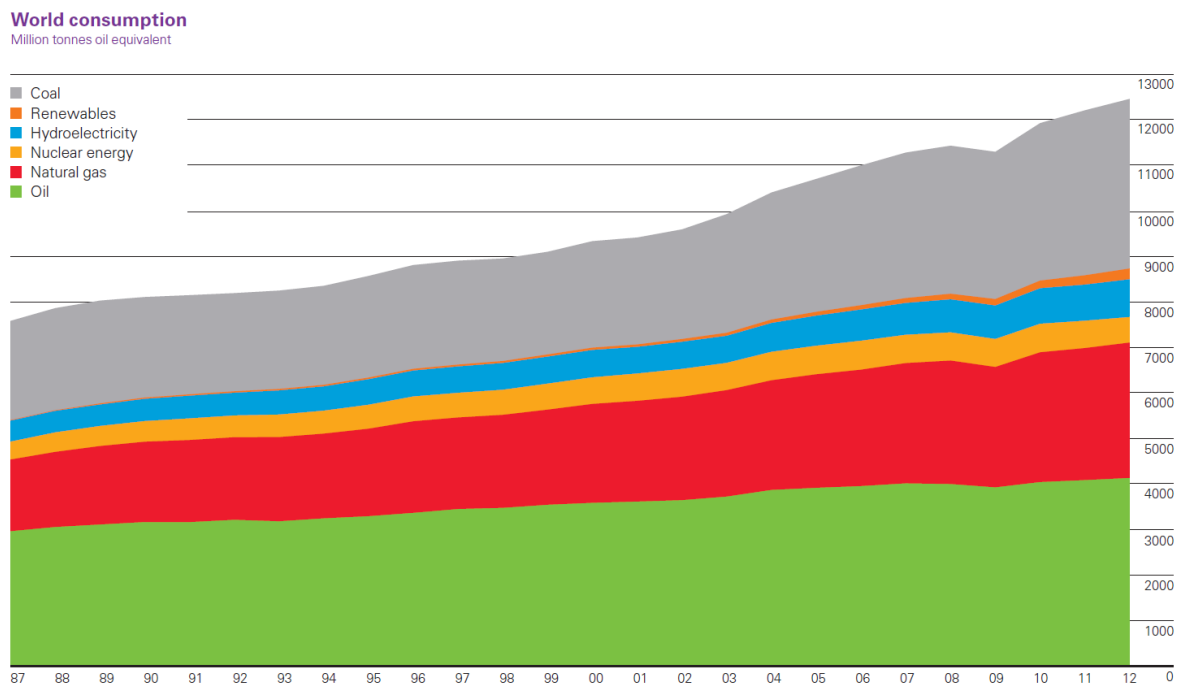
Fig. 1.1. The world primary energy consumption with historical data from 1987 to 2012.

1.2 The necessity of nuclear energy

World-wide energy is currently depends on fossil fuels about 80% of all of the energy. With respect to global warming and energy depletion, each country has to make efforts to reduce the consumption of fossil fuels. The dramatic increase in world-wide demand for energy and its environmental problems are expected in nowadays and the future have stimulated international cooperation to consider how to meet future energy needs while reserving and improving the environment. This concern has led to nuclear energy and it is well described at Fig. 1.2 and 1.3. Although some governments—including Japan, Germany, Switzerland and Italy—have slowed or halted nuclear energy production as a result of the Fukushima accident, both EIA (Fig. 1.2) and IEA (Fig. 1.3) predict that overall production will likely expand since countries still face the same challenges over energy security and reducing global greenhouse gas emissions. In other words, both EIA and IEA estimate positive growth for nuclear energy in latest energy outlook report. These challenges highlight the important role that nuclear energy plays in providing domestic, carbon-free, base load electricity [3], because large amounts of energy can be produced with nuclear reactors without the anti- environmental effects accompanied by the use of fossil fuel products. Although renewable energy sources (solar photovoltaic, biomass, wind power etc.) may offer similar beneficial effects, concerns exist on economic efficiency and reliability when they are used for base-load power generation. The technology and economic reliability of nuclear energy have been demonstrated by the practical reactor operation throughout the world today.
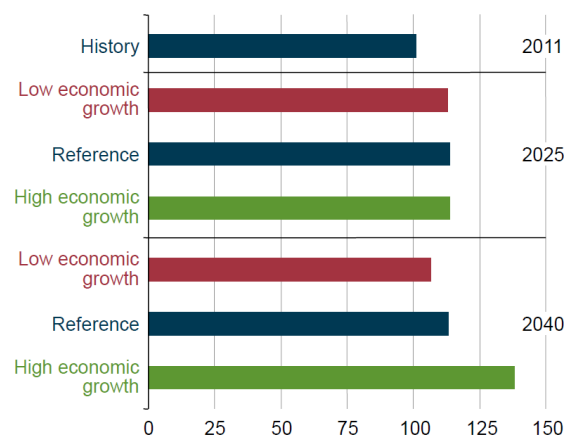
Fig. 1.2. Electricity generating capacity at U.S. nuclear power plants in three cases, 2011, 2025 and 2040 (gigawatts), Source : Annual Energy Outlook 2013: with projections to 2040 by U.S Energy Information Administraion (EIA)
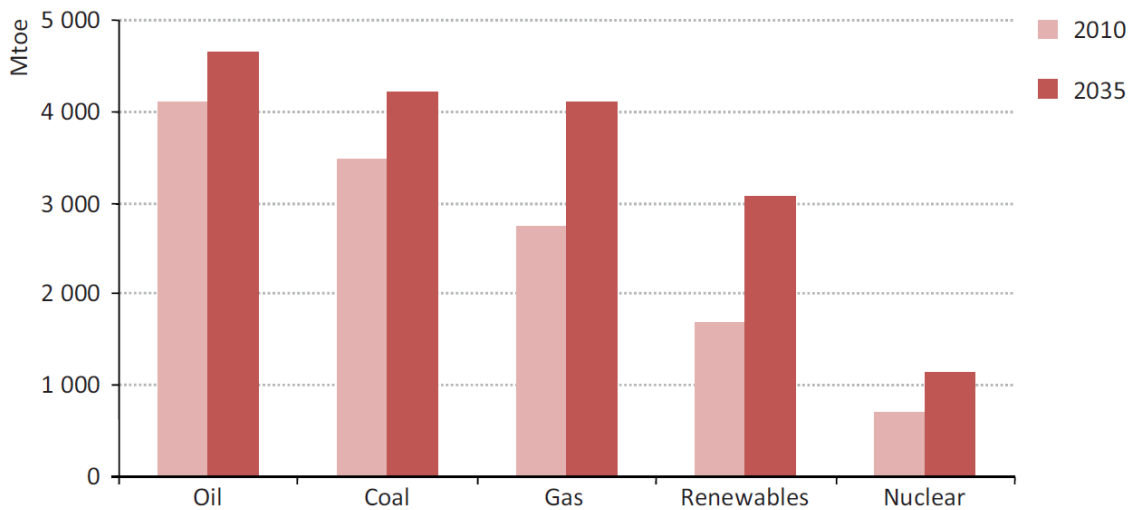
Fig. 1.3. World Primary energy demand by fuel in the New Policies Scenario, Source : World Energy Outlook 2012 of International Energy Agency (IEA)

1.3 Nuclear energy systems

1.3.1 Fusion reactors

Nuclear fusion is one of promising options for generating large amounts of carbon-free energy in the future. If one sentence sums up the fusion reactor, it is "bringing the power of the sun to earth." Because fusion is the process that heats the Sun and all other stars, where atomic nuclei collide together and release energy. To get energy from fusion, gas from a combination of types of hydrogen – deuterium and tritium – is heated to very high temperatures (100 million degrees Celsius). One way to achieve these conditions is a method called 'magnetic confinement' – controlling the hot gas (known as a plasma) with strong magnets. Although many fusion reactor concepts have been developed, the most typical one will probably be Tokamak type [4]. For its advance and development, international cooperation was established to organize the international thermo-nuclear reactor (ITER) taken by China, the European Union, India, Japan, Korea, Russia and the United States.

ITER project was focused on plasma science and technology and the mission did not include a complete set up of blankets for energy generation. A part of blankets will be assembled as a test blanket module (TBM). In BA program, welding and joining technologies were acknowledged as a prime technology of fabrication of TBM. In fusion reactors, two components are particularly important; the tritium-breeding blankets (TBB) and divertor. The TBB takes a role in extraction the

7

fusion energy. And it has to produce tritium for a self-sufficient operation. The divertor purifies the plasma by locally creating a magnetic configuration to evacuate the α-particles and impurities and also extracts fusion energy.

1.3.2 Fission reactors

The principal components of a nuclear reactor are the nuclear fuel, the moderator, the control rods and the coolant. There are many possible nuclear reactor sizes and configurations, with different fuel compositions, moderators, coolants and control mechanisms, all capable of allowing a nuclear chain reaction to be sustained and controlled. Many of these configurations have been investigated and studied in research programs or as prototype commercial plants, though only a few have been developed to the point of industrial maturity. The most successful reactor type is the Light Water Reactor (LWR), which uses ordinary water under high pressure as both the coolant and the moderator. LWRs come in two design configurations - the Pressurized Water Reactor (PWR) and the Boiling Water Reactor (BWR).

1.3.2.1 Pressurized Water Reactor (PWR)

Ordinary water is used as both coolant and moderator. The coolant is kept as high pressure (about 15.5 MPa) to keep it as a liquid. It is contained within the pressure boundary formed by the reactor pressure vessel and piping in the primary coolant system, and is circulated through the core using powerful pumps. Heat is transferred within steam generators to a separate, secondary coolant circuit, where water is boiled to create steam. This steam drives the electricity producing turbine generators (Fig. 1.4).

1.3.2.2 Boling Water Reactor (BWR)

Ordinary water acts as both coolant and moderator, as in PWRs. The coolant is kept as a lower pressure that in a PWR (about 7 MPa) allowing it to boil as it absorbs heat from the reactor. The resultant steam is passed directly to the turbine generators to produce electricity as show in Fig. 1.4. While the absence of steam generators simplifies the design, the absence of a secondary circuit can result in some radioactive contamination of the turbine.
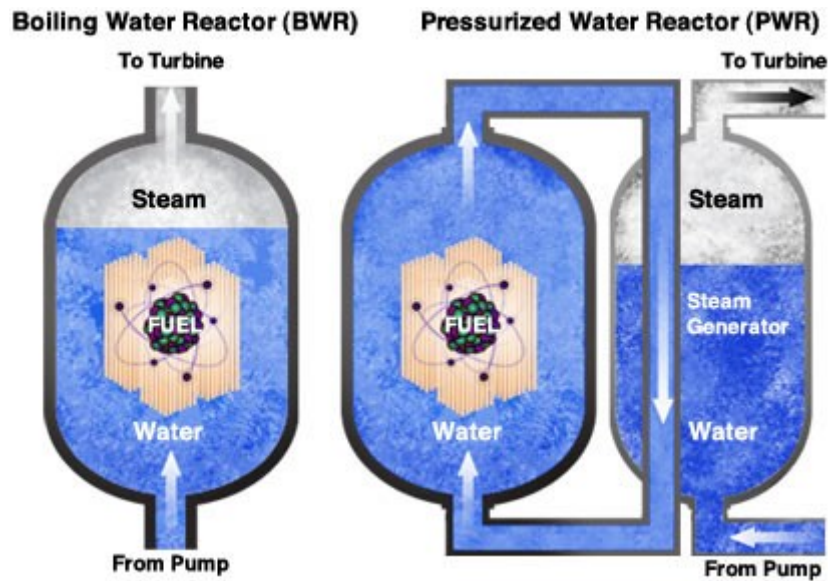
Fig. 1.4. The schematic diagram of the Pressurized Water Reactor (PWR) and Boiling Water Reactor (BWR)

1.3.2.3 Generation IV reactors

Technical design of nuclear power stations can be roughly divided on the generations of nuclear power stations, as shown in Fig. 1.5. First generation was developed in last century, more precisely in 50's and 60's and this type of power stations is no longer in use, because these were early prototypes. Most operating commercial nuclear reactors world-wide are of Generation-II category. The Generation-III reactors have just started to be deployed, and Gen-III+ reactors are at the advanced stage of commercialization. While the current second and third generation nuclear power plant designs provide an economically, technically, and publicly acceptable electricity supply in many markets, further advances in nuclear energy system design can broaden the opportunities for the use of nuclear energy. Therefore, the Generation IV International Forum (GIF) has selected six concepts to develop in order to meet the technology goals for new nuclear systems; Gas Cooled Fast Reactor (GFR), Lead Cooled Fast Reactor (LFR), Molten Salt Reactor (MSR), Sodium Cooled Fast Reactor (SFR), Supercritical Water Reactor (SCWR), Very High Temperature Reactor (VHTR).
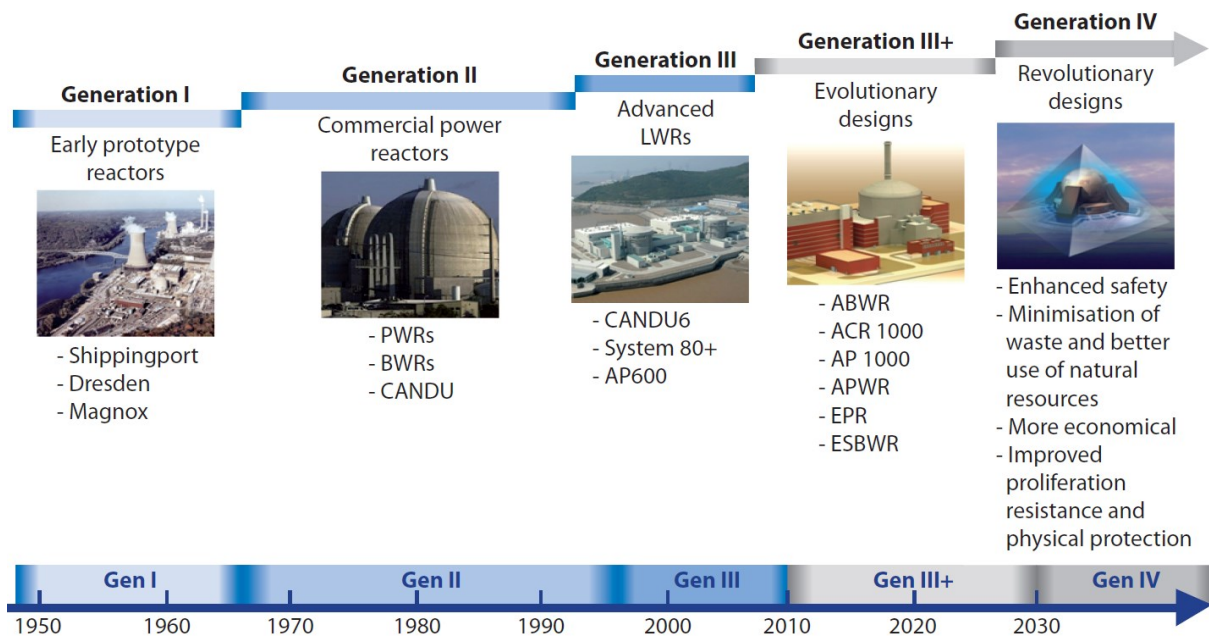
Fig. 1.5. Generation of nuclear power system.

1.4 Structural materials for nuclear reactor system.

The foremost consideration in the successful development and deployment of advanced reactor systems is the safety, performance and reliability issues involving structural materials for both in-core and out-of-core applications. The structural materials need to endure much higher temperatures, higher neutron doses and extremely corrosive environment, which are beyond the experience of the current nuclear power plants.

The main requirements for the materials to be used in advanced reactor systems are the following [6,7]: 1) The in-core materials need to exhibit excellent dimensional stability under irradiation, whether under stress (irradiation creep or relaxation) or without stress (swelling, growth). 2) The mechanical properties of all structural materials (tensile strength, ductility, creep resistance, fracture toughness, stiffness) have to remain acceptable after ageing, and 3) High degree of chemical compatibility between the structural materials and the coolant as well as with the fuel. In this regard, stress corrosion cracking (SCC) and irradiation assisted stress corrosion cracking (IASCC) are issues of important. These requirements have to be met under normal operating conditions, as well as in incidental and accidental conditions.

The main candidate plasma facing materials for fusion power reactors are reported in table 1.1.

And, Table 1.2 summarizes the different classes of materials considered for each system of generation IV. As shown in Table 1.1 and 1.2, many of concepts for fusion and fission reactors adopt the pressurized and/or high temperature water as a coolant media because of its many advantages. On the other hand, the currently operation nuclear plants have experienced capacity losses due to corrosion damage to a number of components, and the most serious issue is the SCC of Boiling Water Reactor (BWR) coolant piping and reactor internals and PWR steam generator tubes.

In both fusion and fission nuclear plants with water coolant systems, critical materials issues have included various forms of corrosion and stress corrosion cracking. These corrosion and SCC issues have had a significant impact on maintenance costs and safety operation of the plants.

Table.1.1 Main candidate materials for plasma facing and breeding blanket components [5]

Function	First wall	Breeding blanket	Divertor
Plasma facing material	W-base alloy, W-coated ODS steel, flowing liquid metal: Li	-	W-base alloy, W-coated SiC_f/SiC flowing liquid metal: Li, Ga, Sn, Sn-Li
Neutron multiplier material	-	Be, $Be_{12}Ti$, $Be_{12}V$, Pb	-
Tritium breeding material	-	Li, eutectic Pb-Li, Li-base ceramic material (Li_2O, Li_4SiO_4, Li_4SiO_4, + 2.5 wt.%SiO_2, Li_2TiO_3, Li_2ZrO_3, $LiAlO_2$)	-
Structural material	RAFM steel, ODS steel, Vanadium alloy, SiC_f/SiC	RAFM steel, ODS steel, Vanadium alloy, SiC_f/SiC	ODS steel, W-base alloy
Coolant	-	Water, helium, eutectic Pb-Li, Li	Water, helium

Table. 1.2 Summary of materials considered for the different systems.[6]

	SFR	GFR	LFR	VHTR	SCWR	MSR
Coolant	Liquid Na	He	Lead alloys	He	Water	Molten salt
P (MPa)	0.1	7	0.1	7	24	0.1
T (K)	625-825	755-1125	825-1075	875-1275	555-825	775-995
Core structures	Wrapper F/M steels	Fuel & core structures	Target, Window Cladding	Core Graphite	Cladding & core Structures	Core Structure
	Cladding Adv Aust & F/M steels			Control rods		Graphite
	F/M ODS	SiC$_f$/SiC composite	F/M steels ODS	C/C SiC$_f$/SiC	Ni based Alloys & F/M steels ODS	Hastelloy
T (K)	665-975	875-1475	625-775	875-1875	625-895	975-1075
Displacement dose (dpa)	Cladding 200	60 = 90	Cladding~00 dpa, ADS/target~100 dpa	7/25		

References

1. World Energy Outlook 2012 by IEA

2. BP Statistical Review of World Energy 2013, online at bp.com/statisticalreview.

3. Annual Energy Outlook 2013_EIA

4. P. Norajitra, L. Bühler, A. Buenaventura, E. Diegele, U. Fischer, E. Hutter, R. Kruessmann, S. Malang, J. Reimann, A. Orden, D. Ward, G. Vieider, F. Wasatjerna, Conceptual design of the dual-coolant blanket in the frame of the EU power plant conceptual study, 2002, FZKA Report 6780.

5. N. Baluc, K. Abe, J.L. Boutard, V.M. Chernov, E. Diegele, S. Jitsukawa, A. Kimura, R.L. Klueh, A. Kohyama, R.J. Kurtz, R. Lässer, H. Matsui, A. Möslang, T. Muroga, G.R. Odette, M.Q. Tran, B. van der Schaaf, Y. Wu, J. Yu, S.J. Zinkle, Status of R&D Activities on Materials for Fusion Power Reactors, Nucl. Fusion , Volumes 47 , 2007 , Pages 696–717

6. P. Yvon, F. Carré, Structural materials challenges for advanced reactor systems, Journal of Nuclear Materials., Volumes 385, 2009, Pages 217-222

7. K.L. Murty, I. Charit, Structural materials for Gen-IV nuclear reactors: Challenges and opportunities, Journal of Nuclear Materials 383 (2008) 189–195

Chapter 2

Literature Survey and Objectives

2.1 Overview of oxide dispersion strengthened steels

2.1.1 General

Oxide dispersion strengthened (ODS) alloys typically consist of a high temperature metal matrix - such as iron aluminide, iron chromium, iron-chromium-aluminium, nickel chromium or nickel aluminide - with small (5-50nm) oxide particles of alumina (Al_2O_3) or yttria (Y_2O_3) dispersed within it. In order to make the second phase be uniformly distributed in the matrix metal, ODS steels are usually made by powder metallurgy method. Dispersion strengthening is one of the strengthening methods to introduce high number density of obstacles to dislocation motion. When the obstacles like compounds are distributed in the fine grains, the matrix of the alloys can be significantly improved in the strength and hardness, which may be accompanied by a slight loss of plasticity and toughness. When the particles become smaller and higher in the size and number density, respectively, the performance of the ODS alloys becomes better.

2.1.2 History

In 1916, the tungsten filament dispersed with thorium oxide (ThO_2) was produced in Germany. In 1919, the filament started to be used in the USA. In 1946, sintered aluminum powders (SAP) were developed to increase heat resistance of Al alloys. In 1962, ODS-Ni alloy with ThO_2 (TD-Ni) was developed for application to turbine. After the development of mechanical alloying method by J.S. Benjamin, INCO, in 1970, the study on dispersion strengthened alloy processing made a great progress, and resultantly, dispersion strengthening coupled with solid solution hardening was achieved in so-called high temperature alloys.

2.1.3 Fundamental

The fundamental deformation properties of metals are determined by the behavior of dislocations, which are systematic line shape distortions introduced into the crystalline lattice. When the material is under stress, these dislocations can move to cause macroscopic strain. The dislocation motion can be impeded by irregularities of strain field in the crystal, such as in the form of grain boundaries, or in the form of impurities, which can act as 'pinning centers' or 'sinks' for the dislocations. The idea of deliberately introducing fine obstacles as the pinning species into the steel matrix was then taken up, and eventually led to the development of new steels with nano-scaled particles of transition metal

oxides (such as those of yttrium or chromium) dispersed in the matrix. Strengthening by the dispersion of ultrafine hard phases is the essence to improve the mechanical properties of materials under high temperature by hindering the dislocation motion at elevated temperatures. Generally, the following requirements have been imposed for dispersion strengthened particles: particles size should be as small as possible (less than 10 nm), particle spacing to achieve enough performance is in the range of several tens nm. In addition, the particles should be stable under high temperatures keeping the size be small by suppressing mutual agglomeration of the small particles. Phase stability of oxide particles is a critical for nuclear structural materials, because under irradiation, non-equilibrium condition is often generated to accelerate phase change. Thus, the ODS steels with fine and high number density of stable oxide particles have demonstrated high yield strength, high resistance to irradiation and thermal creep, as well as high corrosion resistance. This is one of the reasons why the ODS steels have been intensively researched in the world for the application to structural and cladding materials for next generation nuclear reactors.

2.1.4 Oxide dispersion strengthened steels for nuclear applications

An approach to elevate the limit service temperature of the ferritic steels, which has higher thermal conductivity and lower swelling than austenitic steels, is to disperse oxide particles in the ferritic steels. High strength at elevated temperatures of the ODS steels is due to the microstructures that contain a high density of small Y_2O_3 and/or TiO_2 particles dispersed in the ferrite matrix. ODS steels are being developed and investigated for nuclear fission and fusion applications in Japan [1,2], Europe [3,4], and the United States [5].

The chromium content in the previous ODS steels is in the range of 9 ~19 wt. %, while content of the other alloying elements (Al, W, Mo, Nb, Ti, Zr etc.) are at a level of a few percent or less. The main oxide particles of the ODS steels were Y_2O_3 with a size smaller than 10 nm of diameter mostly added with up to 0.5 wt.% at most. Along with yttrium oxides, also used were the alumina and titania [6]. At present there is a great variety of ODS steels with different grades and types, as grouped according to developer countries: Belgium: DT2906 (Fe-13Cr–1.5Mo–2.9Ti–0.6 O_2); DT2203Y05 (Fe–13Cr–1.5Mo–2.2Ti–0.3O–0.5 Y_2O_3) USA: MA957 (Fe–14Cr–0.9Ti–0.3Mo–0.25Y_2O_3); 12CrY1 (Fe–12.4Cr–0.25Y_2O_3); 12CrYWTi (Fe–12.3Cr–3W–0.39Ti–0.25 Y_2O_3) Europe: ODS EUROFER (Fe–9Cr–1.1W–0.2V–0.14Ta–0.3 (0.5) Y_2O_3) China: K7 (Fe – 13Cr – 1.1Ti – 0.2Mo – 2W – 0.39Y_2O_3) Japan: Fe–9Cr–0.12C–2W–0.20Ti–0.35Y_2O_3, Fe–12Cr–0.3C–2W–0.3Ti–0.23Y_2O_3

9Cr-ODS steels developed for sodium-cooled fast reactor shells turned out to be unpromising for supercritical water cooled reactors (SCWR) and liquid bithmuth eutectic fast reactors (LBEFR) due to high corrosion levels. For this reason, high Cr (up to 22 %) ODS steels with Al additives (up to 4.5 %) have been considered for the application to structural materials used in such a high corrosive environment [7].

The application of 9Cr-ODS steel to the cladding of SCWR and LFR is limited because of insufficient corrosion resistance of the steel [8,9]. Corrosion test results in supercritical pressurized water (SCW) and lead-bismuth eutectics (LBE) were referred to determine Cr and Al content. LBE has high solubility of nickel, iron and chromium, which are most important alloy elements in austenitic stainless steels, which is the reason of the difficulty to use nickel super alloys and iron-based austenitic stainless steels as the structural materials for LBE cooled systems, especially at temperatures higher than 773 K [10-14]. Ferritic steels that contain only a small amount of nickel have been considered to be more adequate for LBE application. Above 873 K, however, the solubility of iron and chromium in LBE also becomes significantly larger. In order to prevent material from dissolving into LBE, alumina coating was often conceived. Without alumina coating, however, it is also considered that alumina film, which is spontaneously formed on the surface of the steel containing Al in solution, may suppress dissolution. Fig. 2.1 shows the appearance of ODS steel specimens after corrosion test in LBE with 10^{-6} wt.%O_2 in solution for 10k hr at 923 K. The Al free 19 wt%Cr-ODS steel dissolved into LBE markedly, while those of ODS specimens containing 4 wt.%Al almost completely kept the specimen shape, indicating much higher resistance to LBE corrosion. It is worth to noting that the corrosion resistance in LBE is independent of Cr concentration from 13 to 19 wt.% in Al added ODS steels. The addition of Al is considered to be inevitable for structural materials to apply to LBE nuclear systems especially above 773 K.
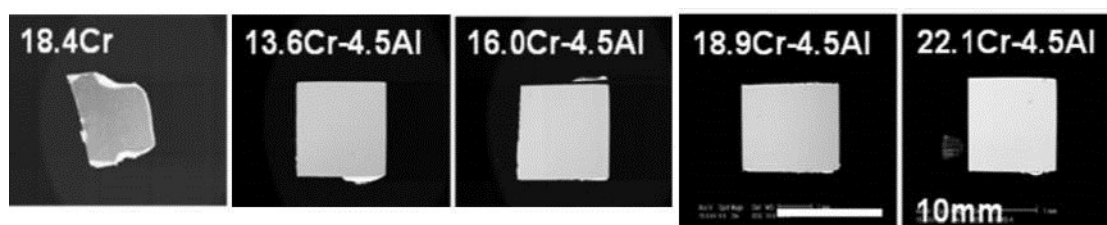
Fig. 2.1. The appearance of ODS steel specimens after corrosion test in LBE solved with 10^{-6} wt.%O_2 for 1×10^4 h at 923 K.

As for the corrosion resistance in SCPW, the previous surveillance test results showed that nickel super alloys were preferable [15]. However, nickel alloys are rather susceptible to irradiation embrittlement as well as helium embrittlement [16]. Fig. 2.2 shows the weight gain after corrosion tests in SCPW (773 K, 25MPa) up to 1800 hr. The weight gain of 9Cr-ODS steel is much larger than 16Cr-ODS steel, indicating that 9Cr-ODS steel is not adequate for application to SCWR. An EPMA and XRD analysis revealed that a thick Fe_3O_4 film was formed on the surface of 9Cr-ODS steel but not detected in the high-Cr ODS steels. It should be noted that the weight gain is much larger in SUS430 (16Cr) than in 16Cr-ODS steel. This clearly indicates that the oxide particles dispersion plays an effective role in the high corrosion resistance of ODS steels, since the corrosion resistance in water environment is mainly controlled by Cr concentration. The corrosion resistance of ODS steels increases with chromium concentration. The effect of Al on corrosion resistance depends on Cr concentration. In 19Cr-ODS steel, the addition of 4 wt.%Al did not remarkably influence the corrosion resistance [9]. However, in 16Cr-ODS steel, the addition of Al improved corrosion resistance. The suppression of corrosion by Al addition in 16Cr-ODS steel is due to formation of very thin alumina film on the surface. In 19Cr-ODS steel, rather dense chromia film was observed on the specimen surface [17]. It is considered that 16 wt.%Cr is not large enough to form homogeneous and stable chromia on the whole specimen surface, while very thin alumina film covers the whole specimen surface of the ODS steel added with 4 wt.%Al. Thus, an addition of Al is effective to improve corrosion resistance of 16Cr-ODS steel but not in 19Cr-ODS steel.
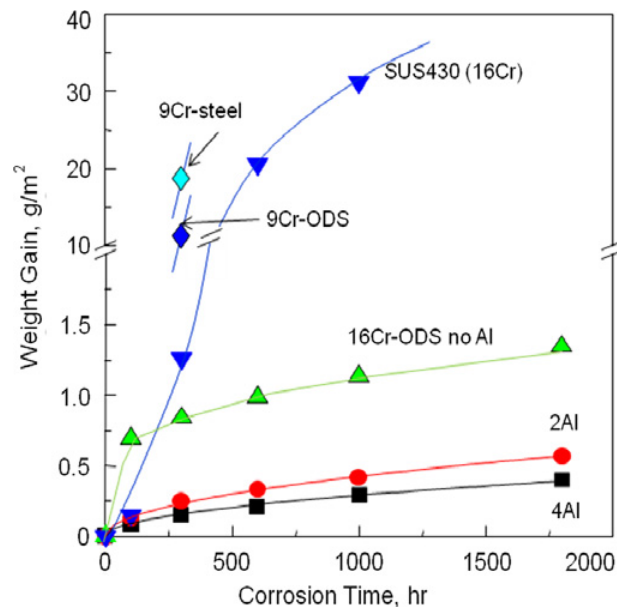
Fig. 2.2. Weight gain after corrosion tests in SCPW (783 K, 25 MPa) up to 1800 h.

Most serious problem of Al addition is a loss of strength. Fig. 2.3 shows the effects of Al addition on the tensile strength of the 19Cr-ODS steel, which clearly indicates that the Al addition significantly reduces the tensile strength, although the tensile strength of 16Cr-4Al-ODS steel is still much higher than a reduced activation ferritic steel, JLF-1.
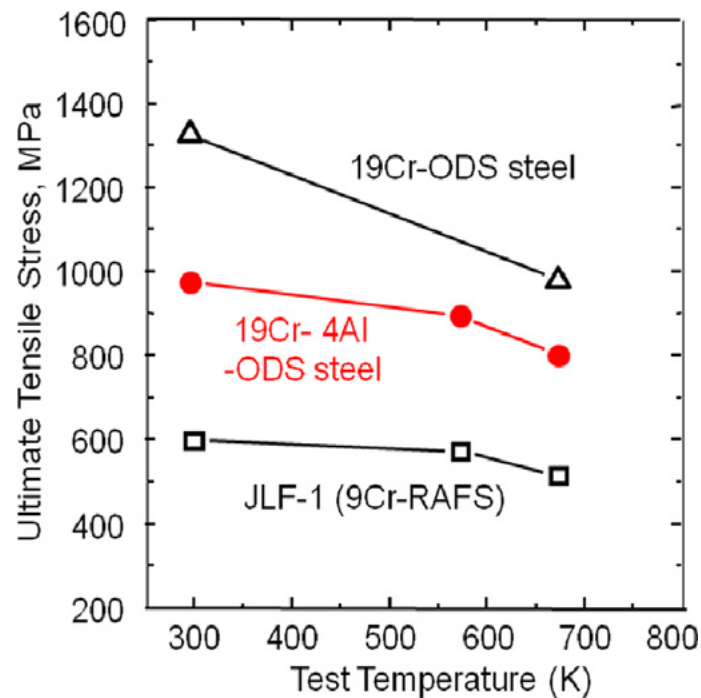
Fig. 2.3. The tensile strength of 19Cr-ODS steels with and without addition of Al as well as JLF-1 steel.

In order to investigate the mechanism of this reduction of strength by Al addition, TEM observations were performed, and it was revealed that the structure and dispersion morphology of the oxide particles were different between the steels with and without Al addition [18]. In the Al added steel, the average diameter of the oxide particles was about 7 nm but less than 3 nm in the Al free ODS steel. The number density of the oxide particles was reduced by almost one order of magnitude. The crystal structure of the oxide particle was also changed by the Al addition. As mentioned before, the fine oxide particles in the steel without Al addition were mainly pylochlore [19], while those in the steel with Al addition were mostly rather larger yttrium aluminum perovskites (YAP) and yttrium aluminum hexagonal (YAH) [20].

20

Yttrium-aluminum oxide particles are not adequate for strengthening of ODS ferritic steels, while yttrium-titanium pylochlore is effective for strengthening. Although alumina and yttria are well known as thermally stable oxides, the possible other sort of fine oxide particles are searched for their application to strengthening of the ODS steels with Al and Y. There are many stable oxide former elements, such as Y, Al, Ti, V, Ta, Nb, Hf, Zr, and so on. Table 2.1 shows the oxide formation energies of each alloy element at 1500 K. Among them yttria is familiar for ODS alloy production. The oxide formation energy is ranging widely from -520 for Nb to -995 kJ/mol O_2 for Y at 1500 K. Since the formation energy of yttria and alumina is -995 and -800 kJ/mol O_2, respectively, Hf and Zr may influence on the characteristics of oxide particles [21].

Table 2.1 The oxide formation energies of each alloy element at 1500 K [17].

Family	3A	4A	5A	3B	4B
Elements	Sc	Ti	V	Al	Si
Atomic#	21	22	23	13	14
Oxide	Sc_2O_3	TiO_2	V_2O_5	Al_2O_3	SiO_2
Formation energy	−990	−770	−570	−800	−
	Y	Zr	Nb		
Atomic#	39	40	41		
Oxide	Y_2O_3	ZrO_2	Nb_2O		
Formation energy	−995	−800	−500		
	La	Hf	Ta		
Atomic#	57	72	73		
Oxide	La_2O_3	HfO_2	Ta_2O_5		
Formation energy	−	−900	−570		

The effects of a small addition of Hf and Zr on the strengthening were investigated for 16Cr-4Al-Y_2O_3-ODS steel. Fig.2.4 shows the tensile strength at 973 K of each candidate ODS steel. 16Cr-4Al is a standard candidate ODS steel whose chemical compositions are 16Cr-4Al-2W-0.15Ti-0.35Y_2O_3. 16Cr is 16Cr-ODS steel without Al addition, showing much higher strength than 16Cr-4Al. The extrusion temperature was 1423 K except for the steels without notification in the figure. The addition of small amount of Hf and Zr is very effective to increase the strength at 973 K.
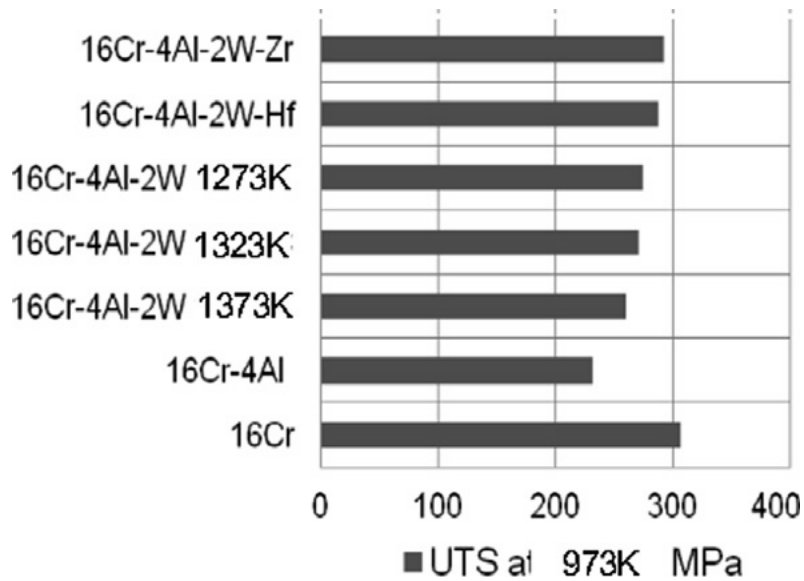
Fig. 2.4. Effects of extrusion temperature and addition of minor elements on the ultimate tensile stress (UTS) of 16Cr−4Al ODS steel at 973 K.

TEM observation revealed that the addition of Hf and Zr reduced and increased the size and the number density of oxide particles, respectively. Furthermore, the number density of grain boundary precipitates, such as carbides and oxides were increased remarkably by addition of Hf or Zr. Grain boundary precipitates are well known as obstacles for grain boundary sliding that is a typical deformation mode at elevated temperatures [22]. This effect also resulted in a significant increase in long term creep properties of the ODS alloy at 973 K, as summarized in Table 2.2.

Table 2.2 Creep test results at 973 K of each candidate ODS steel.

Materials	Creep strength (973 K, 10 k h) (MPa)
16Cr-ODS	100
16Cr–4Al-ODS	60
16Cr–4Al-ODS-Zr	120
16Cr–4Al-ODS-Hf	110

Thus, the positive effect of addition of Hf or Zr overcomes the negative effect of Al addition on high temperature strength. The Zr addition is more recommended than Hf addition in terms of neutron cross section area or neutron absorption.

In the process of additional alloying with zirconium or hafnium, dispersion of oxide yttrium particles shifts towards smaller sizes. High density of particles enriched in Ti, Y and O is observed. The mean size and concentration of oxide particles in initial and annealed samples of 12YW and 12YWT ODS steels (alloyed with titanium) are also close to values of 2-3 nm at a high mean concentration.

2.2 Supercritical water and supercritical water cooled reactor

The use of supercritical water in power production has a history about as long as nuclear power: the first commercial ventures into fossil-fired supercritical power plants initiated in the 50s [23]. The idea of combining the supercritical water and nuclear reactor has surfaced periodically, and the supercritical water cooled reactor (SCWR) is one of the most promising Generation IV nuclear reactor designs.

2.2.1 Supercritical pressurized water.

The phase diagram of water is illustrated in Fig.2.5. As the pressure increases the boiling temperature rises also. At the pressure of 22.1 MPa the boundary between liquid and gas phase vanishes. This point at 22.1 MPa and 374 °C is called the *critical point* of water. At the critical point the specific heat of the water is the highest, consequently the absorbed heat is the maximum for a given amount of water.

The operating ranges of SCWR along with conventional LWRs are also plotted in Fig. 2.5. While BWRs and PWRs operate at a pressure range where transition from liquid to vapor is possible, the operating pressure of the SCWR is high enough that there is no distinct phase transition from liquid to vapor. Since boiling alters the properties of water dramatically and the phase transition essentially occurs in BWRs, special attentions are demanded for the safety issues against the dry out of BWR and nucleate boiling crisis of PWR. At supercritical conditions (above 22.1 MPa, 374 °C) the complicated phenomenon of boiling is physically excluded.
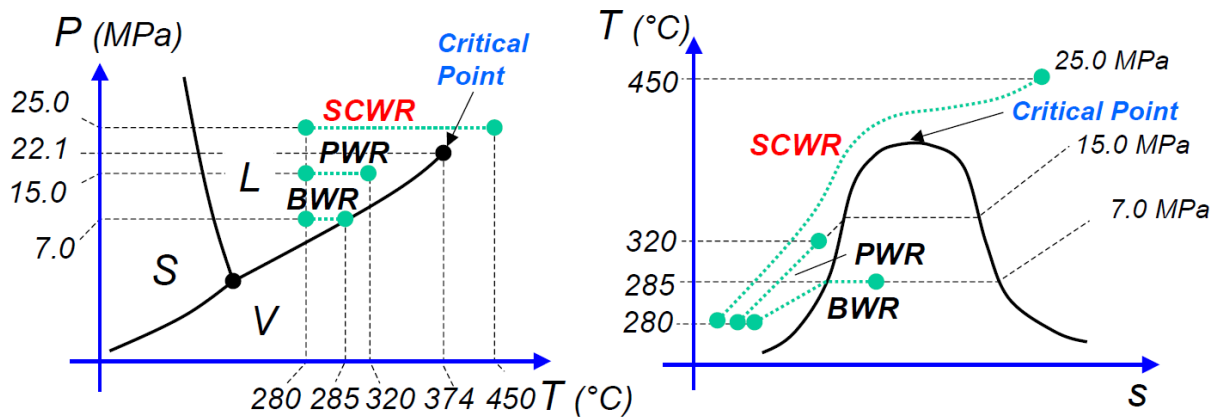
Fig. 2.5 : *Left*: Phase diagram of water,   *Right*: Temperature-Entropy diagram of water

The density of supercritical water has a strong function of temperature and pressure, as illustrated in Fig. 2.6. The difference in properties between supercritical water and normal water is most dramatic in the specific heat, as shown in Fig.2.7. Another relevant property difference is shown in Table 2.3, and it arises from the insolubility of inorganics in supercritical water, which raises the purity control requirements for the coolant.
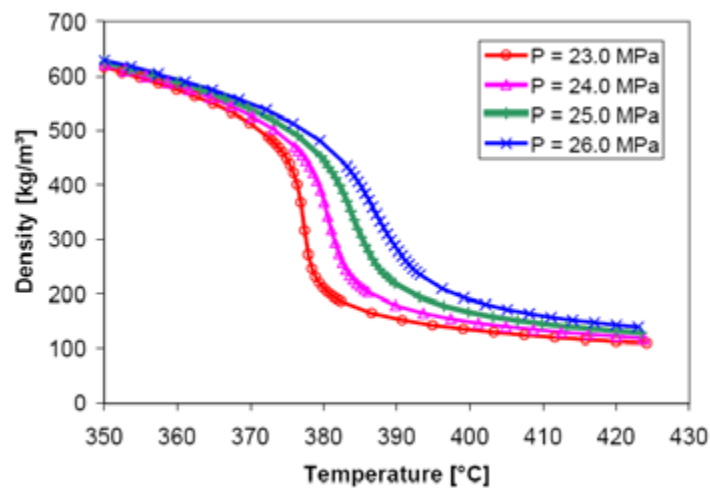
Fig. 2.6: Density changes in supercritical water as a function of pressure and temperature. From [24].
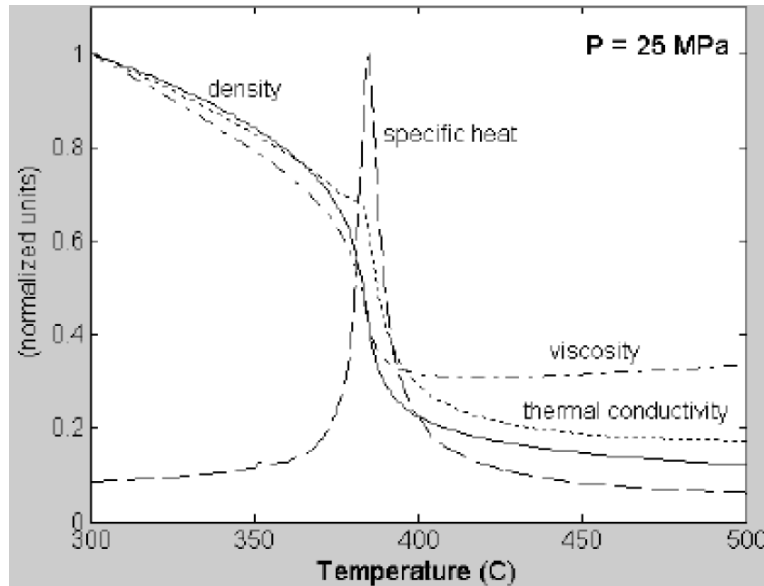
Fig. 2.7: Thermal variation of physical properties of water

Table 2.3. A comparison of some relevant properties of normal light water and supercritical light water.

	Normal Light Water	Supercritical Light Water
Dielectric Constant	78	< 5
Solubility of Organics	Very Low	Fully Miscible
Solubility of Gases	Very Low	Fully Miscible
Solubility of Inorganics	Very High	Not Soluble

2.2.2 Supercritical water cooled reactor.

SCWRs are basically LWRs operating at higher pressure and temperatures with a direct once-through cycle. One SCWR system is shown in Fig 2.8. These systems may have a thermal or fast-neutron spectrum, depending on the core design. SCWRs have unique features that may offer advantages compared to state-of-the- art LWRs in the following[25]:

• SCWRs offer increases in thermal efficiency relative to current-generation LWRs. The efficiency of a SCWR can approach 44%, compared to 33–35% for LWRs.

• A lower-coolant mass flow rate per unit core thermal power results from the higher enthalpy content of the coolant. This offers a reduction in the size of the reactor coolant pumps, piping, and

associated equipment, and a reduction in the pumping power.

• A lower-coolant mass inventory results from the once-through coolant path in the reactor vessel and the lower-coolant density. This opens the possibility of smaller containment buildings.

• No boiling crisis (i.e., departure from nucleate boiling or dry out) exists due to the lack of a second phase in the reactor, thereby avoiding discontinuous heat transfer regimes within the core during normal operation.

• Steam dryers, steam separators, recirculation pumps, and steam generators are eliminated. Therefore, the SCWR can be a simpler plant with fewer major components.
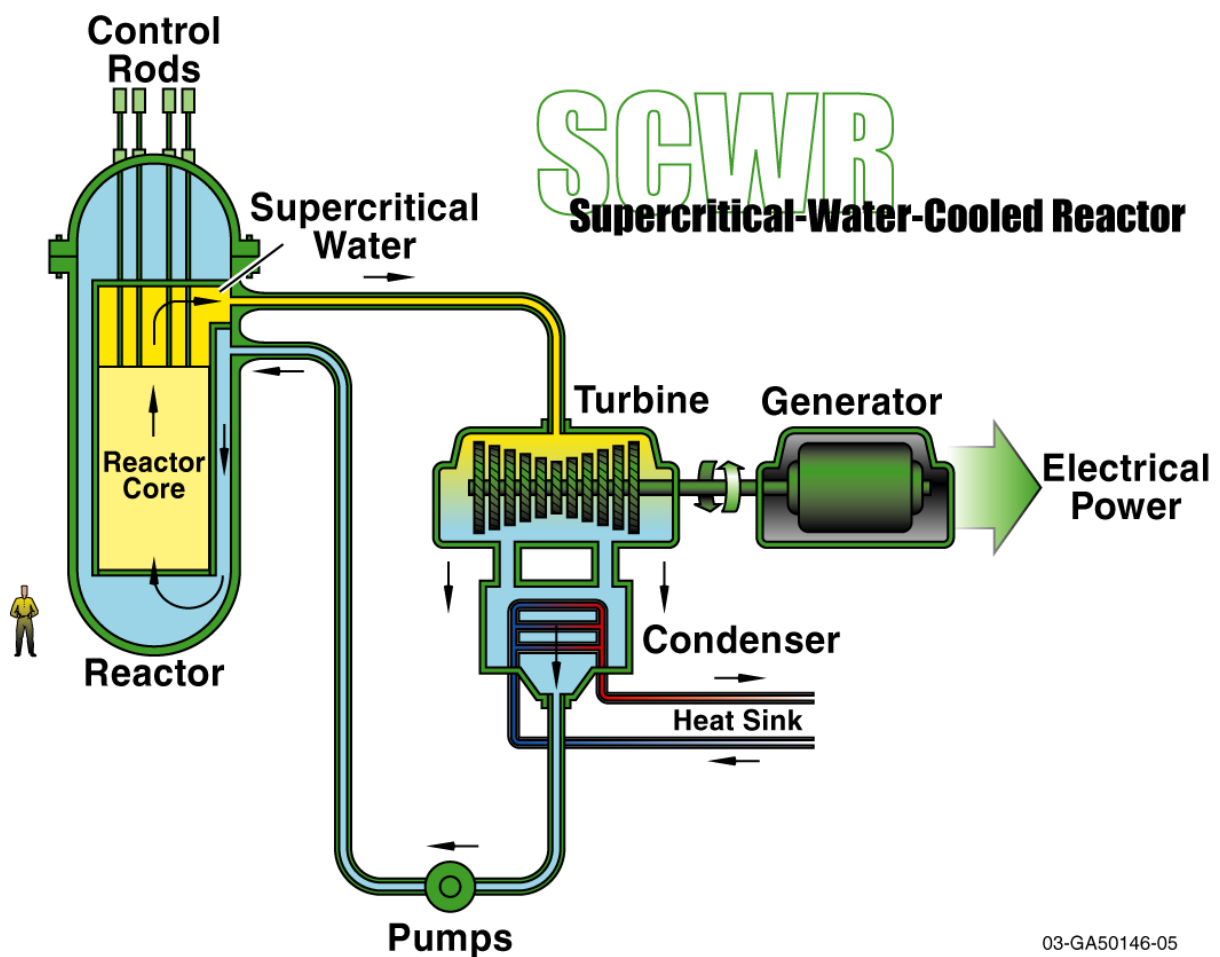
Fig. 2.8: The outline of a supercritical water cooled power plant. The power plant utilizes a direct steam cycle and, thanks to the properties of supercritical water, requires no steam driers or recirculation usually encountered in NPPs [26].

2.2.3 Materials issues for SCWR

As mentioned above, the supercritical water environment is unique and few data exist on the behavior of materials in SCW under irradiation and in the temperature and pressure ranges of interest. At present, no candidate alloy has been confirmed for use as either the cladding or structural material in thermal or fast spectrum SCWRs. Potential candidates include austenitic stainless steels, solid solution and precipitation-hardened alloys, ferritic/martensitic alloys, and oxide dispersion-strengthened alloys.

The fast SCWR design would result in greater doses to cladding and structural materials than in the thermal design by a factor of 5 or more. The maximum doses for the core internals are in the 10–30 dpa range in the thermal design, and could reach 100–150 dpa in the fast design. These doses will result in greater demands on the structural materials in terms of the need for irradiation stability and effects of irradiation on embrittlement, creep, corrosion, and SCC. The generation of helium by transmutation of nickel is also an important consideration in both the thermal and fast designs because it can lead to swelling and embrittlement at high temperatures. The data obtained during prior fast reactor development will play an important role in this area.

Although many of candidate materials have been selected based on satisfactory unirradiated properties and/or proven performance under irradiation, to meet these challenges, the R&D plan for the cladding and structural materials in the SCWRs focuses on acquiring data and a mechanistic understanding relating to the following key issues: corrosion and SCC, radiolysis and water chemistry, dimensional and micro structural stability, and strength and creep resistance.

2.2.3.1 Issues for SCWR corrosion and SCC research

The SCWR corrosion and SCC research can be focused on obtaining the following information: (1) Corrosion rates in SCW at temperatures between 280 and 620 °C (the corrosion should be measured under a wide range of oxygen and hydrogen contents to reflect the extremes in dissolved gasses), (2) Compositions and structure of the corrosion films as a function of temperature and dissolved gasses, (3) The effects of irradiation on corrosion as a function of dose, temperature, and water chemistry, (4) SCC as a function of temperature, dissolved gasses, and water chemistry, (5) The effects of irradiation on SCC as a function of dose, temperature, and water chemistry.

2.2.3.2 Water chemistry

As for the SCWR water chemistry research issues, the followings are necessary: (1) The complete radiolysis mechanism in SCW as a function of temperature and fluid density, (2) The chemical potential of H_2, O_2, and various radicals in SCW over a range of temperatures (280–620 °C), (3) Recombination rates of various radicals, H_2, and O_2 in SCW over a range of temperatures (280–620 °C) (4) Effect of radiation type: neutrons, gammas, as well as flux on radiolysis yields, (5) Formation and reaction of other species by radiolysis processes, (6) Impurities introduced into the primary system.

2.2.3.3 Dimensional and microstructure under irradiation

The issues of irradiation effect on dimensional and microstructures are the followings: (1) Void nucleation and growth, and the effect of He production, on void stability and growth, and He bubble nucleation and growth as a function of dose and temperature, (2) Development of the dislocation and precipitate microstructure and radiation-induced segregation as a function of dose and temperature, (3) Irradiation growth or irradiation induced distortion as a function of dose and temperature, (4) Irradiation-induced stress relaxation as a function of tension, stress, material, and dose.

2.2.3.4 Mechanical properties

Mechanical properties, such as strength, embrittlement and creep resistance, can be addressed on the followings: (1) Tensile properties as a function of dose and temperature, (2) Creep rates and creep rupture mechanisms as a function of stress, dose, and temperature, (3) Creep-fatigue as a function of loading frequency, dose, and temperature, (4) Time dependence of plasticity and high-temperature plasticity, (5) Fracture toughness as a function of irradiation temperature and dose, (6) Ductile-to-brittle transition temperature (DBTT) and helium embrittlement as a function of dose and irradiation temperature, (7) Changes in microstructure and mechanical properties following design basis accidents.

2.3 Basic damage mechanisms of stress corrosion cracking

Stress corrosion cracking is a complex phenomenon driven by the synergistic interaction of mechanical (stress), electrochemical (environment) and metallurgical (materials) factors. BWR, PWR and SCWR components can suffer from SCC, which may have transgranular (through the grains: TGSCC) or intergranular (along the grain boundaries: IGSCC) morphology.

Sometimes the modes are mixed or the mode switches from one to the other. IGSCC and TGSCC can occur in the same alloy, depending on the environment, the microstructure, or the stress/strain state. SCC usually propagates perpendicular to the principal tensile stress. Cracks can also vary in the degree of branching.

All SCC has a brittle-like appearance, since cracks propagate with little or no macroscopic plastic deformation. An alloy affected by SCC does not usually display abnormal mechanical properties although this may be observed in certain classes of alloys; such as precipitation hardened stainless steels or as a result of irradiation damage. Many alloys are susceptible to SCC in at least one environment. However, SCC does not occur in all environments, nor does an environment that induces SCC in one alloy necessarily induce SCC in another alloy.

SCC is usually divided into an initiation and a propagation phase. The initiation time can vary significantly and can be up to several decades. The propagation phase is often divided into two parts, a 'slow' propagation phase and a 'fast' propagation phase of which the latter is usually characterized by crack tip stress intensities, K_I, exceeding a characteristic apparent threshold value in pre-cracked fracture mechanics type specimens known as K_{Iscc}.

Perhaps the most critical factor concerning SCC is that three preconditions are necessary and must be present simultaneously. The elimination of any one of these factors or the reduction of one of these three factors below some threshold level can, in principle, prevent SCC. The three necessary preconditions are: 1) susceptibility (material); 2) tensile stress component (stress); 3) adequate aqueous environment (environment).

2.4 Review of stress corrosion cracking in hot water (BWR and PWR environments)

2.4.1 SCC in BWR

2.4.1.1 Material aspects

There have been two major material factors that have contributed to IGSCC of austenitic alloys in BWR primary coolant systems: thermal sensitization and cold work. Historically, it is well known that austenitic stainless steels and nickel based alloys were sensitized to the occurrence of IGSCC by heat treatment to cause formation of grain boundary carbide accompanied by Cr-depleted grain boundaries, which was named as sensitization treatment. Consequently, the steels were then replaced with low carbon grades or stabilized grades. In recently, however, even low carbon or stabilized steels, IGSCC has also subsequently occurred in cold worked steel.

Thermal sensitization may also occur in the heat affected zones (HAZ) of welds in austenitic alloys both during welding and also during stress relief heat treatments. Sensitization is again caused by the formation of chromium carbides (e.g. $M_{23}C_6$) on grain boundaries and a concomitant depletion of chromium on the grain boundaries and in the adjacent grains, as shown in Fig. 2.9. The reduction in chromium concentration adjacent to the grain boundaries, which may be as little as 2 % lower than the bulk concentration, gives rise to a reduction in passivity relative to the grains themselves and enhances IGSCC.
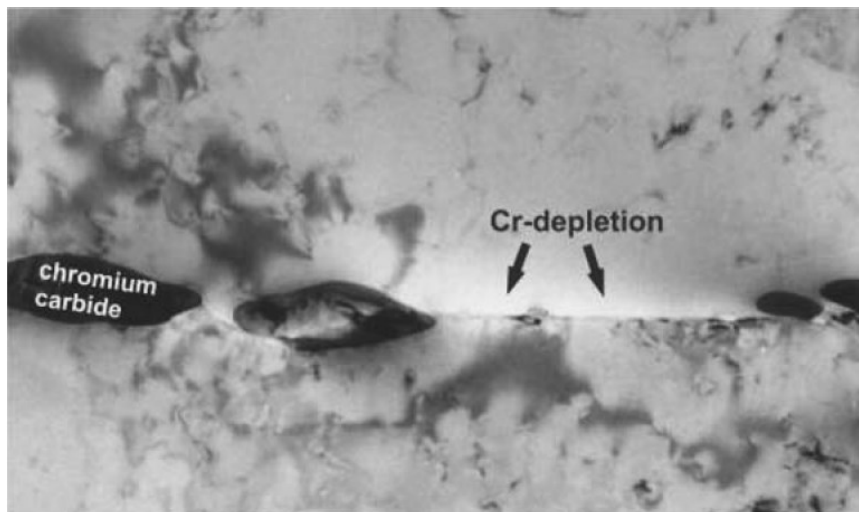

Fig 2.9 Transmission electron microscope (TEM) image showing Cr carbide precipitates along a grain boundary and the zone of Cr-depletion [27]

Thermal sensitization can be counteracted by using either low carbon grades (type 304L or 316L), or by stabilized stainless steels (type 347 and type 321), in which the majority of the carbon is bound by appropriate amounts of a strong carbide former such as niobium or titanium. A combination of both low carbon content, and high stabilization ratio (e.g. Nb/C >13) may enhance the benefits. Similarly, alloy 600 and 182 have been modified with niobium additions to prevent thermal sensitization.

Stainless steel castings and welds, which have a duplex phase of austenitic and ferritic structure, are not susceptible to thermal sensitization, because of the high diffusivity of chromium in the ferrite. Consequently, they are not susceptible to IGSCC in BWR systems.

In low carbon and stabilized grades of stainless steel, IGSCC occurred even at non-sensitized condition. It has been shown that the susceptibility to IGSCC is enhanced by cold work imposed during fabrication process. Hardness levels of the cold worked area have been above 300 HV. In many cases, the initial cracking was found to be transgranular and then changed to intergranular mode. The initial transgranular cracking is often associated with a surface layer of cold work induced by grinding or other severe surface machining techniques. Failures have also occurred where the occurrence of IGSCC was attributed to the presence of severe cold working (e.g. cold bent piping).

The mechanism by which cold work renders austenitic alloys susceptible to IGSCC is not fully understood and is still being investigated. It is possible that there is a synergistic interaction among deformation induced martensite, high residual stresses and localized deformation.

For application to heat resistant steel, alloy X-750 has been commonly used in one of two heat treatment conditions. The alloy X-750 is a precipitation hardened alloy with similar contents of nickel and chromium as alloy 600. One heat treatment is known as equalized and aged (EQA), in which the material subjects a two-step thermal treatment: the first at 885 °C for about 24 hours followed by ageing at 704 °C for 20 hours, which causes to be susceptible to IGSCC under BWR conditions. The second heat treatment, which is known as high temperature annealing (HTA), is a single step ageing at 704 °C for about 20 hours after solution annealing at 1093 °C for one to two hours. The main goal of HTA treatment is to precipitate the strengthening gamma prime phase, $NiAl_3$, together with a fine and high number density of $M_{23}C_6$ carbide distribution at grain boundaries. In BWRs the HTA is more effective to reduce the susceptibility to IGSCC.

2.4.1.2 Environmental aspects

IGSCC can occur in all grades and conditions of iron base stainless steel and nickel alloys if the requirements for environment and electrochemical corrosion potential (ECP) are conducive to SCC. However, from a practical point of view, the commonly agreed threshold for the possible occurrence of IGSCC in laboratory experimental results and field experience, is an ECP $\geq$ -230 mV$_{SHE}$ [28,29].

Under BWR normal water chemistry (NWC) conditions, the ECP is mainly influenced by the presence of oxidizing radiolysis products, O_2 and H_2O_2, dissolved in the high temperature water. These environmental conditions are potentially suitable for the occurrence of IGSCC among other contributing factors; notably metallurgical factors such as grain boundary sensitization or cold work, that is, high strain field. The main oxidant is hydrogen peroxide which exists in transiently in direct cycle BWR systems, but decomposes quite rapidly to water and oxygen on out of core surfaces away from the radiation field.

Other environmental conditions such as flow conditions, temperature and presence of impurities such as sulphate and chloride also influence the occurrence of IGSCC.

2.4.1.3 Tensile stress aspects

From a theoretical point of view, the role of tensile stresses is important for damaging or rupturing protective oxide films during both initiation and propagation of cracks. In the field, almost all SCC cases in BWR components occur in the vicinity of welds where the level of residual stresses produced by weld shrinkage is a very important factor having an impact on both crack initiation and crack propagation. For austenitic steels, SCC cracks propagate mainly through the heat affected zone (HAZ) of the base metal. For dissimilar welds, cracks are observed mainly in the weld metal alloy 182 (in some case propagating a short distance into the base material). Not only residual stresses but also cold work of the material can have pronounced effects on crack initiation and crack propagation.

The stress level at the surface triggers the process of crack initiation and these stresses may be either applied or residual. Flaws and other surface imperfection can act as stress raisers increasing local stresses at the (near) surface. Thus, corrosion attack (pitting or intergranular corrosion) or fabrication/welding defects/imperfections can act as a starting point for SCC. Very high surface stresses may also result from cold work introduced by fabrication processes such as machining, grinding or other surface finishing operations. Cold work can allow local near surface residual stresses

to remarkably exceed the original yield strength of the bulk material.

In contrast to crack initiation, the stress dependence of crack growth can be more easily quantified. Crack growth is driven by the sum of stresses due to operational and residual manufacturing stresses and SCC growth rates can be correlated with the local stress intensity factors K_I. Compared to the base metal, the calculation of the stress-state in welds is more complex and residual stress measurements are much more difficult because of anisotropy of the weld metal microstructure. For mitigation of SCC by stress improvement, different processes have been developed to reduce surface stresses or introduce compressive stresses at the surfaces exposed to BWR coolant; e.g. improved welding techniques, post weld heat treatment and peening

2.4.2 SCC in PWR

2.4.2.1 Material aspects

In contrast to a number of IGSCC occurrences of stainless steels in BWR, the same materials used in PWR have shown rather good performance, and the PWR-IGSCC has been mainly attributed to a combination of an inadvertent presence of oxygen trapped in stagnant regions and thermal sensitization and/or cold work [30]. However, nickel based alloys, particularly alloys 600, 132 and 182, have proved to be susceptible to IGSCC in the normal specification of PWR primary water systems, which is commonly known as PWSCC. The high strength analogue of alloy 600, alloy X-750, and to a considerably lesser extent alloy 718 with a somewhat higher chromium content, have also proved to be susceptible to PWSCC of which the details are discussed below. PWSCC susceptibility in alloy 600 has been shown to depend on the metallurgical structure, particularly the carbide morphology, and cold work level.

Nickel alloys, especially alloy 600, with many carbides on the grain boundary are found to be more resistant to PWSCC, whereas those with many intragranular carbides are the most susceptible. Since the carbon solubility in nickel alloys is low, carbon in solid solution combines with chromium to form chromium carbides during cooling from hot working temperatures.

The initial studies of the importance of the effect of carbide morphology on PWSCC susceptibility were carried out in connection with steam generator tube cracking. During the mill annealing process to produce steam generator tubes, the ability to get a favorable microstructure depends on the amount of carbon in solid solution to precipitate as carbides in the grains. Another cause of failure of

subsequent thermal treatment to give the favorable intergranular carbide morphology is tube straightening after mill annealing which generates dislocations on which carbides may precipitate preferentially. These microstructural considerations are not confined to tubing but also apply to thicker section forgings of alloy 600.

Microstructures that are most resistant to PWSCC have grain boundaries with a semi-continuous decoration of carbides (see Fig 2.10). Thermally treated alloys (705 °C for 16 hours) usually have improved PWSCC resistance for this reason. The mechanism by which PWSCC resistance is improved by grain boundary carbides remains open to debate. One hypothesis for the beneficial effect of intergranular carbides on PWSCC resistance has been proposed by Bruemmer who suggested that IG cracks are blunted by grain boundary carbides. In this mechanism dislocations are preferentially emitted from carbides at the crack tip, thereby reducing the stress concentration around them [31]. Another possible explanation arises from considerations of selective oxidation of chromium at the grain boundaries. In this case, carbides act a sink for oxygen and also present a more difficult diffusion path for oxygen. The role of carbon is not so clear in the case of alloy 182 and 82 weld materials, because it is preferentially precipitated as niobium carbide.
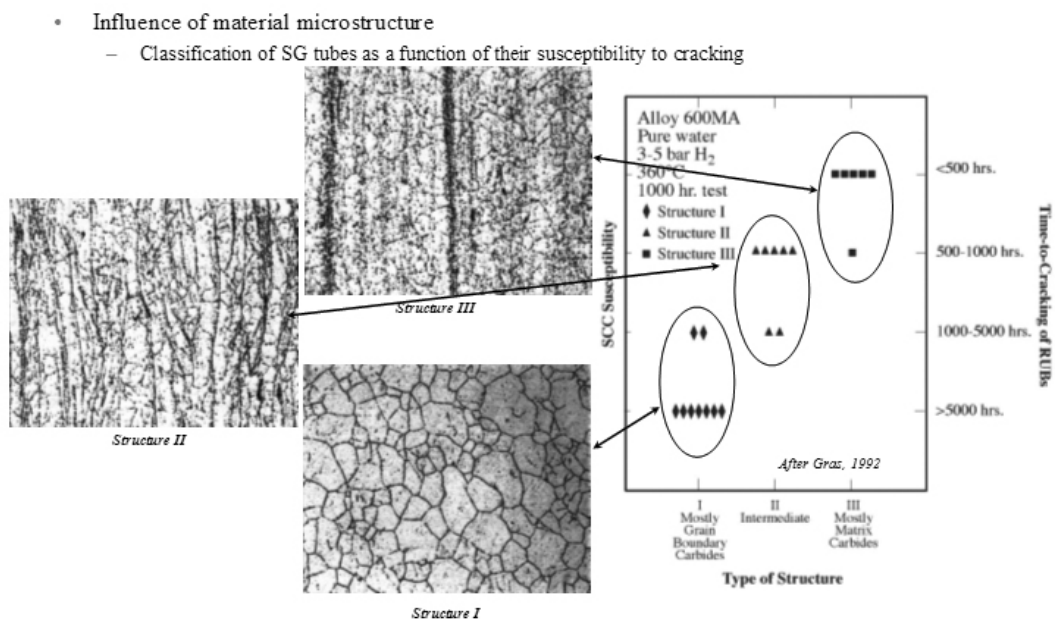

Fig 2.10 Carbide classification system due to Vaillant.

The use of alloy 600 for new and replacement components has been discontinued and has been replaced by alloy 690. The corresponding weld metals are alloy 52 and alloy 152. These alloys are characterized by significantly higher chromium content, approximately 30 %. No cracking has been reported to date in these materials after up to 20 year service. Nevertheless, laboratory work has shown that PWSCC propagation can occur after at least 10 % of unidirectional cold work in the plane of cold work or on steam generator tubes with a degraded microstructure. Many studies have confirmed the very high PWSCC initiation resistance of alloys 690, 152 and 52 at temperatures of up to 360 °C.

Alloy X-750 is also used in PWRs for high strength applications. The second of the two HTAs described in Section 2.4.1.1 produces a microstructure that is also more resistant to PWSCC, presumably due to the carbide morphology. Alloy 718, another precipitation hardened high strength alloy used in PWRs for high strength bolts and springs, is highly resistant to PWSCC initiation, but more susceptible to propagation. A few cases of PWSCC have occurred where oxidation damage of grain boundaries occurred during fabrication, which circumvented the crack initiation phase. Alloy 286 is a gamma prime strengthened stainless steel used in some high strength fastener applications where considerations of thermal expansion coefficients between austenitic components are important. The alloy is, however, rather susceptible to PWSCC, particularly in the condition of higher strength tempering, which demands that the applied stress must be very strictly controlled so as not to exceed the proportional limit even with stress concentrations in a practical uses.

2.4.2.2 Environmental aspects

The main environmental parameters in PWR primary systems influencing the SCC are temperature and the hydrogen concentration in the water, and to a much lesser extent the Li-content, interior related pH-value, and the presence of zinc.

The effect of hydrogen on the crack growth rate in alloy 600 and its weld metals has been extensively studied during the last few years, which indicated that the crack growth has a weak maximum in alloy 600, larger in the case of the weld metal alloys 182 and 132, at a hydrogen concentration approximately corresponding to the Ni/NiO equilibrium potential, as illustrated in Fig. 2.11.
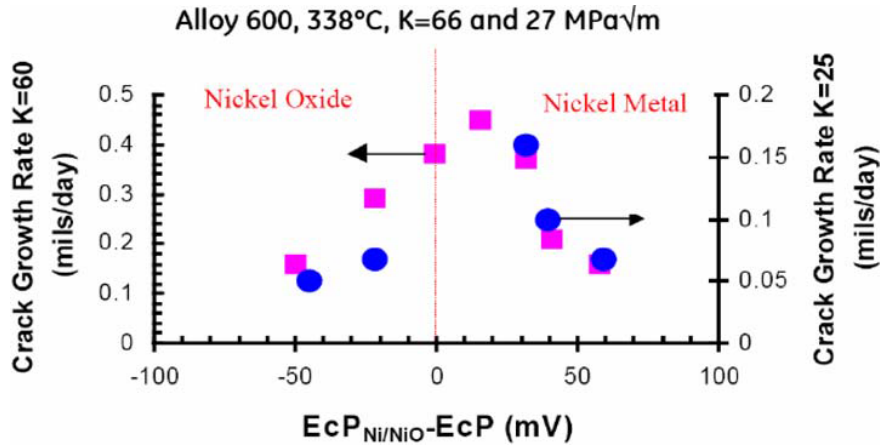
Fig. 2.11. Crack growth rate for alloy 600 in simulated PWR environment at 338 °C [32].

In addition, the temperature has a considerable effect on the PWSCC crack growth rate as illustrated in Fig. 2.12 for alloy 182 for three different hydrogen concentrations. The temperature varies in the primary system with the lowest temperature in the cold leg pipework and the highest in the pressurizer. The figure shows that the crack growth rate increases significantly with temperature; it also shows that the effect of hydrogen is considerable and that at high hydrogen concentrations corresponding to potentials less than the NiNiO equilibrium potential the crack growth rate decreases (as in Fig. 2.11).
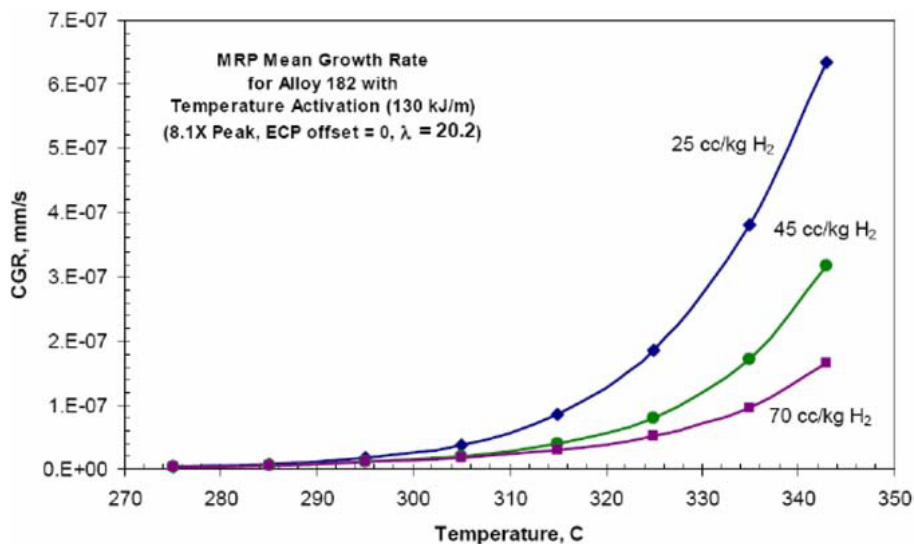
Fig. 2.12. Effect of temperature on PWSCC crack growth rate for alloy 182 [32].

Studies of the effect of hydrogen on the initiation of PWSCC do not show a peak in susceptibility as a function of hydrogen concentration but resistance to cracking continuously increases with decreasing hydrogen content (see Fig. 2.13). However, in the normal range of hydrogen applied in operating PWRs (25–50 cc/kg), the influence of hydrogen on crack initiation is relatively small. Note that hydrogen partial pressures below 5 kPa (corresponding to 7–8 ml H_2/kg H_2O at 330 °C) would be required to obtain significant benefits from reduced hydrogen concentrations. This is outside the present hydrogen specification and such low hydrogen contents have not yet been used in any operating PWR.

In summary, it appears that there are certain differences between the explanations indicated by initiation and propagation data as regards the effect of hydrogen partial pressure. As illustrated in Fig. 2.14, the propagation data shows a weak maximum whereas certain initiation data a continuous decrease of the initiation time with increasing hydrogen. The apparently strong effect of corrosion potential close to Ni/NiO oxide stability has not been explained, although the other oxides have been identified in long term experiments which might influence the cracking tendency.
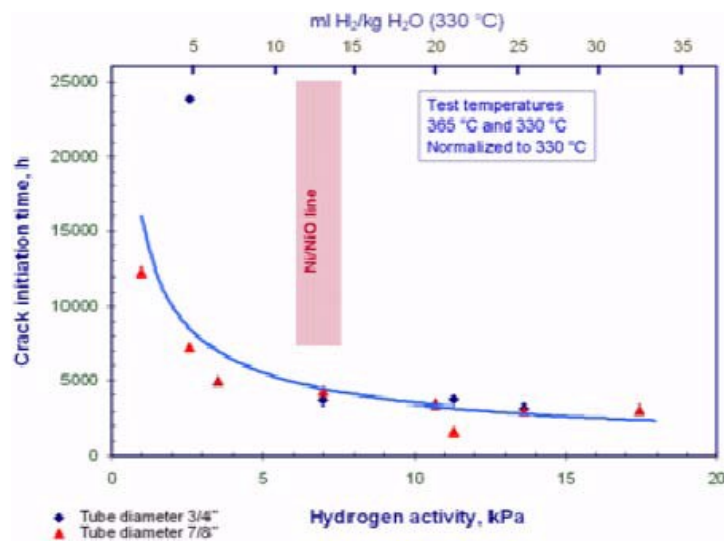
Fig. 2.13. The effect of hydrogen on initiation time. The data includes measurements at different temperatures normalized to the hydrogen partial pressure at 330 °C [33].
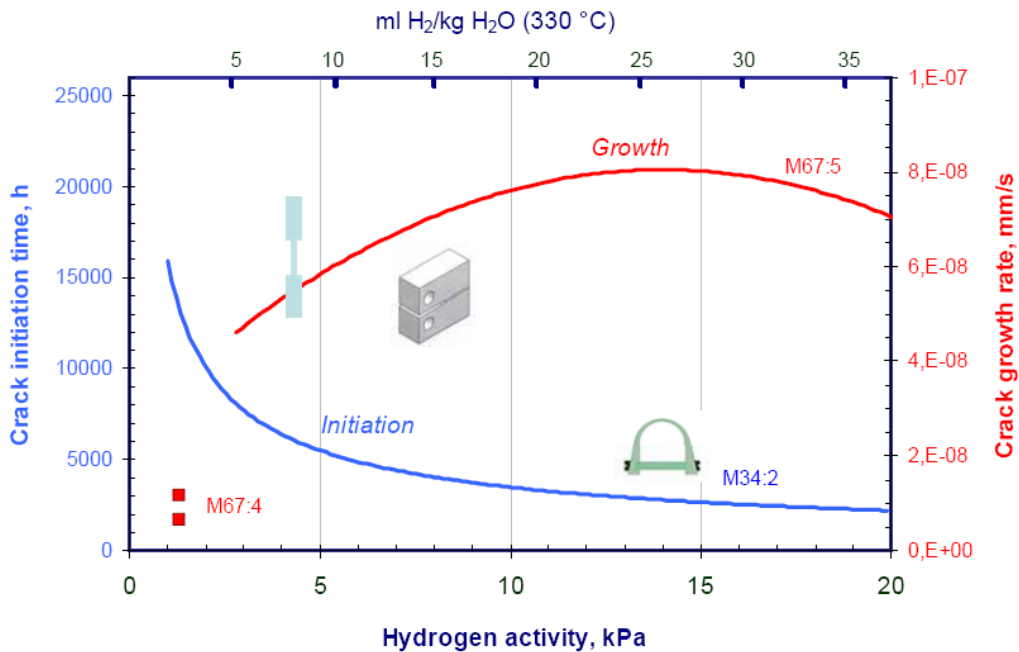
Fig. 2.14. Comparison of the effect of hydrogen on initiation and propagation of PWSCC in alloy 600 MA [7].

The effect of lithium on PWSCC has drawn some attention in recent years, as extended fuel cycles imply operation at higher Li contents (and pH) during the beginning of a fuel cycle. Earlier crack initiation data indicate that moderate increases in Li content decrease somewhat the initiation time. The effect of higher Li content (>7 ppm) on the initiation of PWSCC has not been investigated. Regarding the effect of Li on the crack growth rate, data generated so far show no or little influence. EDF has observed a small detrimental influence of Li 3.5 ppm/ 2 ppm on crack growth rates (CGRs) (×2.6) but no influence on initiation (for times greater than 18 000 h).

Zinc is being added to some PWR primary loops mainly to reduce the activity buildup. The zinc concentration used is around 5–10 ppb. However, zinc may also have a significant beneficial effect on the initiation of PWSCC. Zinc additions have also been applied in plants for such reasons. The additions are larger and up to 40 ppb. Regarding crack growth, the available data is inconclusive, while it indicates that there is little or no effect of Zn.

The effect of any future changes in PWR chemistry should be carefully considered with respect to PWSCC of alloy 600, alloy 182 and other structural materials due to the unresolved contradictions

between initiation and propagation data. Utilities are recommended to carefully study and follow ongoing research. It should also be pointed out that a change of hydrogen can also influence activity transport and buildup as well as AOA conditions. These questions have not yet been resolved.

2.4.2.3 Tensile stress aspects

Constant load PWSCC tests have been performed on alloy 600 base metal, alloy 690 base metal and alloy 132/182/82 weld metals. Some of these results are shown in Fig. 2.15–2.17. As a result, alloy 600 and alloy 132/82 have identifiable threshold stresses but for alloy 690 and the associated high Cr weld metals (152/52), no threshold stress has been measured in PWSCC tests since no cracking occurred [34].

In general, few instances of IGSCC in stainless steels have been observed in PWRs. There are, however, many SCC issues with alloy 600 and other Ni-based alloys. However, contrary to BWR experience, few PWR SCC issues are associated with weld HAZs. Most cracking has been observed in wrought materials remote from HAZs or in weld metals. The surface residual stress due to grinding or other surface finishing operations plays an important role in all cases of PWRSCC and strain reversals or deformation texture in the cold worked material are always involved.
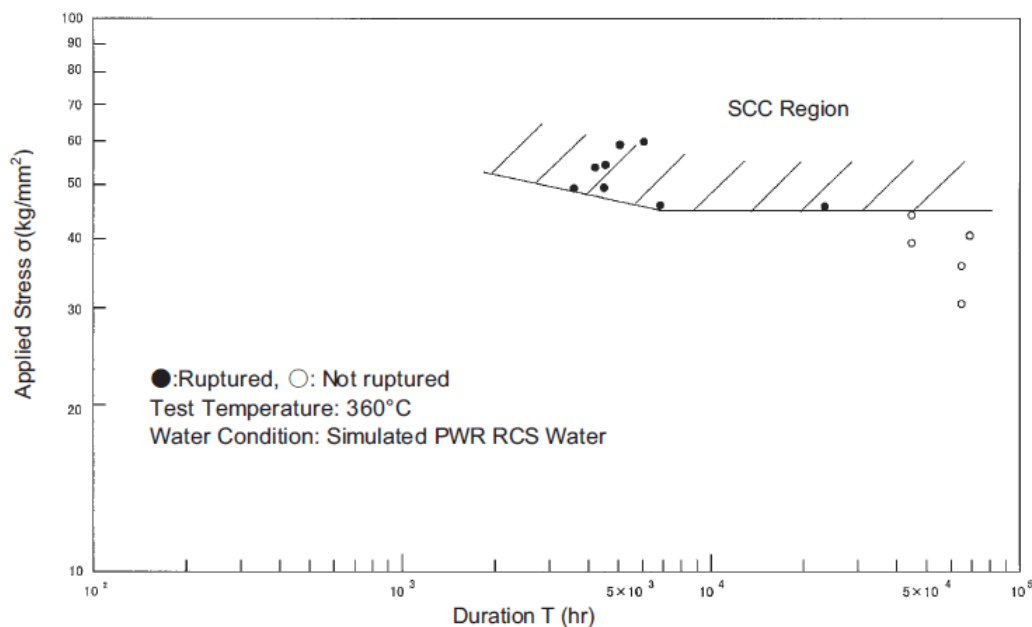
Fig. 2.15. Results of constant load PWSCC tests for alloy 600 base metal.
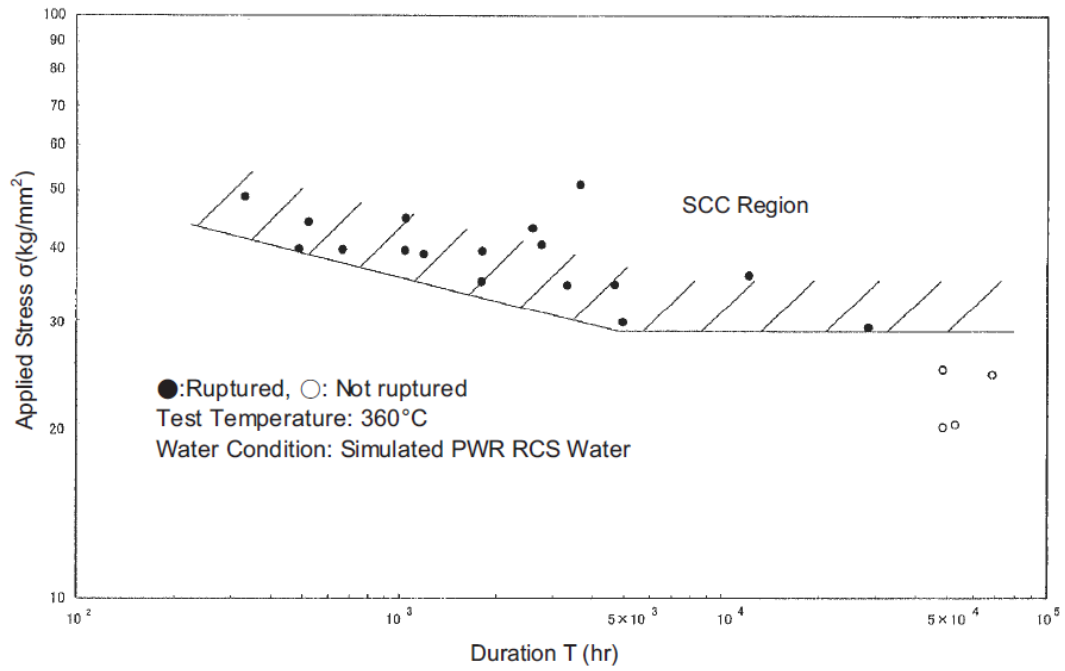
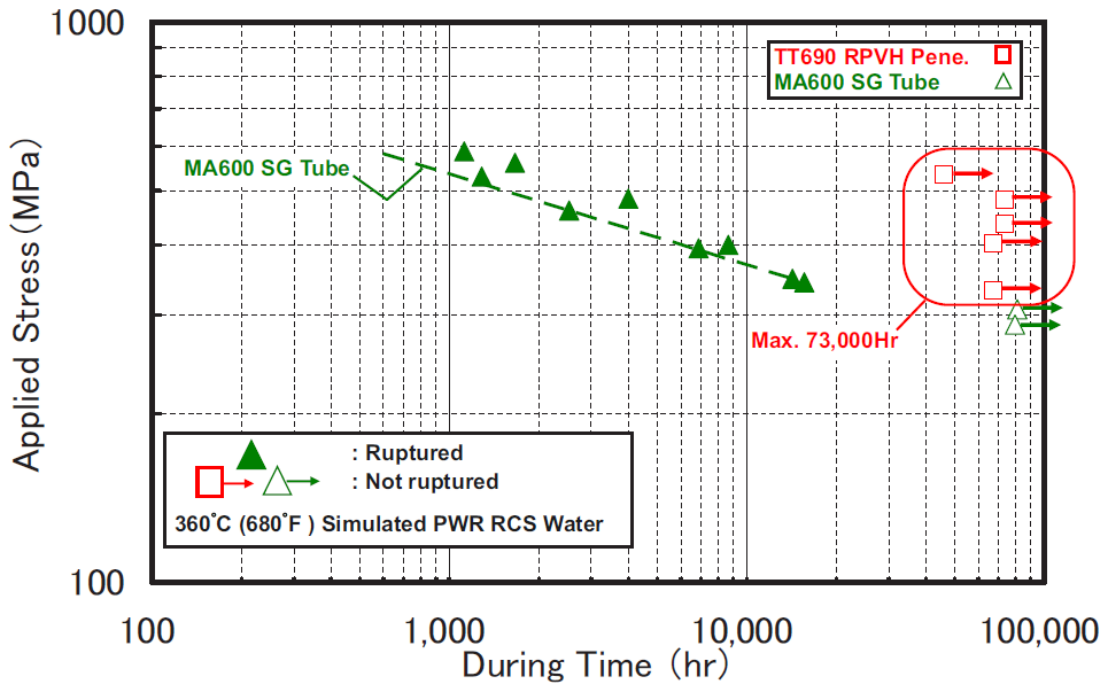Fig. 2.16. Results of constant load PWSCC tests for alloy 132/82 weld metal.

Fig. 2.17. Results of PWSCC tests on alloy 690 base metal and Alloy 600 base metal showing no cracking detected in alloy 690 after test times up to ~75 000 hours.

2.5 Review of stress corrosion cracking in supercritical pressurized water

An early study of SCC of 316 SS in degassed SCPW was reported by Boyd and Pray [35]. Their samples were exposed to 732 °C, 34.5 MPa SCPW and stressed to 90 % of the stress required to cause rupture in 1000 hours (103 MPa). It was found that the samples failed after one week of exposure. The SEM observations of fracture surface and the side surfaces revealed the presence of transgranular cracking. Fournier et al. [36] carried out constant extension rate tensile tests (CERT) at a strain rate of 1×10^{-6} s^{-1} to test alloys 690 and 718 in 400 °C, 25 MPa SCPW under aerated conditions. Alloy 718 failed by IGSCC such that the entire fracture surface was IG in nature and exhibited no necking. It was determined that the cracking was initiated by the oxidation of niobium precipitates in the alloy. Alloy 690 failed by completely ductile rupture and showed a significant amount of necking. Both of these alloys were also tested in air environments at 600 °C using the same type of CERT experiments. The tests in air revealed behavior for each alloy that was similar to that in SCPW at 400 °C.

Recent results by Teysseyre et al. [37] indicate that IGSCC is a significant problem throughout the SCWR temperature range for austenitic alloys. In a comprehensive study of SCC behavior between 400 and 550 °C for alloys 304L, 316L, 625 and 690, they found that in deaerated SCPW under constant extension rate, all alloys display some degree of IGSCC at all temperatures. Alloys 304L and 625 suffered the most severe cracking with crack depths exceeding 300 μm in the case of 304L at 550 °C. They were able to identify at least 3 distinct cracking modes; TG, IG and tarnish rupture and were able to determine the activation energies for cracking, which were about 100 kJ/mol for 304L and 625 and 80 kJ/mol for 316L and 690. Fig. 2.18 shows the strong effect of temperature on crack growth rate measured from CERT samples for 304L, 316L, 625 and 690. [37]

Tsuchiya et al. [38] investigated the behavior of sensitized 304 and 316 stainless steels using CERT experiments at 4×10^{-7} s^{-1}. The test temperature ranged from 290-550 °C, with a pressure of 25 MPa, and high purity water dissolved with oxygen content of 8 ppm. For both alloys, the fracture surface did not show any sign of IGSCC for temperatures above 400 °C. However, 304 did show IGSCC on the fracture surface at temperatures below 400 °C. Both alloys had small cracks on the side surface when exposed to SCPW. Watanabe et al. [39] examined the SCC behavior of sensitized 316 stainless steel as a function of pressure using CERT experiments at 2.78×10^{-6} s^{-1}. They found that the fracture surface of the alloy was almost completely IG in nature under subcritical conditions of 360 °C and 25 MPa. Fracture was transgranular under 400 °C, 30 MPa supercritical conditions. However, as the pressure was increased at 400 °C, the fracture mode became more predominantly IGSCC. They also found that small additions of H_2SO_4 induced in IG fracture.
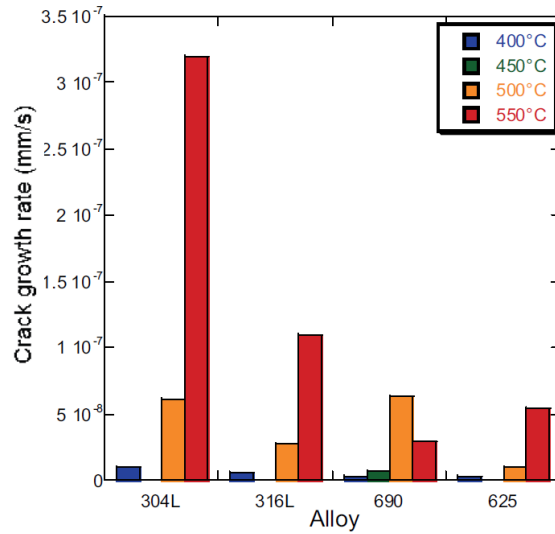
Fig. 2.18. Crack growth rate measured from cross sections of CERT samples for alloys 304L, 316L, 625 and 690 between 400 °C and 550 °C in deaerated SCW. [37]

Fujisawa et al. [40] studied SCC of 316, C-276, 625 and MC alloy in 400 °C SCPW containing 8 ppm dissolved oxygen. No IG cracks were observed in pure water, but the addition of small amounts (0.001 mol/l) HCl resulted in IG cracking in both 317 and alloy C-276.

Bosch [41] tested a superaustenitic stainless steel, N31266, a superduplex stainless steel, S32550, and two nickel base alloys N06625 and N06030 in 250-450 °C SCPW with additions of hydrogen peroxide in dynamic (CERT) and static (constant stress) loading mode. The CERT tests were conducted at a strain rate of 5×10^{-7} s^{-1} and the constant load tests were conducted with loading the elastic limit, $\sigma_{y\ 0.2}$. in SCPW+10% H$_2$O$_2$, the superaustenitic stainless steel exhibited cracking in CERT test at 400 °C but not in constant load tests. Higher concentrations of H$_2$O$_2$ or the addition of NaCl were required to cause cracking in this alloy. The superduplex stainless steel did not crack in constant load tests under any conditions. Cracking occurred in CERT tests using N06625 at 400 °C, while cracking in constant load tests required the addition of NaCl similar with the superaustenitic alloy. No cracking occurred in N06030 under constant load testing.

U-bend experiments conducted at VTT in 400 °C SCPW containing 1 bar H$_2$ overpressure did not result in cracking after 1000 hr and 675 hr for austenitic alloys (304, 304L, 321, A286) and nickel-base alloys (625, Uranus B66, 690, 718, 800), respectively. [42]

Cracking has not been observed in ferritic-martensitic alloys with the exception of HT-9, which

showed minor amounts of IG at 400 °C [43].

Very little data exists on Ti alloys in supercritical water, though there is a significant database in subcritical water. The only experiment conducted in SCPW was on Ti–15Mo–5Zr–3Al in pure SCPW at 550 °C, 25 MPa and 8 ppm dissolved oxygen. The maximum stress was 249 MPa, and the strain to failure was 38 %, resulting in a crack density of 26 cracks/mm^2 [44]. Similarly, several experiments have been conducted on ODS alloys in subcritical water [45,46], no experiments have been conducted to date in SCW.

2.6 Summary of introduction and objectives of this research

Energy is one of the most significant resources of global economy, and is necessary to increase the opportunities of economic and social development. Already today, the world's energy consumption - 80% of which is produced from fossil fuels, whose combustion generates carbon dioxide and other greenhouse gases – accounts for 12 billion tonnes of oil equivalent. The growth of the demand is estimated in 40 % over 20 years, due to the increased population and industrialization, especially in emerging countries. Even with improvements in energy efficiency, it is expected that global energy demand would be doubled by 2050. Therefore, we must face several challenges: meeting significant electricity needs while facing the reduction of fossil fuels and enacting measures to tackle climate change. In order to achieve these objectives, it is certainly necessary to save electricity, develop carbon capture and storage technologies and increase as much as possible the use of renewables. Nevertheless, no source, not even renewables, is capable alone of meeting electricity needs. The most suitable solution is therefore a balanced generation mix that includes fossil fuels, renewables and nuclear power. Indeed, nuclear ensures the stability of electricity generation while allowing the reduction of carbon dioxide emissions: over one year, a nuclear power station can save emissions for 9 million tons of carbon dioxide. It would be equivalent to removing 4 and a half million cars from the roads. These advantages have led the positive prediction of the increasing nuclear energy by many of international energy reports.

Nuclear materials R&D is essential to identify key priority topics and funding opportunities with the purpose of supporting in an efficient way the development and optimization of a sustainable nuclear energy. However, the operating conditions envisaged for nuclear systems are demanding and will impact on the performance of the structural and clad materials, the safety and the feasibility of most of nuclear reactor concepts and their optimization will depend crucially on the capability of the

chosen materials to withstand the expected operating conditions. Among the various nuclear material issues, stress corrosion cracking (SCC) is one of the significant ageing degradations for major components of pressurized water reactors (PWRs), boiling water reactors (BWRs) and supercritical water reactors (SCWRs) and is still an important technical issue.

However, the experiment data of SCC susceptibility of ODS steels in supercritical pressurized water (SCPW) has not been reported to our knowledge. And all of tests for SCC susceptibility in SCPW were conducted with oxygen environments but not in SCPW dissolved with hydrogen.

In this research, therefore, the stress corrosion cracking susceptibility was investigated for oxide dispersion strengthened (ODS) ferritic steel and conventional structural steels such as F82H ferritic/martensitic steel and SUS316L austenitic stainless steel in supercritical pressurized water (SCPW) dissolved with various oxygen and hydrogen contents. And, the specimen morphologic effects such as surface roughness and specimen size and shape were discussed for the structural metallic materials based on the results from slow strain rate test (SSRT) in vacuum and SCPW.

References

1. S. Ukai, T. Nishida, H. Okada, T. Okuda, M. Fujiwara, and K. Asabe, Development of Oxide Dispersion Strengthened Ferritic Steels for FBR Core Application, (I), J. Nucl. Sci. Tech. 34 (1997) 256-263.

2. S. Ukai, T. Yoshitake, S. Mizuta, Y. Matsudaira, S. Hagi, and T. Kobayashi, J. Nucl. Sci. Tech. 36 (1999) 710.

3. A. Alamo, J. Decours, M. Pigoury, C. Foucher, in: Structural Applications of Mechanical Alloying, ASM International, Materials Park, Ohio, 1990.

4. A. Alamo, H. Regle, G. Pons, and L. L. Bechade, Materials Science Forum 88-90 (1992) 183.

5. D. K. Mukhopadhyay, F. H. Froes, and D. S. Gelles, J. Nucl. Mater. 258-263 (1998) 1209-1215.

6. N.A. Azarenkov, V.N. Vojevodin, V.G. Kirichenko, G.P. Kovtun, V.V. Kurinny, S.V. Lytovchenko, NANOSTRUCTURAL MATERIALS IN THE NUCLEAR ENGINEERING, 2013, 58

7. A. Kimura, R. Kasada, N. Iwata, H. Kishimoto, C.H. Zhang, J. Isselin, P. Dou, J.H. Lee, N. Muthukumar, T. Okuda, M. Inoue, S. Ukai, S. Ohnuki, T. Fujisawa, T.F. Abe, Development of Al added high-Cr ODS steels for fuel cladding of next generation nuclear systems, J. Nucl. Mater. 417 (2011) 176-179

8. A. Kimura, S. Ukai, M. Fujiwara, in: Proc. Int. Conf. On Grobal Environ. Adv. Nucl. Power Plants, (GENES4/ ANP2003), CD-ROM file, 2003, p. 1198, ISBN: 4- 901332-01-5.

9. A. Kimura, S. Ukai, M. Fujiwara, in: Proc. Int. Cong. Adv. Nucl. Power Plants, (ICAPP-2004), CD-ROM file, 2004, p. 2070, ISBN: 0-89448-680-2.

10. H.U. Borgstedt, G. Drechsler, G. Frees, Z. Peric, J. Nucl. Mater. 155−157 (1988) 728−731.

11. M. Broc, T. Flament, P. Fauvet, J. Sannier, J. Nucl. Mater. 155−157 (1988) 710− 714.

12. V. Coen, H. Kolbe, L. Orecchia, J. Nucl. Mater. 155−157 (1988) 740−743.

13. T. Sample, H. Kolbe, J. Nucl. Mater. 283−287 (2000) 1336−1340.

14. G. Benamati, C. Fazio, I. Ricapito, J. Nucl. Mater. 307−311 (2002) 1391−1395.

15. M. Harada, O. Kubota, H. Anada, Kobe Steel Eng. Rep. 53 (3) (2003) 92−97.

16. M.R. James, S.A. Maloy, F.D. Gac, W.F. Sommer, J. Chen, H. Ullmaier, J. Nucl. Mater. 296 (2001) 139−144.

17. H.S. Cho, A. Kimura, S. Ukai, M. Fujiwara, J. Nucl. Mater. 329−333 (2004) 387− 391.

18. P. Dou, R. Kasada, A. Kimura, T. Okuda, M. Inoue, S. Ukai, S. Ohnuki, T. Fujisawa, F. Abe, J. Nucl. Mater. 417 (2011) 166−170.

19. S. Yamashita, S. Ohtsuka, N. Akasaka, S. Ukai, S. Ohnuki, Philos. Mag. Lett. 84 (8) (2004) 525.

20. P. Dou, A. Kimura, T. Okuda, M. Inoue, S. Ukai, S. Ohnuki, T. Fujisawa, F. Abe, Acta Mater., in press.

21. ″Metal Data Book″, Jpn Inst. Metals, 1984, pp. 84.

22. A. Kimura, R. Kasada, N. Iwata, J. Isselin, P. Dou, J.H. Lee, T. Okuda, M. Inoue, S. Ukai, S. Ohnuki, T. Fujisawa, F. Abe, in: Proceedings of International Workshop on 2nd Structural Materials for Innovative Nuclear Systems, OECD Nuclear Energy Agency, J. Nucl. Mater. 417 (2011) 896−899.

23. PowerClean R, D&D Thematic Network, "Fossil Fuel Power Generation State-of the-Art", July 30, 2004.

24. Tulkki, V. "Supercritical Water Reactors", Master's Thesis, Helsinki University of Technology, November 2006.

25. GIF R&D Outlook for Generation IV Nuclear Energy Systems 21 August 2009

26. "A Technology Roadmap for Generation IV Nuclear Energy Systems", December 2002, Report GIF-002-00, U.S. DOE Nuclear Energy Research Advisory Committee and GIF, http://gif.inel.gov/roadmap/pdfs/gen iv roadmap.pdf (as in 21.10.2006)

27. Renate Cold work Workshop, Toronto, 2007.

28. ELECTRIC POWER RESEARCH INSTITUTE, BWR water chemistry guidelines, 2004 Edition.

29. ROSSKAMP M et al., VGB guideline for the water in nuclear power plants with light water reactors (BWR), VGB-R 401 J (2006).

30. ILEVBARE G., Proc. of Workshop on Cold Work in Iron-and Nickel-Base Alloys Exposed to High Temperature Water Environments, Toronto, 2007.

31. BRUEMMER S.M., CHARLOT L.A., HENAGER JR, C.H, Corrosion 44 (11) (1988) 782.

32. ANDERSEN P., HICKLING J., AHLUWALIA A., WILSON J., "Effect of H_2 on mitigation of PWSCC in nickel alloys," Optimization of Dissolved Hydrogen Content in PWR Primary Coolant (Int. Workshop, Tohuku University, Sendai, Japan, 2007).

33. MOLANDER A, et al., "Comparison of PWSCC initiation and crack growth data for alloy 600," Water Chemistry of Nuclear Reactor Systems (Int. Conf. Berlin, 2008).

34. PWSCC life time evaluation on alloy 690, 52 and 152 for PWR material, EPRI conf, June, 2007.

35. W.K. Boyd and H.A Pray, "Corrosion of Stainless Steels in Supercritical Water," Corrosion, 13 (1957) 375.

36. L. Fournier et al., "Stress Corrosion Cracking of Nickel Base Superalloys in Aerated Supercritical Water," NACE International Annual Conference, Corrosion 2001, Houston, TX, Paper 01361, pp. 1-11, 2001.

37. S. Teysseyre, Z. Jiao and G. S. Was, "Stress Corrosion Cracking of Austenitic Alloys in Supercritical Water", Corrosion, submitted

38. Y. Tsuchiya et al., "SCC and Irradiation Properties of Metals under Supercritical-Water Cooled Power Reactor Conditions," GENES4/ANP2003, Kyoto, Japan, Paper 1096, Sep. 15-19, 2003.

39. Y. Watanabe, H. Abe, Y. Diago and T. Nishida, "Corrosion Resistance and Cracking Susceptibility of 316L Stainless Steel in Sulfuric Acid-Containing Supercritical Water," Corrosion2004, NACE International, New Orleans, TX, Paper 04493, 2004

40. R. Fujisawa, et al., "Cracking Susceptibility of Ni Base Alloys and 316 Stainless Steel in Less Oxidizing or Reducing SCW," Corrosion2005, NACE International, Houston, TX, Paper 05395, 2005.

41. C. Bosch and D. Delafosse, "Stress Corrosion Cracking of Ni-Based and Fe-Based Alloys in Supercritical Water," Corrosion2005, NACE International, Houston, TX, Paper 05396, 2005.

42. L. Heikinheimo et al. "Materials for High Performance Light Water Reactors (EU-HPLWR)," SCWR Information Exchange Meeting, Pittsburgh, PA, June, 2004.

43. P. Ampornrat and G. S. Was, "Corrosion and Stress Corrosion Cracking of Ferritic-Martensitic Alloys in Supercritical Water," Proc. 12th International Conference on Environmental Degradation of Materials in Nuclear Power Systems – Water Reactors," The Minerals, Materials and Metals Society, Warrendale, PA, in press.

44. S. Kasahara, H. Matsui, F. Kano, N. Saito, M. Ookawa, J. Kaneda, in: Proceedings of Workshop on fueled loop tests for SCWR R&D, OECD/NEA, Paris, March, 2006.

45. A. Kimura et al., in: Proc. ICAPP'05, Seoul, Korea, Paper 5338, May, 2005.

46. H.S. Cho et al., J. Nucl. Mater. 329–333 (2004) 387.

Chapter 3

Stress Corrosion Cracking Susceptibility of ODS Ferritic Steel in Supercritical Pressurized Water Dissolved with Different Hydrogen and Oxygen Contents

3.1 Introduction

Supercritical pressurized water cooled reactor system has been considered as one of the candidates of Generation IV fission advanced nuclear systems as well as fusion systems because of its high thermal efficiency and simple reactor design [1]. In the supercritical water reactor (SCWR), the operation temperature is expected to be in the range 500 ~ 550 °C, and fuel claddings and the other core components are subjected to a potentially corrosive environment [2]. It is well known that the SCPW above critical point (374 °C, 22.1 MPa) is very severe environment for metallic materials being highly corrosive and it may cause stress corrosion cracking. For the application to the advanced nuclear systems, high performance is required for structural material in terms of its radiation resistance, weldability, creep strength, corrosion and stress corrosion cracking susceptibility, etc [3]. To meet these requirements, oxide dispersion strengthened ferritic steels have been developed as a high performance structural material for nuclear applications. Recent study showed that the corrosion resistance of the ODS ferritic steels in SCPW significantly increased with increasing Cr concentration up to 16 wt.%. And the addition of Al to about 4 wt.% made the ODS steels show excellent corrosion resistance to Pb-Bi eutectic coolant and SCPW [4].

There are several works on the SCC susceptibility of ODS steels, ferritic–martensitic (F/M) and austenitic steels at room and higher temperatures [5-9]. The existing data of austenitic and ferritic-martensitic steels at a temperature range from 380 °C to 550 °C in SCPW clearly showed a general decrease in the ultimate tensile stress with temperature. Teysseyre and Was [10] reported that the crack growth rate and maximum crack depth of austenitic stainless steels increased with increasing temperatures. In contrast, the observed dependence of strain to failure on temperature does not show any clear relationships with SCC susceptibility [1,6,10-14].

The selection of the strain rate is very important because the susceptibility to cracking may not be evident from the result of tests at too low or too high strain rate. In the previous works on SCC in a number of material-environment systems, strain rates in the range $10^{-5} \sim 10^{-6}$ s^{-1} are generally used and many of slow strain rate test (SSRT) in SCPW were conducted at strain rates faster than 10^{-7} s^{-1}. It was reported that low alloy steels become sensitive to the strain-induced corrosion cracking (SICC) at a strain rate of 1×10^{-6} s^{-1} in light water reactor system [15]. Nishimura and Maeda proposed that SCC-dominated strain rate region is from 10^{-4} s^{-1} to 10^{-6} s^{-1} for types 304 and 316 austenitic stainless steels in acidic chloride solutions at 80 °C [16]. Serebrinsky [17] investigated the effect of strain rate on the crack propagation rate (CPR), which was calculated by dividing the length of the brittle zone measured under the scanning electron microscope (SEM) by the fracture time, for FCC alloys in LiCl

solution at 130 °C, and showed that an increase in the strain rate enhanced the CPR. Therefore, more various range of strain rate test in SCPW is required for careful consideration of SCC susceptibility.

The dependence of SCC on DO content for ferritic-martnesitic steel in SCPW [18] as well as 304 austenitic steel and alloy 690 in high temperature water [19,20] were investigated, indicating that the thickness of the oxide layer grown on the specimen surface depended on DO content of the water.

Similarly, several experiments have been conducted on ODS alloys in sub-critical water [21]. Previous works demonstrated that ODS steels showed no susceptibility to SCC in a simulated boiling water reactor condition dissolved with oxygen, but did show in a SCPW. Corrosion behavior and SCC susceptibility in SCPW have been evaluated for austenitic and ferritic-martensitic steels [1,6,7,10-13,18,21], but few research groups studied on corrosion behavior of ODS steels in a SCPW [4,7,9,21-25]. In general, nickel-base alloys and austenitic stainless steels exhibited higher susceptibility to intergranular stress corrosion cracking (IGSCC) than ferritic–martensitic alloys. Meanwhile, ferritic-martensitic alloys suffer from severe oxidation. On the other hand, outstanding corrosion resistance of ODS steels to SCPW has been presented by several works on corrosion behavior of ODS steels in a SCPW. Therefore, one of the solutions to prevent SCC is the use of ODS ferritic steels, which has been considered to be resistant to SCC. However, the experimental data on the SCC susceptibility of ODS steels in SCPW are so limited.

In this study, the effect of strain rate on the deformation and fracture behavior was investigated to evaluate the susceptibility of ODS steel to SCC in SCPW dissolved with different hydrogen and oxygen contents.

3.2. Experimental

3.2.1. Specimen preparation

The material used in this study is a high Cr (15Cr) ODS ferritic steel (SOC-16) of which the chemical compositions are shown in Table 3.1. SOC-16 was manufactured by mechanical alloying method using a high speed attritor in KOBELCO. The mixed powders were encapsuled, hot extruded at 1150 °C and subsequently annealed at 1150 °C for 60 min followed by air cooling. The details of the fabrication process of the ODS steel are given in the previous papers [26,27]. Tensile specimens were sampled from the extruded bar with the loading direction parallel to the extruded direction. Round bar tensile specimens which measure a gauge section of 10 mm with 2.1 mm of diameter were

used for SSRT. The specimen geometry is shown in Fig. 3.1. The surface of the round bar specimens was mechanically polished by SiC abrasive paper to 4000 grit.

Table 3.1. Chemical compositions of ODS ferritic steel (SOC-16). wt%

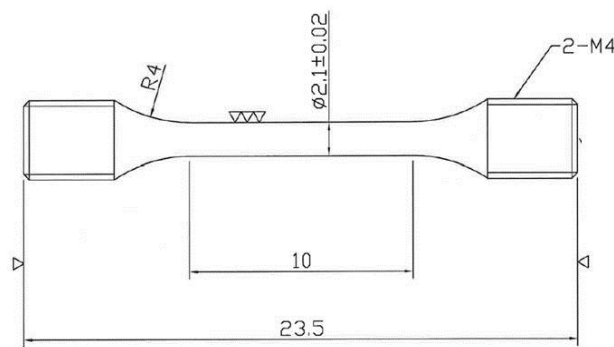| Material	C	Cr	W	Al	Ti	Y	O	N	Ar	Hf	Y_2O_3
SOC-16	0.043	14.54	1.93	3.01	0.13	0.28	0.17	0.006	0.0064	0.62	0.36

Fig. 3.1. The geometry of tensile specimens for SSRT in SCPW

3.2.2. SSRT conditions

In order to evaluate the susceptibility to SCC in SCPW, SSRT was carried out at strain rates of 1×10^{-3} s^{-1} and 1×10^{-6} s^{-1} or 5×10^{-7} s^{-1} in SCPW at 500 °C under a pressure of 25 MPa with different contents of dissolved oxygen and dissolved hydrogen. The DO and DH contents of the water were DH = 0.4 ppm, DO and DH < 0.01 ppm and DO = 8 ppm (mg/L). The water chemistry was controlled by injections of high purity nitrogen and hydrogen gas to a conditioning tank and the conductivity was lower than 0.10 µS/cm during experiment. In addition, tensile tests in a vacuum of 2.0×10^{-3} Pa were also performed at 500 °C to compare with the deformation and fracture behavior in SCPW. After the SSRT, fractured surface and side surface of the gauge section were observed by SEM to investigate the fracture mode in detail. Electron probe microanalyzer (EPMA) analysis was also conducted for the cross-sectional areas of the tensile specimens to understand the roll of corrosion products. The cracking pass way was examined by the cross-sectional observation to measure the crack depth and to count the number of cracks.

3.3. Results and discussion

3.3.1. Stress-strain behavior

The SSRT stress–strain curves of SOC-16 deformed in a vacuum and SCPW dissolved with different DO and DH are shown in Fig. 3.2 (a) for the test at a higher strain rate (1×10^{-3} s^{-1}) and Fig. 3.2 (b) for the test at a lower strain rate (1×10^{-6} s^{-1} or 5×10^{-7} s^{-1}). Table 3.2 summarized the numerical values of the tensile properties obtained by the SSRT. Both the figures indicate that there is no significant effect of test environment on the stress-strain behavior of the ODS steel irrespective of the strain rate, although the yield stress and ultimate tensile stress are decreased with decreasing strain rate, while the total elongation tends to increase with decreasing strain rate. This behavior is a typical strain rate effect for metallic materials because a decreased strain rate gives more time for dislocations to move past obstacles as a thermally activation process. The obtained tensile test results suggest that there is no susceptibility to SCC of the ODS steel in the SCPW.

Generally, the susceptibility to SCC can be evaluated by measuring the reduction of total elongation and the change in the fracture mode from ductile to brittle fracture, IGSCC and transgranular stress corrosion cracking (TGSCC). In our previous work on the SCC of a martensitic steel in SCPW, a remarkable fracture mode change from ductile to brittle mode was accompanied by lowering strain rate, while the total elongation of the steel was not affected by the strain rate change [1]. Therefore, the susceptibility to SCC can be more clearly evaluated by the observation of fracture mode change and the measurement of reduction in area (RA). Fig. 3.3 shows the RA of the tensile specimens after SSRT at different strain rates, indicating that the RA is almost independent of the test environment and strain rate. This also suggests that the ODS steel is not susceptible to SCC in SCPW at this experimental condition.
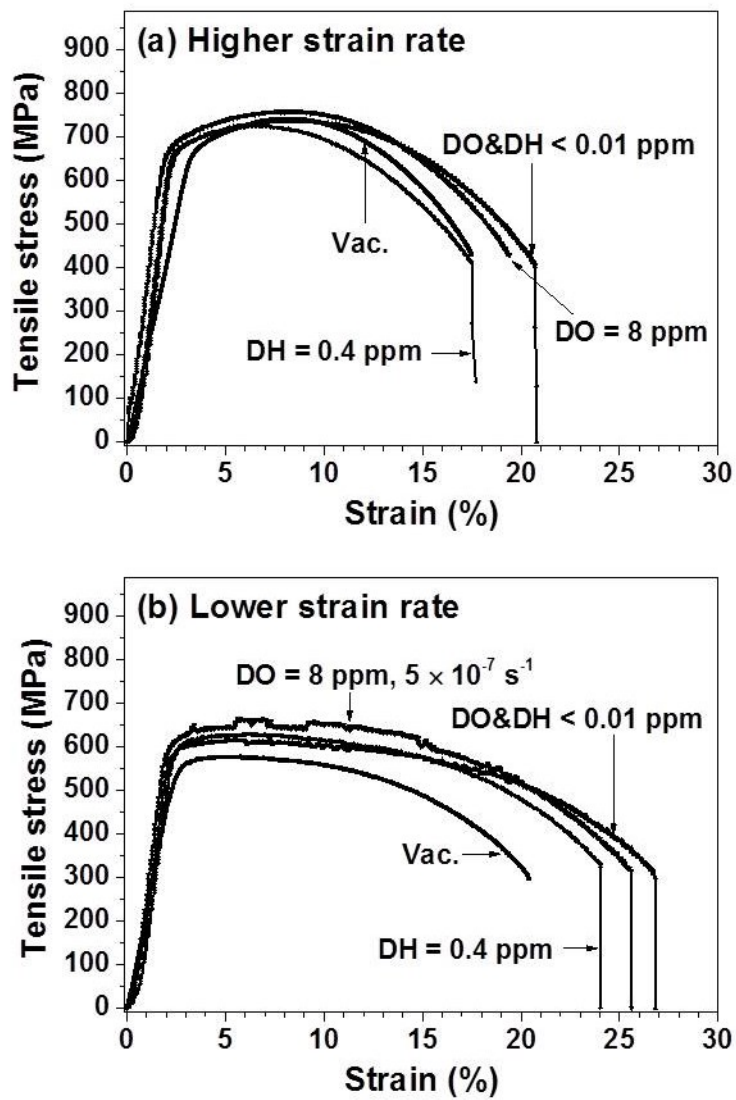
Fig. 3.2. SSRT stress-strain curves tested at (a) higher strain rate of 1×10^{-3} s^{-1} and (b) lower strain rate of 1×10^{-6} s^{-1} or 5×10^{-7} s^{-1} in vacuum and SCPW (DH = 0.4 ppm, DO & DH < 0.01 ppm and DO = 8 ppm)

Table 3.2. SSRT data for ODS ferritic steel in vacuum and SCPW

| Environments	Strain rate	Yield stress (MPa)	Ultimate tensile stress (MPa)	Total elongation (%)	Reduction in area (%)
Vacuum	1×10^{-3} s^{-1} (higher)	667	742	17.5	70.4
	1×10^{-6} s^{-1} (lower)	527	579	20.4	68.3
SCPW DH = 0.4 ppm	1×10^{-3} s^{-1} (higher)	655	725	17.7	70.5
	1×10^{-6} s^{-1} (lower)	592	630	24	67.8
SCPW DO&DH < 0.01 ppm	1×10^{-3} s^{-1} (higher)	662	736	20.8	70.3
	1×10^{-6} s^{-1} (lower)	579	615	26.8	70.8
SCPW DO = 8.0 ppm	1×10^{-3} s^{-1} (higher)	662	760	19.4	69.7
	5×10^{-7} s^{-1} (lower)	602	665	25.6	73.2
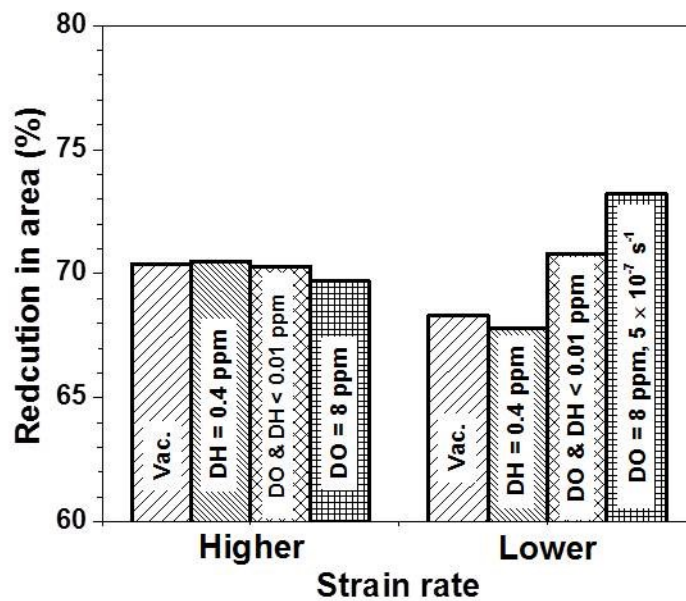
Fig. 3.3. Reduction in area of ODS ferritic steel after SSRT at higher (1×10^{-3} s^{-1}) and lower (1×10^{-6} s^{-1} or 5×10^{-7} s^{-1}) strain rates.

55

3.3.2. Fracture behavior

3.3.2.1. Fracture mode

To investigate the fracture behavior, SEM observations of the fractured surface and the specimen side surface in the necking region were carried out and shown in Fig. 3.4 and 3.5 deformed at higher and lower strain rates, respectively. The results of the SEM observations are in good agreement with those obtained by the measurement of RA. In all the tested specimens regardless of the strain rate, a typical ductile fracture was observed showing a cup and corn facture shape with necking accompanied by the formation of very fine dimples on the fractured surface. However, detailed observations of the side surface revealed that some cracks randomly oriented exist in the necking region deformed at both higher and lower strain rates in SCPW, while no such a crack was observed in the specimen deformed in vacuum at higher strain rate. Furthermore, the cracks at the higher strain rate in SCPW (Fig. 3.4b~d) are more or less similar to those formed in vacuum at the lower strain rate of 1×10^{-6} s^{-1} (Fig 3.5a). Therefore, it is considered that the cracks in the specimen tested in vacuum at the lower strain rate (Fig. 3.5a) are formed in the oxide layer produced during the test for about 60 hours at 500 °C, although the oxidation rate is low in the vacuum of 2.0×10^{-3} Pa. The cracks observed in SCPW at the lower strain rate (Fig. 3.5b~d) show somewhat different patterns, which were located at only near the necking region, but not observed at the other gauge part of the specimen. Furthermore, these cracks were formed along random direction to the tensile direction. The fractured surface observation also indicates that the cracks were limited at the peripheral region of the fractured surface. In the case of austenitic stainless steels in high temperature water and SCPW, however, it was reported that a plenty of cracks were initiated suddenly and tended to be distributed in the direction perpendicular to the loading direction and the cracks were distributed over the whole surface of the specimen gauge [1,12,28].
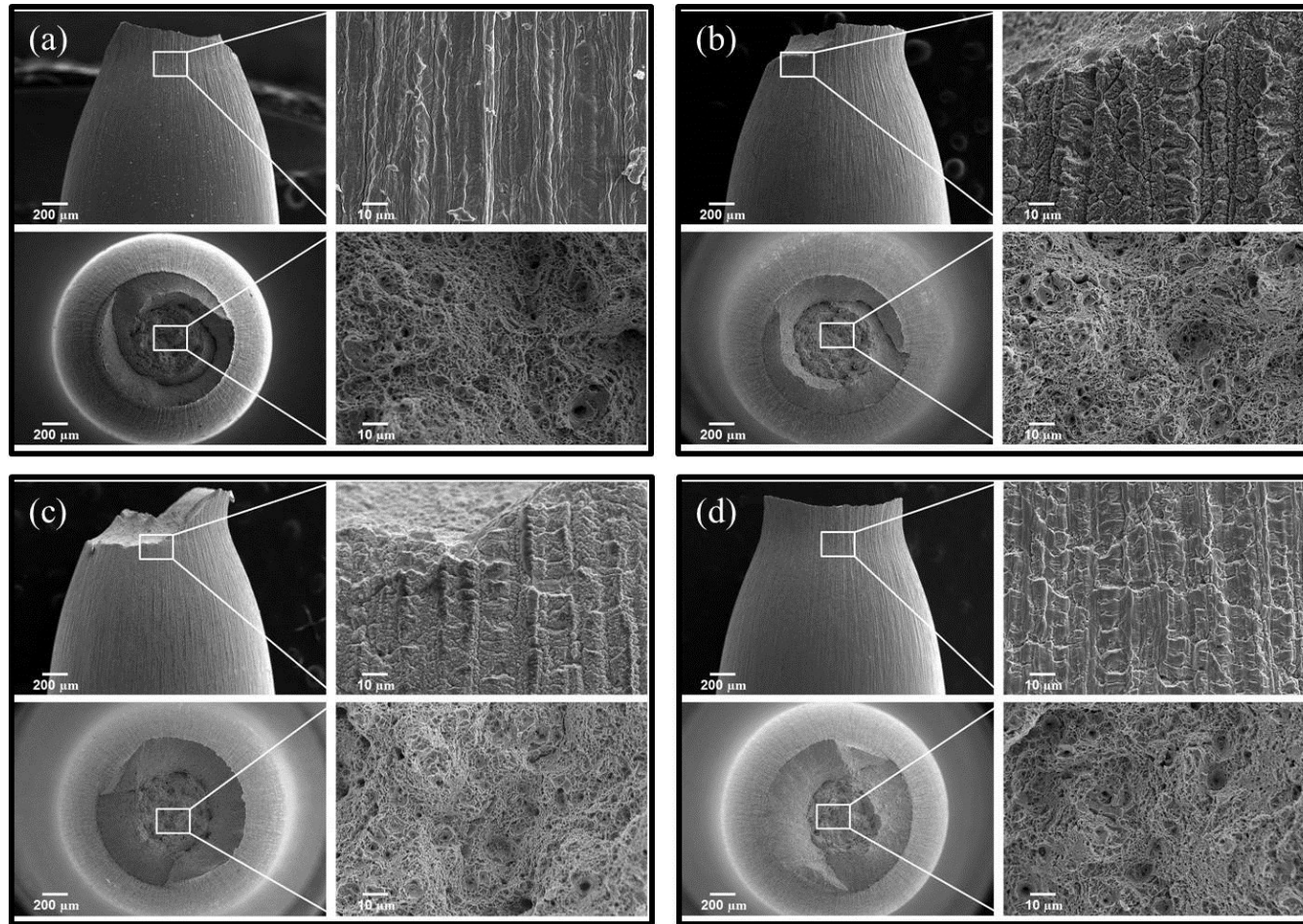
Fig. 3.4. SEM images of fracture surface and gauge section of the ODS steel after SSRT at a higher strain rate of 1×10^{-3} s^{-1}. (a : vacuum, b : SCPW with DH 0.4 ppm, c : SCPW with DO & DH < 0.01 ppm, d : SCPW with DO 8.0 ppm)
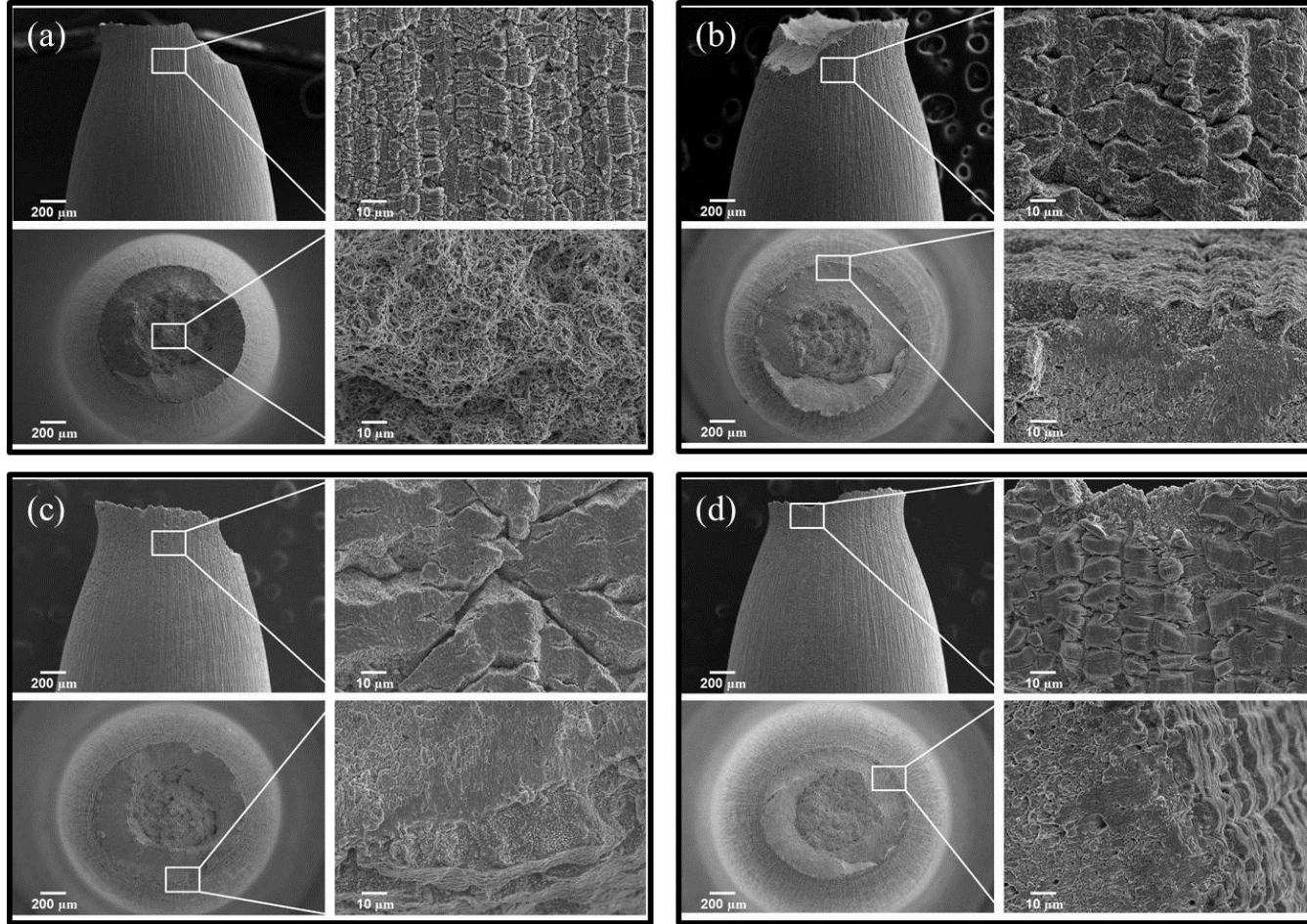
Fig. 3.5. SEM images of fracture surface and gauge section of the ODS steel after SSRT at lower strain rate of 1×10^{-6} s^{-1} or 5×10^{-7} s^{-1}. (a : vacuum - 1×10^{-6} s^{-1}, b : SCPW with DH 0.4 ppm - 1×10^{-6} s^{-1}, c : SCPW with DO & DH < 0.01 ppm - 1×10^{-6} s^{-1}, d : SCPW with DO 8.0 ppm - 5×10^{-7} s^{-1})

3.3.2.2. Analysis of corrosion products

In order to understand the role of corrosion products, EPMA analysis was conducted for the cross-sectional areas in the homogeneously deformed region of the tensile specimens after SSRT in SCPW at the lower strain rates. As shown in Fig. 3.6, the results revealed that all the corrosion products were Fe/Cr/Al oxide layers, even in the dissolved hydrogen environment. The oxide layers were classified into two layers, an outer Fe-rich oxide layer and an inner Cr and Al-rich complex oxide layer. The formation of the oxide layers can be explained based on an outward diffusion of iron ions which will produce the outer layer, while an inward diffusion of oxygen forms the inner oxide layer. The interesting is that the EPMA results indicate that the oxide layer formed in the water with DO 8 ppm is thinner than that of DH 0.4 ppm and DO & DH < 0.01 ppm. This phenomenon can be interpreted in terms of Al effects that the addition of Al to 15Cr ODS ferritic steel suppresses the corrosion by the formation of very thin Cr/Al rich complex oxide layer. As shown in Fig. 3.6, the inner Cr/Al complex oxide layer was formed on all the specimen surfaces irrespective of the water condition, which interrupts the growth of the outer Fe oxide layer, resulting in the suppression of the entire corrosion. The oxide layer thickness depends on the DO/DH contents and the thickness of the Cr/Al complex oxide film is thinnest for the specimen tested in DH=0.4 ppm. In other words, SCPW dissolved with extremely low oxygen contents interrupts the creation of the Cr/Al complex layer and gives rise to thicker outer oxide layer in DH = 0.4 ppm and DO & DH < 0.01 ppm.

Fig. 3.7 shows oxide layer thickness of highly deformed necking portion and less deformed gage portion after SSRT at the lower strain rates. The thicknesses of the thin oxide layer in the less deformed portion show a good correspondence to the EPMA results. On the other hand, the thick oxide layers of highly deformed part such as near the necking region are thicker than those of the less deformed part. This difference could be the evidence that the deformation accelerates corrosion by introducing fresh surface for corrosion. However, the water chemistry effect tis negligible to the fracture behavior of the ODS steel in SCPW.

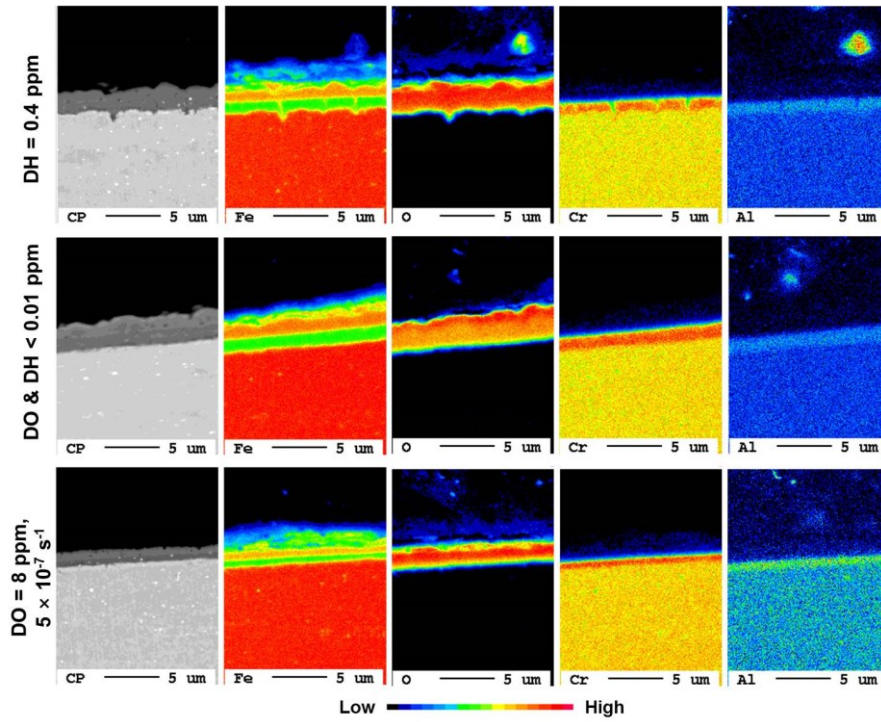Fig. 3.6. EPMA analysis results of cross sectional area of the specimens after SSRT in SCPW at lower strain rate of 1×10^{-6} s^{-1} or 5×10^{-7} s^{-1} (scale shows the relative concentration).
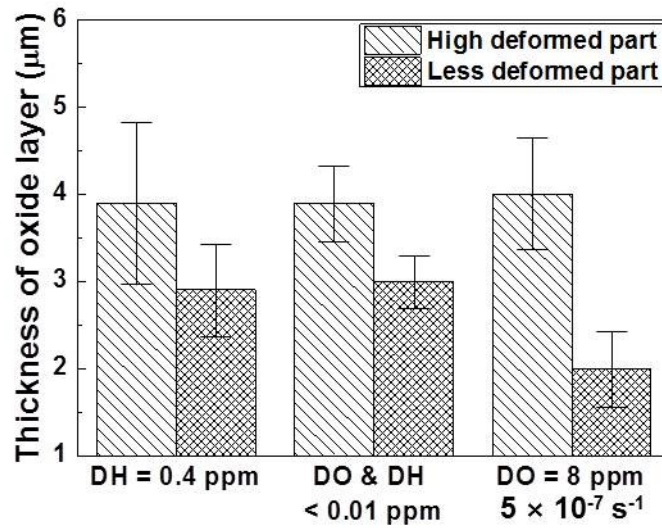

Fig. 3.7. Oxide layer thickness of highly deformed necking portion and less deformed gage portion after SSRT at lower strain rate of 1×10^{-6} s^{-1} or 5×10^{-7} s^{-1}

In the previous work by Was et al., they reported the corrosion behavior of austenitic steels and ferritic-martensitic steels in SCPW, where the oxide layer developed in ferritic–martensitic steels was stable, maintained a constant average density and was difficult to be broken. It is also reported that in many of the austenitic stainless steels with higher bulk concentrations of nickel and chromium, the outer oxide layer had a tendency to spall [10]. And the oxide layer of high Cr ODS steels in SCPW consisted of magnetite and hematite [23, 24], which was similar to high Cr austenitic stainless steels. In this research on the ODS steel, cracks and pores were also observed in the outer layer of the magnetite and the oxide layer tended to spall.

3.3.2.3. Correlation of growth rate of corrosion products and diffusion of elements

The thickness of corrosion products can be estimated based on the diffusivity of elements, such as Fe, Cr, Al and O through the oxides. As the oxide grows thicker the required diffusion distance increases, which may result in the decreasing of the oxidation rate. Theoretically, oxidation should follow parabolic behavior. Oxidation kinetics can be determined by one of two processes; diffusion of Fe cations through the oxide to the oxide-water interface, or diffusion of O anions through the oxide to the metal-oxide interface.

The diffusion coefficients were calculated by the equation of diffusion distance;

$$S = \sqrt{4Dt} \qquad\qquad (3.1)$$

or,
$$D = S^2t/4 \qquad\qquad (3.2)$$

where S is the diffusing distance (cm), D is the diffusion coefficient (cm^2/s) and t is the time (s).

S was obtained from Fig 3.7, and t is available from the strain rate and strain to fracture in each test. The values of calculated diffusion coefficient are summarized in Table 3.3.

Table 3.3. Diffusion coefficients of O and Fe in the oxide layer of less deformed gage portion after SSRT at lower strain rate (1×10^{-6} s^{-1} or 5×10^{-7} s^{-1}) (cm^2/s)

	$D_{\text{DH} = 0.4 \text{ ppm}}$	$D_{\text{DO \& DH} < 0.01 \text{ ppm}}$	$D_{\text{DO} = 8 \text{ ppm}}$
Fe	3.15×10^{-14}	3.40×10^{-14}	4.88×10^{-15}
O	1.40×10^{-14}	1.11×10^{-14}	4.88×10^{-15}

Table 3.4 lists the selected diffusion data of Fe and O ions in oxides from literature, which is compared with the calculated diffusion coefficient of Table 3.3. As shown in Table 3.4, Experiments conducted with poly-crystal oxide specimens provided higher diffusivities than those of single-crystal oxide specimen, and the diffusion of Cr is too slow to influence the oxidation mechanism, thus it is negligible. Comparing Table 3.3 with Table 3.4, the diffusion coefficients of O and Fe in the oxide formed on 15Cr-4Al ODS ferritic steel are much lower than that of the O and Fe in the oxide formed on conventional Fe-Cr steels. This implies that the rate controlling mechanism of oxidation in the ODS steel is different from the other steels.

Table 3.4. Diffusion coefficients of Fe, Cr and O in Fe_3O_4, Fe-Cr spinel oxide and Cr_2O_3

Oxide	Ions	Temp. (°C)	Diffusion coefficient (D) (cm^2/s)	Note : (S) Single crystal, (P) Polycrystal	Ref.
Fe_3O_4	O	500-800	3.50×10^{-6}	(S) 20-200 MPa hydrothermal with O^{18}	[29]
Fe_3O_4	Fe	350-1200	4.51×10^{-5}	(P) Fe^{55} in Fe_3O_4, averaged from $P_{O2}=10^{-28} - 10^{-18}$ atm	[30]
$FeCr_2O_4$	O	600-1000	1.61×10^{-5}	(P) O^{18} radiotracer on Fe-Cr alloy	[31]
Fe_3O_4	Fe	1200	6.71×10^{-9}	(P) Fe^{59} tracer	[32]
Fe_3O_4	Cr	1200	1.54×10^{-11}	(P) Cr^{51} tracer	[32]
Cr_2O_3	Cr	800	5.90×10^{-18}	Bulk	[33]
Cr_2O_3	Cr	800	1.10×10^{-12}	Grain boundary	[33]
Cr_2O_3	O	800	2.60×10^{-18}	Bulk	[33]
Cr_2O_3	O	800	5.90×10^{-13}	Grain boundary	[33]

The oxidation kinetic equation of the ODS steel can be estimated by obtaining the oxidation parabolic constant k_P. If oxidation film was very stable and was not broken off, the oxidation curves generally obey a parabolic law:

$$(\Delta m)^2 = k_P t. \qquad (3.3)$$

Assuming that the oxide layer consists of Cr_2O_3, the k_C value defined as $x^2 = k_C t$ (x: oxide thickness) is expressed by:

$$k_C = \left(\frac{M_{Cr_2O_3}}{3M_O\rho_{Cr_2O_3}}\right)^2 k_P \tag{3.4}$$

where $M_{Cr_2O_3}$ is the molar mass of Cr_2O_3 and M_O is the molar mass of oxygen atom and $\rho_{Cr_2O_3}$ is the density of Cr_2O_3. It is necessary to consider the effective diffusion coefficients (D_{eff}^{ox}) in the oxide layer [34] which take into account diffusion in the bulk, D_{bulk}^{ox}, and along grain boundaries, D_{gb}^{ox}, according to:

$$D_{eff}^{ox} = (1-f)\,D_{bulk}^{ox} + D_{gb}^{ox} \tag{3.5}$$

where f is the fraction of atoms diffusion along grain boundaries, commonly given by:

$$f = \frac{3\delta}{\phi} \tag{3.6}$$

where δ is the grain boundary width arbitrarily taken as 1 nm, and ϕ is the oxide grain size [34].

From the classical equation given by Wagner, which relates the parabolic oxidation constant k_C to the diffusion coefficients for an oxide M_aO_b, k_C can be expressed [33]:

$$k_C(\text{calc.}) = \int_{P_{O_2}^{int}}^{P_{O_2}^{ext}} \left[D_{anion}^{ox} + \frac{b}{a} D_{cation}^{ox}\right] d\ln(P_{O_2}) \tag{3.7}$$

$P_{O_2}^{ext}$: oxygen pressure at gas/scale interface; $P_{O_2}^{int}$: oxygen pressure at the alloy/scale interface and D_{anion}^{ox} and D_{cation}^{ox}: anion and cation diffusion coefficients in oxide layer.

Writing $D = D°(p_{O_2})^n$ for each species ($D°$ being the diffusion coefficient at $p_{O_2} = 1$ atm) and considering that self-diffusion occurs by O_i and V_{Cr}:

$$k_C = \int D_O°(p_{O_2})^{1/6} d\ln(p_{O_2}) + \frac{3}{2}\int D_{Cr}°\left(p_{O_2}\right)^{3/16} d\ln(p_{O_2})$$

$$= 6D_O°(p_{O_2}^{ext})^{1/6} + 8D_{Cr}°(p_{O_2}^{ext})^{3/16} \tag{3.8}$$

$$= 6D_O°(0.1\ \text{atm}) + 8D_{Cr}°(0.1\ \text{atm})$$

In our previous research, H.S. Cho [35] calculates the diffusion coefficients of Cr and O in the oxide layer formed on high Cr (14-22 wt%) ODS steels at 510 °C in SCPW by using diffusion data in

a literature [36] and the result was shown in Table 3.5.

Table 3.5. Diffusion coefficients of Cr and O in the oxide layer formed on high Cr (14-22 wt%) ODS steels at 510 °C in SCPW

Element	D_{bulk}^{ox}	D_{gb}^{ox}	D_{eff}^{ox}
Cr	1.73×10^{-19}	6.88×10^{-15}	4.14×10^{-17}
O	1.20×10^{-23}	7.74×10^{-15}	4.64×10^{-17}

The calculated diffusion coefficients by using experimental data in this research (see Table 3.3) exhibits approaching value of the grain boundary diffusion coefficients (see Table 3.5). This implies that the grain boundary diffusion plays an important role in the oxide formation of the 15Cr-4Al ODS steel.

Although grain boundary diffusion, which is faster than the bulk or effective diffusion, was mainly occurred, the thickness of oxide layer on the ODS steel is very thin. It indicates that diffusivity of ions in the oxide layer on ODS steel in SCPW is slower than the effective diffusion of ions in oxide on conventional steels. It should be noted that the thickness of the oxide layer on the ODS steel is almost similar regardless of the water chemistry. Therefore, it can be suggested that the grain boundary diffusion mechanism of the 15Cr-4Al ODS steel could be affected by nano-particles and presence of Al-Cr rich complex oxide layer.

3.3.2.4. Cracks on specimen side surface

To make clear the relation of oxide layer with cracks produced in the ODS steel, cross-sectional observation was carried out to measure the crack depth and to count the number of the cracks in the necking part up to 1.2 mm far away from the edge of the cup and corn fractured surface. Fig. 3.8 indicates that the crack depth tends to deeper when the deformation is more severe, that is, near fractured portion. In all cases cracks were only observed in necking region and no crack was observed in the region far beyond 1.2 mm away from the fractured surface. The maximum crack depth was observed on the specimen tested with DH = 0.4 ppm at lower strain rate of 1×10^{-6} s^{-1}, which does not

exceed 25 μm. It should be noted that the number of cracks on the ODS steel was not influenced by the strain rate, although much more surface cracks on gauge section were observed in the test in DO = 8 ppm water at a strain rate of 5×10^{-7} s^{-1} (Fig. 3.5d).
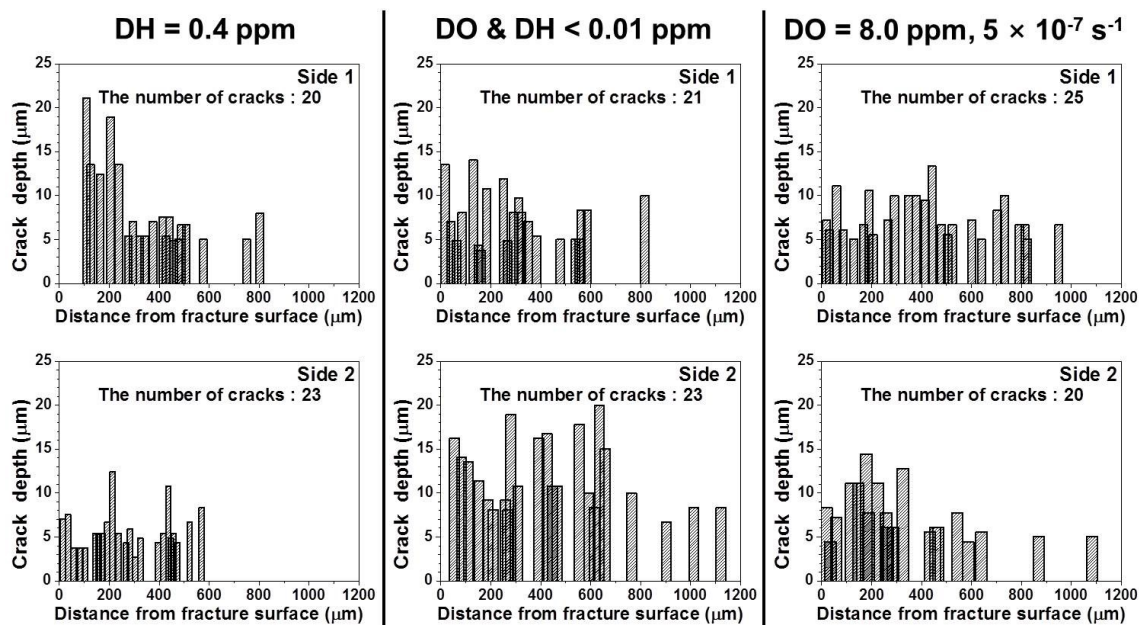

Fig. 3.8. The number and depth of cracks according to the distance from fractured surface after SSRT deformed at lower strain rate of 1×10^{-6} s^{-1} or 5×10^{-7} s^{-1} in SCPW. Side 1 and 2 are the bottom and top side of the cross sectional area of the specimens in Fig. 3.9

The deeper cracks were also covered by the almost same level of oxide layer as shown in Fig. 3.9, indicating that the cracks are limited in the necking region and are very shallow. Based on the results above, the crack development of ODS steel in SCPW can be explained in terms of "corrosion layer cracking" model of Fig. 3.10. First, oxide layer rupture is occurred in the necking region through a large deformation (Fig. 3.10a), because the oxide layer has no enough ductility. Once oxide layer cracking occurred, a fresh metallic surface is introduced, and corrosion proceeds by the outward diffusion of iron ions and the inward diffusion of oxygen (Fig. 3.10b). Finally, the successively formed new oxide layer at the front of the crack is deformed and new cracks are introduced in the layer (Fig. 3.10c). This crack development of ODS steel which is nano-crystalline material does not significantly affect its tensile property, although Irvin R. Kramer and Louis J. Demer [37] report that

oxide films on surface influence the mechanical properties of materials. This is because the influence of the films is considerably larger for single crystals than for polycrystalline materials, as they also mentioned in the report.
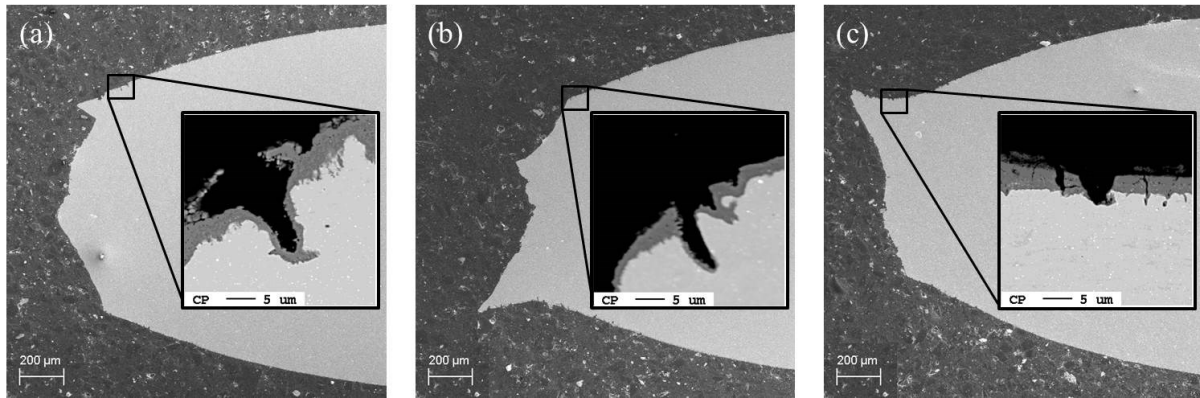
Fig. 3.9. Cross-sectional SEM images of specimens showing cracks after SSRT at lower strain rate in SCPW. (a : DH 0.4 ppm - 1×10^{-6} s^{-1}, b : DO & DH < 0.01 ppm - 1×10^{-6} s^{-1}, c : DO 8.0 ppm - 5×10^{-7} s^{-1},)

Fig. 3.10. Schematic view of "corrosion layer cracking" model of ODS steel in SCPW.

From the macroscopic analysis, the deformation and fracture behavior of the ODS steel in SCPW are not sensitive to the change in the contents of DH and DO of SCPW.

3.4. Conclusions

SCC susceptibility and fracture mode of a 15Cr-4Al-2W ODS ferritic steel in SCPW (500 °C, 25 MPa) dissolved with DH = 0.4 ppm, DH = DO = 0 ppm and DO = 8 ppm were investigated by means of SSRT. The main results obtained are the followings:
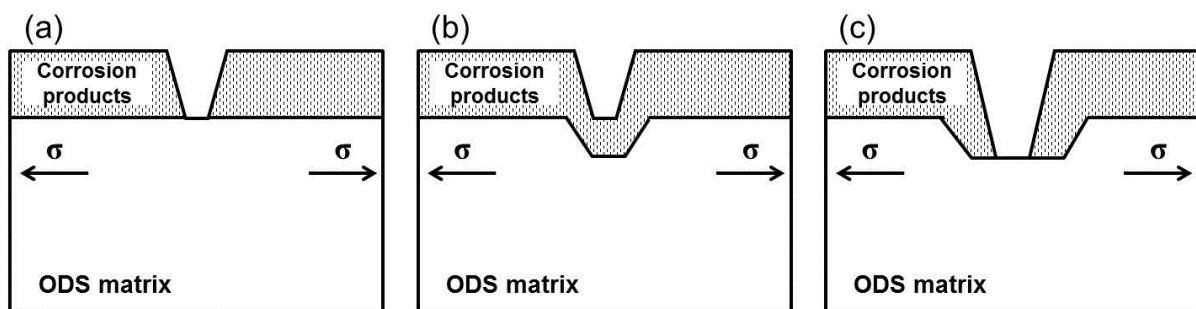
1) The deformation and fracture behavior of the ODS steel are independent of the test conditions, such as strain rate, environment namely vacuum or SCPW and DH/DO contents in SCPW. All the tested specimens shows a ductile fracture showing a cup and corn shape of fractured region.

2) The effect of DH and DO contents on the fracture behavior is negligible for the ODS steel.

3) The high resolution EPMA observations revealed that oxide layer thickness depends on the DO/DH contents and the thickness of the Cr/Al complex oxide film is thickest for the specimen tested in DH=0.4 ppm. In other words, SCPW dissolved with extremely low oxygen contents interrupts the creation of the Cr/Al complex oxide layer and gives rise to thicker outer oxide layer in DH = 0.4 ppm and DO & DH < 0.01 ppm.

4) The detailed EPMA and SEM analysis showed that small "corrosion layer cracking" was observed in the necking region of all the tested specimens except for that tested in vacuum at higher strain rate. The number of the oxide layer cracks was not influenced by the change in the strain rate ranging from 1×10^{-3} s^{-1} to 5×10^{-7} s^{-1}.

5) The diffusion process of the ODS steel in SCPW follows grain boundary diffusion mechanism. Although grain boundary diffusion, which is faster than the bulk or effective diffusion, was mainly occurred, the thickness of oxide layers on the ODS steel is very thin and similar, regardless of the water chemistry. Therefore, it can be suggested that the grain boundary diffusion mechanism of the 15Cr-4Al ODS steel could be affected by nano-particles and presence of Al-Cr rich complex oxide layer.

6) After the test in vacuum at a strain rate of 5×10^{-7} s^{-1}, the corrosion layer cracking was observed, indicating that the small amount of oxygen in the vacuum may cause corrosion and corrosion layer cracking in necking area.

7) The 15Cr-ODS ferritic steel shows no susceptibility to SCC in SCPW in the test condition of this research.

References

1. N. Muthukumar, J.H. Lee, A. Kimura, SCC behavior of austenitic and martensitic steels in supercritical pressurized water, J. Nucl. Mater. 417 (2011) 1221–1224

2. Arthur T. Motta, Aylin Yilmazbayhan, Marcelo J. Gomes da Silva, Robert J. Comstock, Gary S. Was, Jeremy T. Busby, Eric Gartner, Qunjia Peng, Yong Hwan Jeong, Jeong Yong Park, Zirconium alloys for supercritical water reactor applications: Challenges and possibilities, J. Nucl. Mater. 371 (2007) 61-75.

3. Y. Watanabe, H. Abe, Y. Daigo, T. Nishida, Environmentally Assisted Cracking of Sensitized Stainless Steel in Supercritical Water : Effects of Physical Property of Water, GENES4/ANP2003, (2003) Paper 1183

4. A. Kimura, R. Kasada, N. Iwata, H. Kishimoto, C.H. Zhang, J. Isselin, P. Dou, J.H. Lee, N. Muthukumar, T. Okuda, M. Inoue, S. Ukai, S. Ohnuki, T. Fujisawa, T.F. Abe, Development of Al added high-Cr ODS steels for fuel cladding of next generation nuclear systems, J. Nucl. Mater. 417 (2011) 176-179.

5. Ramar, P. Spätig, R. Schaublin, Analysis of high temperature deformation mechanism in ODS EUROFER97 alloy, J. Nucl. Mater. 382 (2008) 210–216.

6. Seong Sik Hwang, Byung Hak Lee, Jung Gu Kim, Jinsung Jang, SCC and corrosion evaluations of the F/M steels for a supercritical water reactor, J. Nucl. Mater. 372 (2008) 177–181.

7. H.S. Cho, H. Ohkubo, N. Iwata, A. Kimura, S. Ukai, M. Fujiwara, Improvement of compatibility of advanced ferritic steels with super critical pressurized water toward a higher thermally efficient water-cooled blanket system, Fusion Eng. Des. 81 (2006) 1071–1076.

8. Zhanpeng Lu, Tetsuo Shoji, Yoichi Takeda, Yuzuru Ito, Seiya Yamazaki, The dependency of the crack growth rate on the loading pattern and temperature in stress corrosion cracking of strain-hardened 316L stainless steels in a simulated BWR environment, Corros. Sci. 50 (2008) 698–712.

9. J.H. Lee, R. Kasada, A. Kimura, T. Okuda, M. Inoue, S. Ukai, S. Ohnuki, T. Fujisawa, F. Abe, Influence of alloy composition and temperature on corrosion behavior of ODS ferritic steels,

J. Nucl. Mater. 417 (2011) 1225–1228.

10. G.S. Was, P. Ampornrat, G. Gupta, S. Teysseyre, E.A. West, T.R. Allen, K. Sridharan, L. Tan, Y. Chen, X. Ren, C. Pister, Corrosion and stress corrosion cracking in supercritical water, J. Nucl. Mater. 371 (2007) 176–201

11. T. Hirose, K. Shiba, M. Enoeda, M. Akiba, Corrosion and stress corrosion cracking of ferritic/martensitic steel in super critical pressurized water, J. Nucl. Mater. 367–370 (2007) 1185–1189

12. R. Novotny, P. Hähner, J. Siegl, P. Haušild, S. Ripplinger, S. Penttilä, A. Toivonen, Stress corrosion cracking susceptibility of austenitic stainless steels in supercritical water conditions, J.Nucl.Mater. 409 (2011) 117-123

13. S. Teysseyre, Z. Jiao, E. West, G.S. Was, Effect of irradiation on stress corrosion cracking in supercritical water, J. Nucl. Mater. 371 (2007) 107-117

14. Masahiro Nono, Tetsuya Nakajima, Masahiro Iwama, Ryuta Kasada, Akihiko Kimura, SCC behavior of SUS316L in the high temperature pressurized water environment, J. Nucl. Mater. 417 (2011) 878-882

15. E. Lenz, N. Wieling, Strain-induced corrosion cracking of low-alloy steels in LWR-systems – Interpretation of susceptibility by means of a three dimensional diagram, Ncul. Eng. and Design. 91 (1986) 331-344.

16. R. Nishimra, Y. Maeda, SCC evaluation of type 304 and 316 austenitic stainless steels in acidic chloride solutions using the slow strain rate technique, Corrosion Science 46 (2004) 769-785

17. S.A Serebrinsky, J.R. Galvele, Effect of the strain rate on stress corrosion crack velocities in face-centred cubic alloys. A mechanistic interpretation, Corrosion Science 46 (2004) 591-612

18. Nai-qiang Zhang, Hong Xu, Bao-rang Li, Yang Bai, Dong-yu Liu, Influence of the dissolved oxygen content on corrosion of the ferritic-martensitic steel P92 in supercritical water, Corrosion Science 56 (2012) 123-128

19. Wenjun Kuang, Xinqiang Wu, En-Hou Han, Influence of dissolved oxygen concentration on the oxide film formed on 304 stainless steel in high temperature water, Corrosion Science 63 (2012) 259-266

20. Wenjun Kuang, Xinqiang Wu, En-Hou Han, Influence of dissolved oxygen concentration on the oxide film formed on Alloy 690 in high temperature water, Corrosion Science 69 (2013) 197-204

21. A. Kimura, H.S. Cho, N. Toda, R. Kasada, H. Kishimoto, N. Iwata, S. Ukai, M. Fujiwara, Fuel cladding materials R&D for high burn-up operation of advanced water-cooling nuclear energy systems, Proceedings of the 2005 International Congress on Advances in Nuclear Power Plants (ICAPP '05), Seoul, Korea, 2005, p. 5338.

22. H.S. Cho, A. Kimura, S. Ukai, M. Fujiwara, Corrosion properties of oxide dispersion strengthened steels in super-critical water environment, J. Nucl. Mater. 329–333 (2004) 387-391.

23. Helong Hu, Zhangjian Zhou, Ming Li, Lefu Zhang, Man Wang, Shaofu Li, Changchun Ge, Study of the corrosion behavior of a 18Cr-oxide dispersion strengthened steel in supercritical water, Corrosion Science 65 (2012) 209-213

24. J. Isselin, R. Kasada, A. Kimura, Corrosion behaviour of 16%Cr-4%Al and 16%Cr ODS ferritic steels under different metallurgical conditions in a supercritical water environment, Corrosion Science 52 (2010) 3226-3270

25. Yun Chen, Kumar Sridharan, Shigeharu Ukai, Todd R. Allen, Oxidation of 9Cr oxide dispersion strengthened steel exposed in supercritical water, J.Nucl.Mater. 371 (2007) 118-128

26. S. Ukai, T. Nishida, T. Okuda, T. Yoshitake, R&D of oxide dispersion strengthened ferritic martensitic steels for FBR, J. Nucl. Mater. 258-263 (1998) 1745-1749.

27. Shigeharu Ukai, Shunji Mizuta, Tunemitsu Yoshitake, Takanari Okuda, Masayuki Fujiwara, Shigeki Hagi, Toshimi Kobayashi, Tube manufacturing and characterization of oxide dispersion strengthened ferritic steels, J. Nucl. Mater. 283–287 (2000) 702-706.

28. Masayuki Kamaya, Takumi Haruna, Crack initiation model for sensitized 304 stainless steel in high temperature water, Corrosion Science 48 (2006) 2442-2456.

29. Giletti, B.J. and K.C. Hess, Oxygen diffusion in magnetite. Earth and Planetary Science Letters, 1988. 89: p. 115-122.

30. Atkinson, A., M.L. O'Dwyer, and R.I. Taylor, 55Fe Diffusion in Magnetite Crystal at 500 °C

and its Relevance to Oxidation of Iron. Journal of materials science, 1983. 18: p. 2371-2379.

31. Horita, T., et al., Diffusion of oxygen in the scales of Fe-Cr alloy interconnects and oxide coating layer for solid oxide fuel cells. Solid State Ionics, 2008. 179(38): p. 2216-2221.

32. Töpfer, J., S. Aggarwal, and R. Dieckmann, Point defects and cation tracer diffusion in (CrxFe1 - x)3 - [delta]O4 spinels. Solid State Ionics, 1995. 81(3-4): p. 251-266.

33. Tsai, S.C., A.M. Huntz, and C. Dolin, Growth Mechanism of Cr_2O_3 Scales: Oxygen and chromium diffusion, oxidation kinetics and effect of yttrium. Materials Science and Engineering, 1996. A212: p. 6-13.

34. A. M. Huntz, Parabolic laws during high temperature oxidation: relations with the grain size and thickness of the oxide, J. Mater. Sci. Letters 18 (1999) 1981-1984

35. H.S. Cho. Effect of Cr and Al on Corrosion Behavior and Mechanical Properties of Oxide Dispersion Strengthened Steels, Doctoral thesis

36. A.C.S. Sabioni, A.M. Huntz, F. Silva, F. Jomard, Diffusion of iron in Cr_2O_3: polycrystals and thin films, Mater. Sci. Eng. A392 (2005) 254-261

37. Irvin R. Kramer and Louis J. Demer, Effects of environment on mechanical properties of metals, Progress in Material Science, Vol.9, No 3(1961) 133-199.

Chapter 4

Stress Corrosion Cracking Behavior of Austenitic Stainless Steel and Ferritic/Martensitic Steel in Different Water Chemistry of Supercritical Pressurized Water

4.1 Introduction.

Several works on the SCC susceptibility of austenitic stainless steels and ferritic/martensitic steels were conducted in SCPW dissolved with various oxygen contents from deaerated condition ($\simeq$0.0 ppm) to 8 ppm. Austenitic stainless steels tested in supercritical water are 304, 316, 316L, 347 and UNS S31266 [1-7]. All of these steels have experienced some degree of SCC, most of which is intergranular. Ferritic/martensitic steels of T91, T92, HCM12A, HT-9 and F82H have been tested in SCPW with dissolved oxygen contents ranging from the deaerated condition to 500 ppb by slow strain rate test [7-12]. Of these alloys, only HT-9 showed a susceptibility to SCC that increased with temperature and DO content.

In the case of water chemistry condition for boiled water reactor (BWR), an effective remedy for 304 austenitic stainless steel pipe cracking can be developed based on hydrogen injection to reduce the steel corrosion potential combined with careful control of water quality [13].

Some experimental data for nickel alloy at pressurized water reactor (PWR) condition indicates that primary water stress corrosion cracking (PWSCC) growth rate has a convex upward dependency for DH content [14,15]. On the other hand, it is reported that the experimental data of PWSCC initiation shows a monotonic decrease of initiation time for the increasing DH content [16-18]. SCC growth rate of uni-directionally cold worked 316NG stainless steel in simulated PWR primary water environments decreases with increasing DH in the range of 5–50 cm^3 (STP) H_2/kg H_2O [19].

As for the application of the structural materials to fusion blanket systems, the effect of hydrogen isotopes on SCC will be one of the important issues to be solved. However, all of the tests in SCPW were conducted with oxygen environments but not in SCPW dissolved with hydrogen, as mentioned above. Therefore, the objective of this study is to investigate the effect of supercritical water chemistry against SCC susceptibility of 316L austenitic stainless steel and F82H ferritic/martensitic steel.

4.2 Experimental

4.2.1 Materials and specimen preparation

The materials used were SUS316L austenitic stainless steel and F82H ferritic/martensitic steel. The chemical compositions are shown in Table 4.1. The geometry of tensile specimen has been described in the previous chapter. SUS316L was solid solution heat-treated at 1050 °C for 1 hour, and

then water quenched. In case of F82H, the tensile specimens were cut out from a thick (15 mm) plate which was normalized at 1040 °C for 30 min and tempered at 740 °C for 1 hr followed by air cooling.

Table.4.1. The chemical compositions of tested materials in wt. %

Material	C	Si	Mn	Cr	Ni	P	S	W	V	Ta	N	B	Mo
F82H	0.10	0.2	0.5	8.0	—	—	—	2.0	0.20	0.04	<0.01	0.003	—
SUS316L	0.01	0.73	1.06	17.41	12.13	0.032	0.004	—	—	—	—	—	2.05

4.2.2 SSRT conditions.

To investigate the SCC susceptibility, the SSRTs were carried out in a supercritical pressurized water system at 500 °C under a pressure of 25 MPa, at a higher strain rate of 1×10^{-3} s^{-1} and lower strain rate of 1×10^{-6} s^{-1} or 5×10^{-7} s^{-1}. The contents of DO and DH of SCPW for the test were 0.4 ppm DH, DO and DH < 0.01 ppb (deaerated) and 8 ppm DO, which were controlled by injections of high purity oxygen, nitrogen and hydrogen gas to a conditioning tank.

After the tests, a gauge section and fracture surface of the SSRT specimen was observed with a scanning electron microscope (SEM) to investigate fracture mode to evaluate SCC susceptibility. A cross section of the fractured tensile specimens was analyzed with a SEM and Electron probe micro-analyzer (EPMA). The cracking pass way was examined by the cross-sectional observation to measure the crack depth and to count the number of cracks. Crack development pattern was also investigated by electron backscattered electron diffraction (EBSD).

4.3 Results and discussion.

4.3.1 Stress-strain behavior.

The SSRT results of SUS316L and F82H in a vacuum and SCPW dissolved with different DO and DH are shown in Fig. 4.1 and 4.2. The numerical values of tensile properties obtained by the SSRT are summarized in Table 4.2.

For SUS316L austenitic steel, all of the stress-strain curves exhibit typical work hardening behavior, indicating the high degree of uniform elongation. The elongations of specimens tested in

deaerated SCPW (DO & DH < 0.01 ppb) were reduced by decreasing strain rate, while other specimens tested in SCPW with DH 0.4 ppm, DO 8 ppm and also vacuum show higher elongation at lower strain rate.

In contrast, the stress-strain curves for F82H ferritic / martensitic steel denote that the yield stress and ultimate tensile stress are decreased with decreasing strain rate, while the total elongation tends to increase with decreasing strain rate. This phenomenon can be explained by typical strain rate effect for metallic materials because a decreased strain rate gives more time for dislocations to move past obstacles as a thermally activation process. There is no significant effect of test environment on the stress-strain behavior of the F82H ferritic / martensitic steel at tested strain rates. The obtained SSRT results suggest that there is no susceptibility to SCC of the F82H in the SCPW, although stress strain behavior often gives us no information about SCC susceptibility.
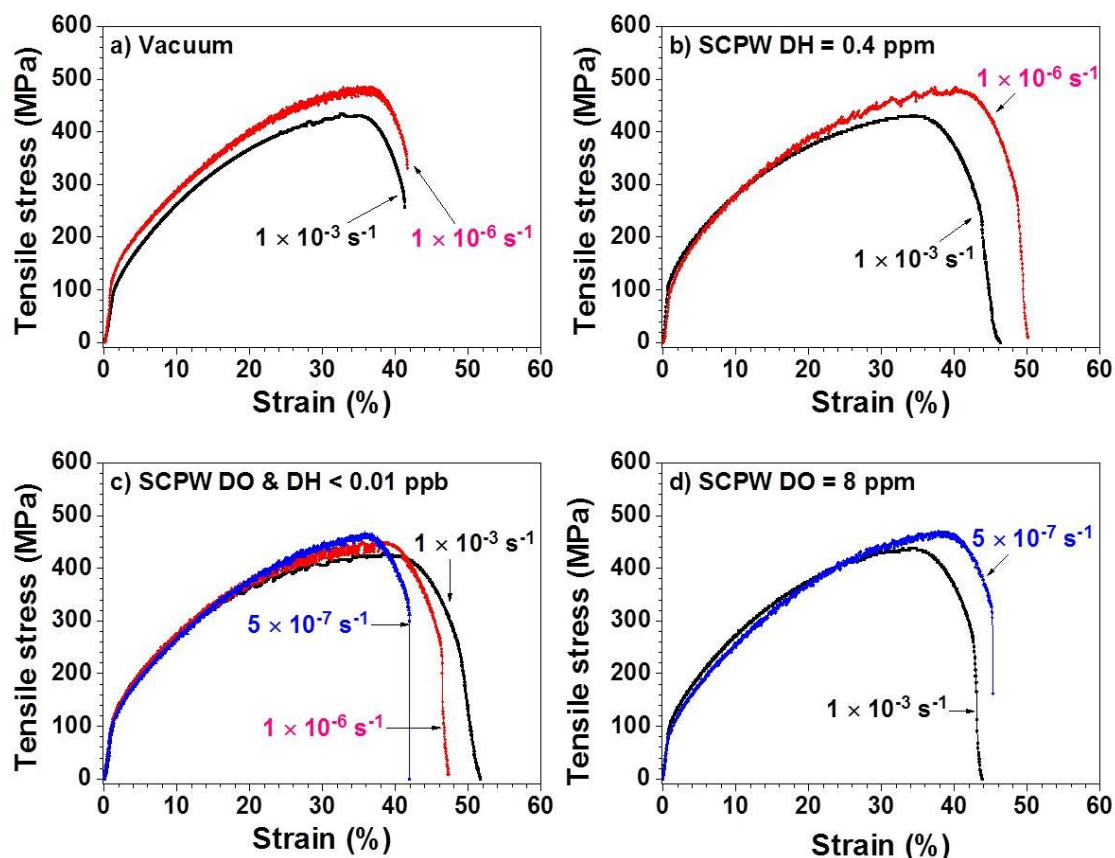

Fig. 4.1 SSRT stress-strain curves for SUS316L austenitic stainless steel as a function of different strain rate at each environment of a) vacuum, b) SCPW DH =0.4 ppm, c) SCPW DO & DH < 0.01 ppb (deaerated) and d) SCPW DO = 8 ppm
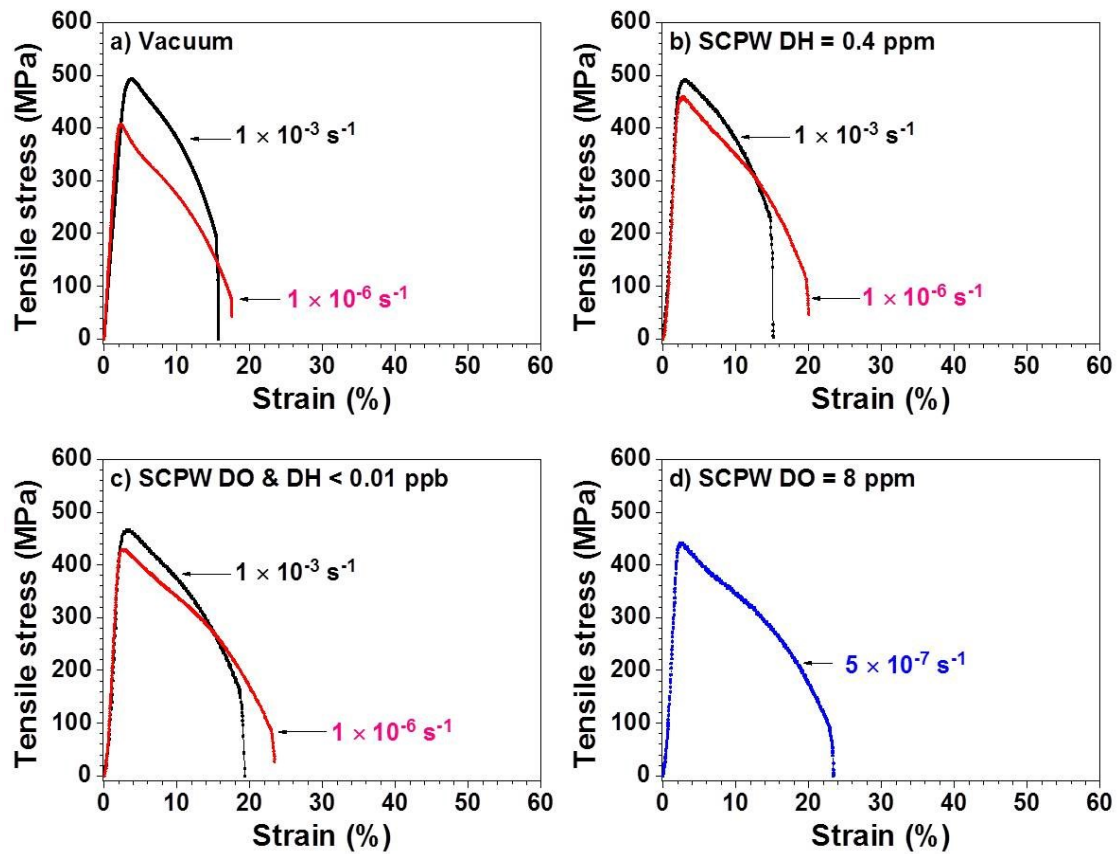
Fig. 4.2 SSRT stress-strain curves for F82H ferritic/martensitic steel as a function of different strain rate at each environment of a) vacuum, b) SCPW DH =0.4 ppm, c) SCPW DO & DH < 0.01 ppb (deaerated) and d) SCPW DO = 8 ppm

Table 4.2. SSRT data for ODS ferritic steel in vacuum and SCPW

Material	Environments	Strain rate	Yield stress (MPa)	Ultimate tensile stress (MPa)	Total elongation (%)	Reduction in area (%)
SUS316L	Vacuum	1×10^{-3} s^{-1}	108	435	41.3	73.6
		1×10^{-6} s^{-1}	122	486	41.6	70.3
	SCPW DH = 0.4 ppm	1×10^{-3} s^{-1}	116	431	46.3	82.8
		1×10^{-6} s^{-1}	108	485	50.1	74.4
	SCPW DO&DH < 0.01 ppm	1×10^{-3} s^{-1}	125	428	51.6	89.4
		1×10^{-6} s^{-1}	101	448	47.3	66.8
		5×10^{-7} s^{-1}	113	466	41.9	59.2
	SCPW DO = 8.0 ppb	1×10^{-3} s^{-1}	109	438	43.7	78.3
		5×10^{-7} s^{-1}	104	470	48.6	78.3
F82H	Vacuum	1×10^{-3} s^{-1}	466	492	15.7	85.7
		1×10^{-6} s^{-1}	400	407	17.6	93.4
	SCPW DH = 0.4 ppm	1×10^{-3} s^{-1}	467	491	15.2	76.4
		1×10^{-6} s^{-1}	444	489	20	90.6
	SCPW DO&DH < 0.01 ppb	1×10^{-3} s^{-1}	449	466	19.3	84.1
		1×10^{-6} s^{-1}	418	429	23.4	93.6
	SCPW DO = 8.0 ppm	5×10^{-7} s^{-1}	438	441	23.4	91.8

4.3.2 Fracture behavior

4.3.2.1 Fracture surface analysis.

Fig. 4.3 shows the dependence of reduction in area of fractured surface after SSRT on strain rate. In the case of SUS316L austenitic stainless steel, the reduction in area of the specimens tested in SCPW with any water chemistry decreased with decreasing strain rate, while relatively constant values of reduction in area were obtained for the specimens tested in vacuum regardless of strain rate changes. It should be noticed that a significant decreasing of reduction in area occurred in SCPW with DO & DH < 0.01 ppb at lower strain of 1×10^{-6} s^{-1} and 5×10^{-7} s^{-1}. A direct link between total elongation and reduction in area of SUS316L was not observed.

In contrast to this, the reduction in area of F82H ferritic / martensitic steels increased with decreasing strain rate, not only in non-corrosive environment of vacuum but also in corrosive environments of SCPW.

All fracture surfaces of SUS316L and F82H after SSRT at higher strain rate of 1×10^{-3} s^{-1} exhibit ductile fracture surface with dimples at any tested environment, as shown in Fig 4.4 and 4.5. After SSRT at lower strain rate of 1×10^{-6} s^{-1} or 5×10^{-7} s^{-1}, brittle fracture surface was observed on SUS316L tested in SCPW (Fig 4.6 - b, c, d, e) while no brittle surface was shown in vacuum (Fig 4.6 – a). Appearance of brittle fracture surface and decreasing of reduction in area imply that fracture mode of SUS316L was changed in SCPW by decreasing strain rate. In contrast, only ductile fracture surface was found on F82H tested at lower strain rate, regardless of test environments, as shown in Fig 4.7.
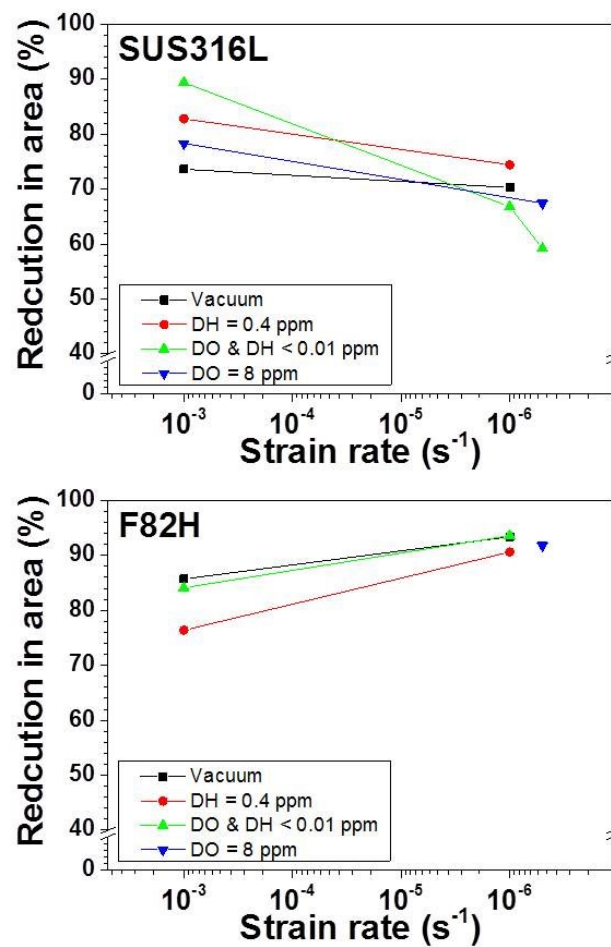

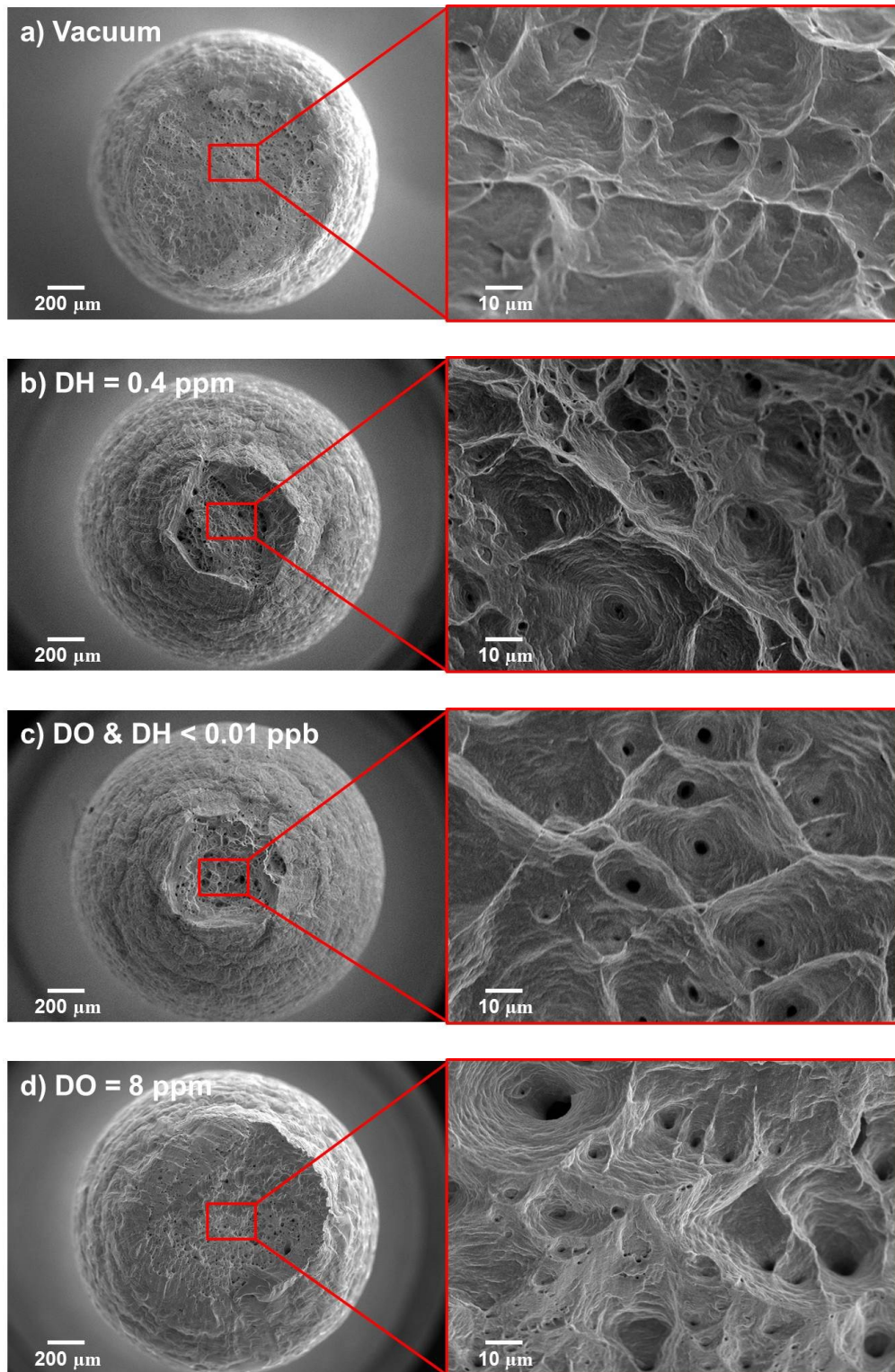Fig 4.3. Reduction in area of SUS316L and F82H after fracture by SSRT.

Fig. 4.4 Fracture surface of SUS316L austenitic stainless steel after SSRT at higher strain rate of 1×10^{-3} s^{-1} in a) vacuum, b) SCPW with DH 0.4 ppm, c) deaerated SCPW (DO & DH < 0.01 ppb) and d) SCPW with DO 8 ppm.
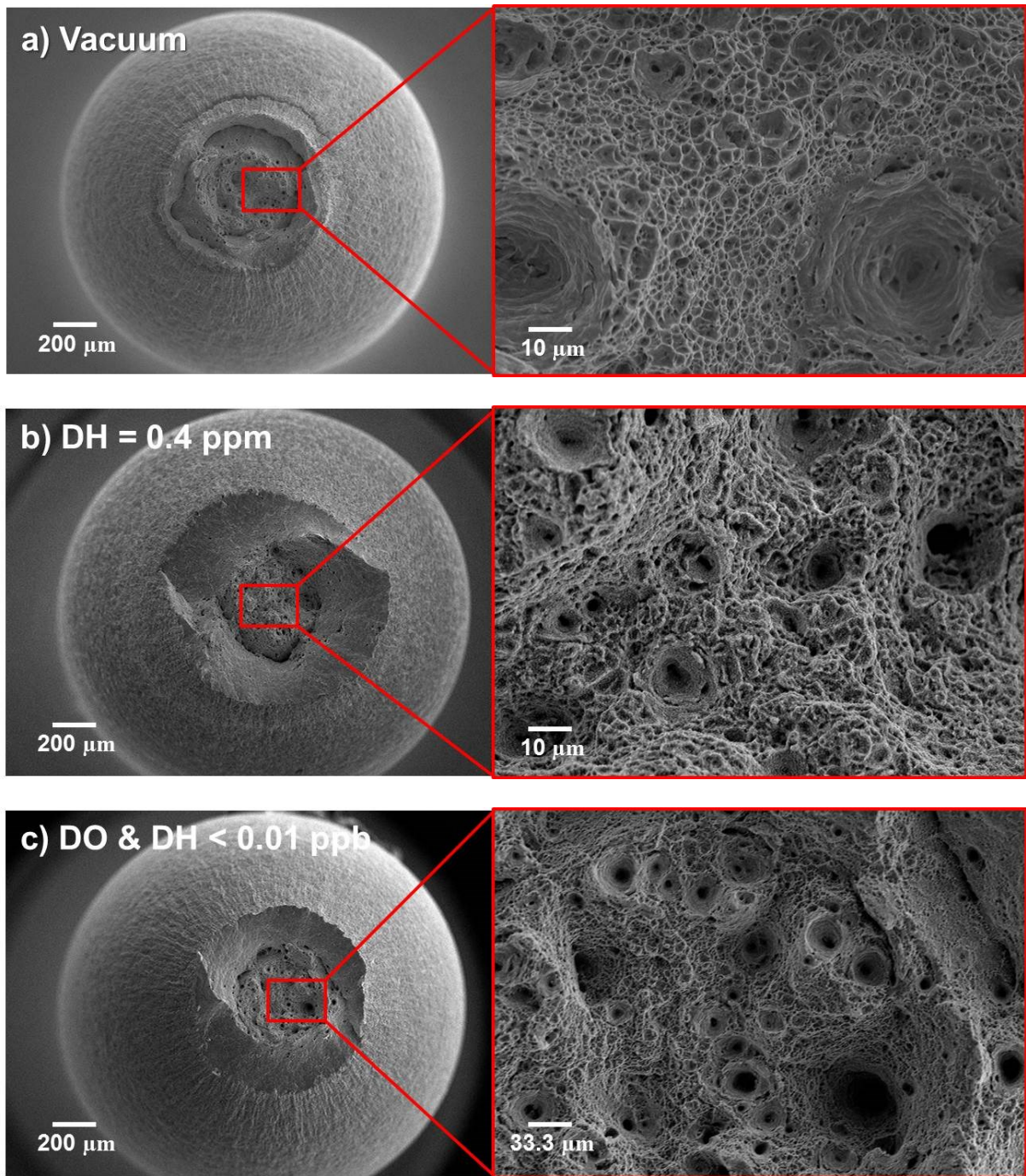
Fig. 4.5 Fracture surface of F82H ferritic / martensitic steel after SSRT at higher strain rate of 1×10^{-3} s^{-1} in a) vacuum, b) SCPW with DH 0.4 ppm and c) deaerated SCPW (DO & DH < 0.01 ppb)
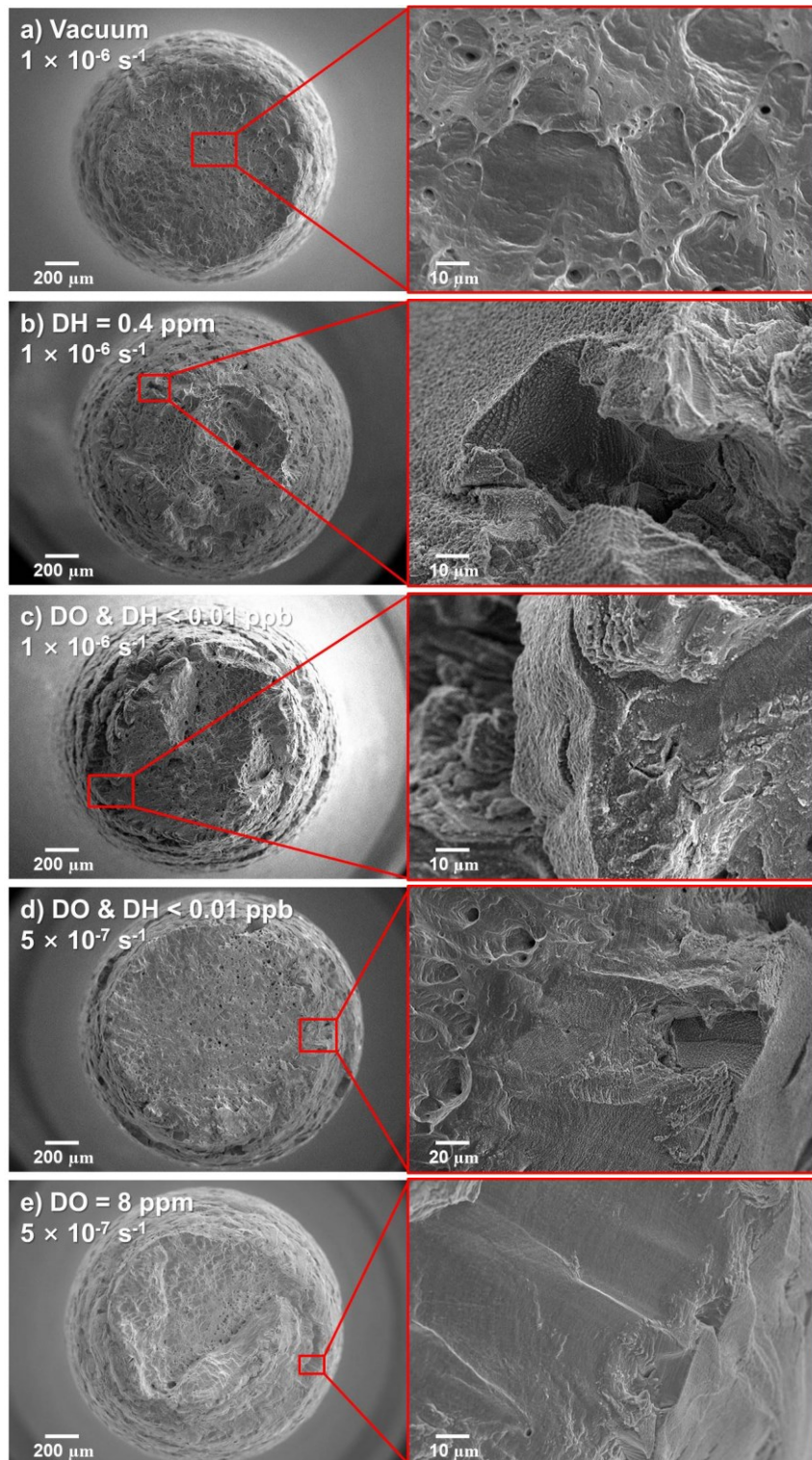
Fig. 4.6 Fracture surface of SUS316L austenitic stainless steel after SSRT at lower strain rate of 1×10^{-6} s^{-1} or 5×10^{-7} s^{-1} in (a) vacuum, (b) SCPW with DH 0.4 ppm, (c, d) deaerated SCPW (DO & DH < 0.01 ppb) and (e) SCPW with DO 8 ppm.
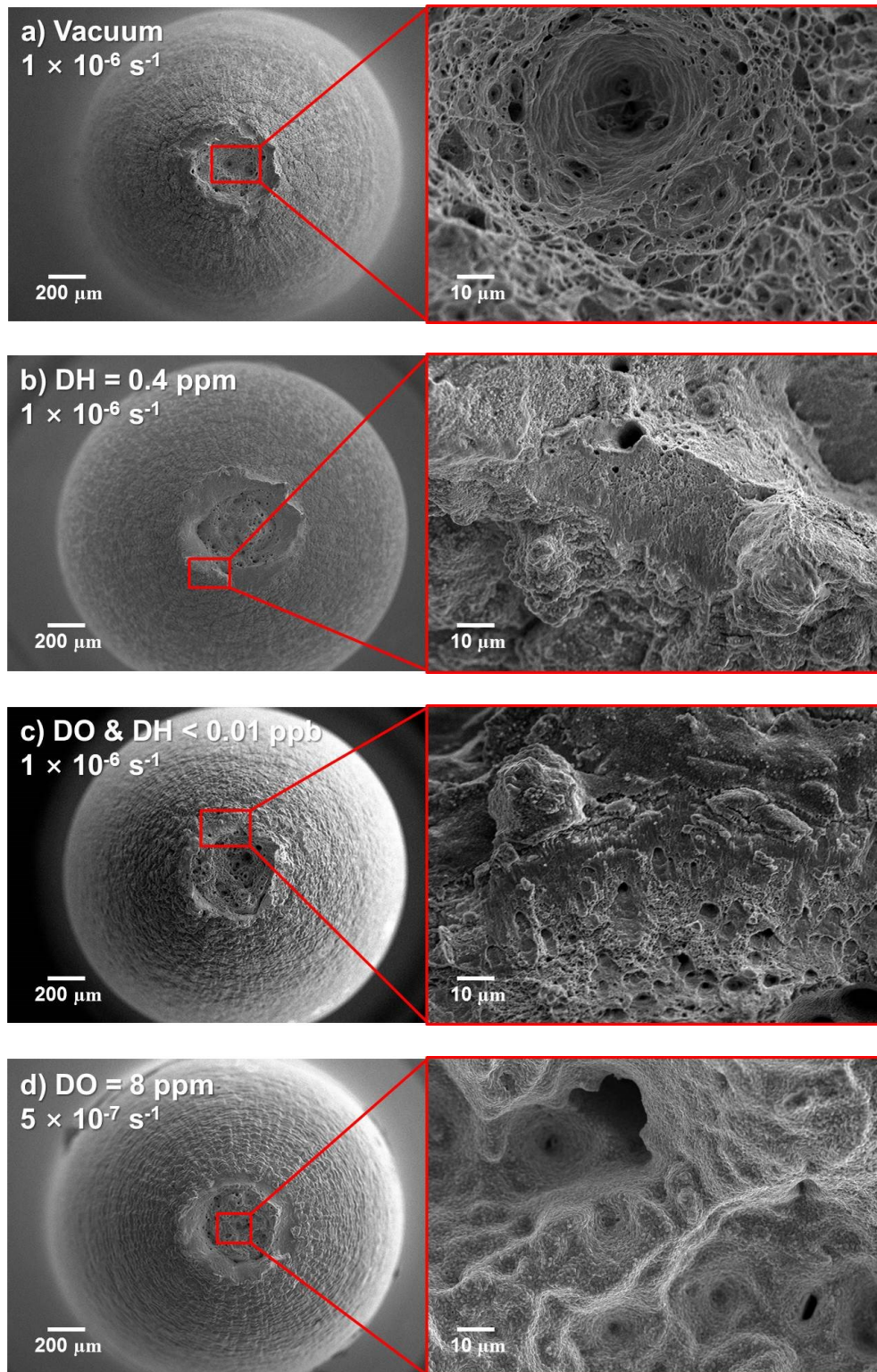
Fig. 4.7 Fracture surface of SUS316L austenitic stainless steel after SSRT at lower strain rate of 1×10^{-6} s^{-1} or 5×10^{-7} s^{-1} in a) vacuum, b) SCPW with DH 0.4 ppm, c) deaerated SCPW (DO & DH < 0.01 ppb) and d) SCPW with DO 8 ppm.

4.3.2.2 Specimen side surface analysis.

Fig 4.8 and 4.9 indicate that cup and corn facture shape with necking was observed for all the tested materials at higher strain rate of 1×10^{-3} s^{-1} not only in vacuum but also in a SCPW. However, at lower strain rate of 1×10^{-6} s^{-1} or 5×10^{-7} s^{-1}, cracks were observed on the specimen surface of both of SUS316L and F82H except for SUS316L tested in vacuum as shown in Fig 4.10 and 4.11. The observed cracks, however, have a significant difference in the distribution and shape between SUS316L and F82H. Cracks on SUS316L were widely distributed over the whole gauge section and were mostly formed perpendicularly to the tensile direction. Because the surfaces of SUS316L specimens tested at lower strain rates were covered by corrosion products, it should be confirmed that the cracks contribute to development into matrix. In contrast, cracks on F82H were located at only near the neck part with different crack pattern, as shown in Fig 4.11. The crack patterns at lower strain rate were changed from perpendicular to random, as deformation is more progressing. This evidence suggests that the surface cracks are only corrosion products on the F82H specimen and no crack propagates into the substrate matrix of F82H.
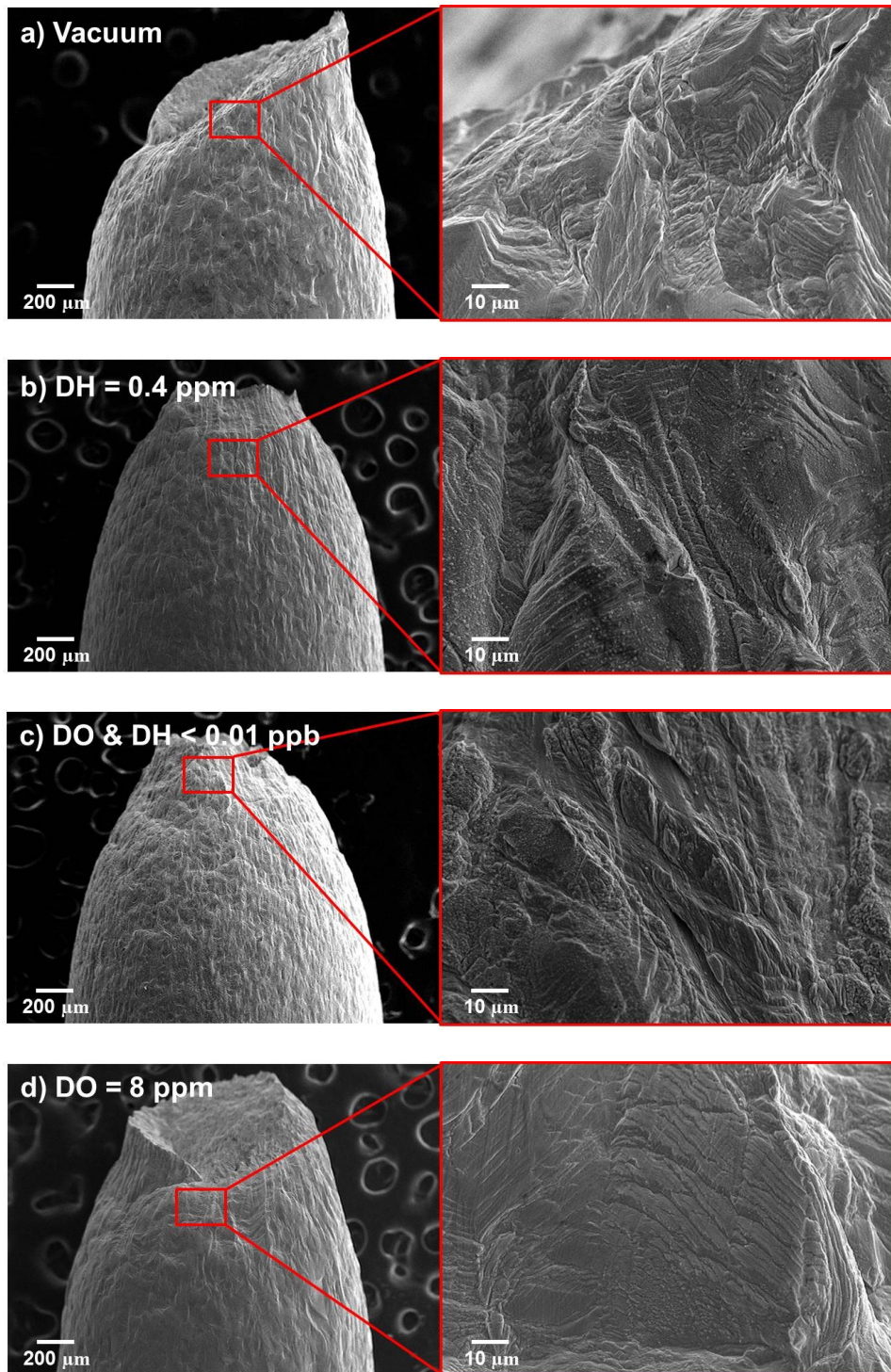
Fig. 4.8 Specimen side surface of SUS316L austenitic stainless steel after SSRT at higher strain rate of 1×10^{-3} s^{-1} in a) vacuum, b) SCPW with DH 0.4 ppm, c) deaerated SCPW (DO & DH < 0.01 ppb) and d) SCPW with DO 8 ppm.
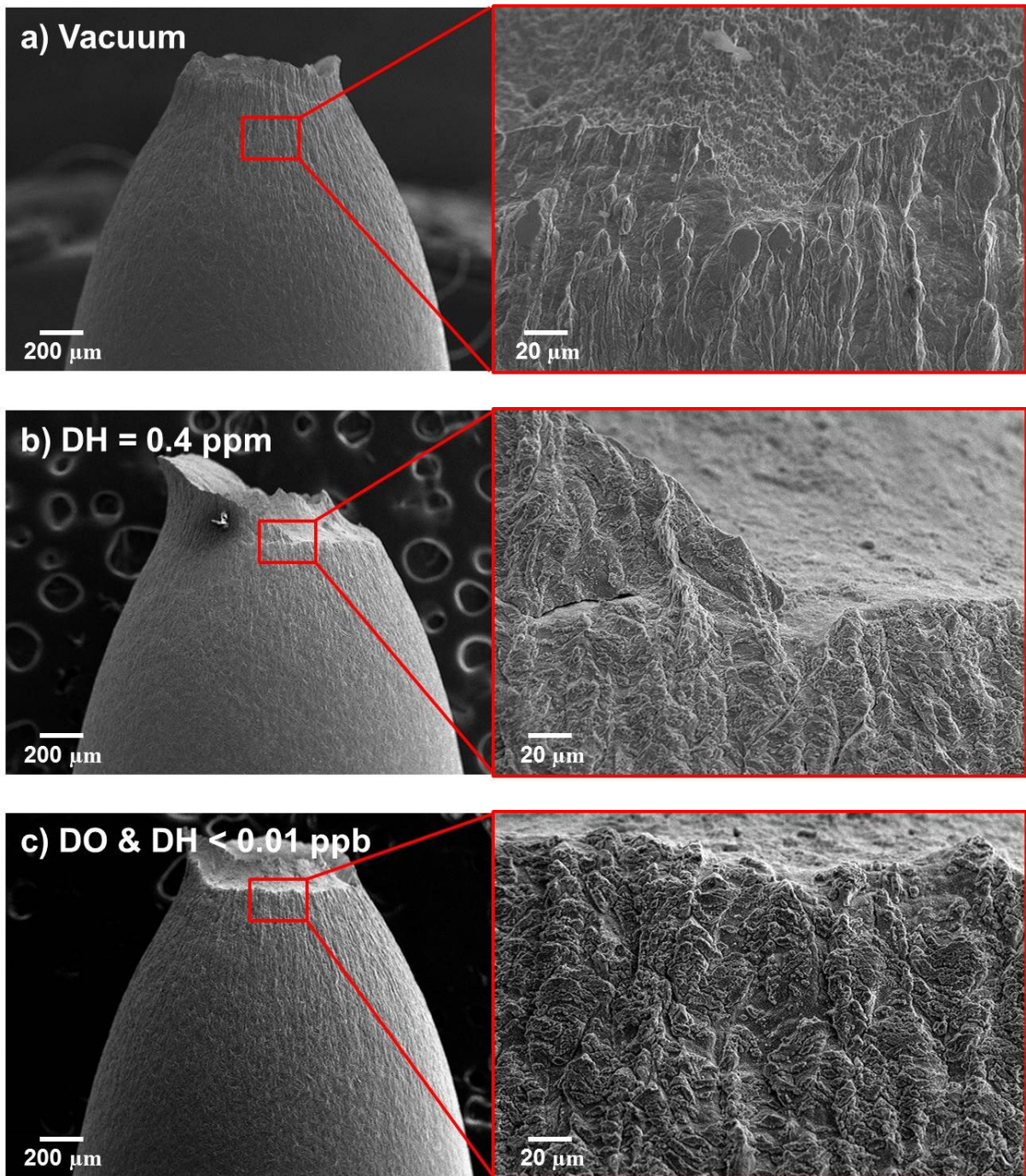
Fig. 4.9 Specimen side surface of F82H ferritic / martensitic steel after SSRT at higher strain rate of 1 $\times$ 10^{-3} s^{-1} in a) vacuum, b) SCPW with DH 0.4 ppm and c) deaerated SCPW (DO & DH < 0.01 ppb)
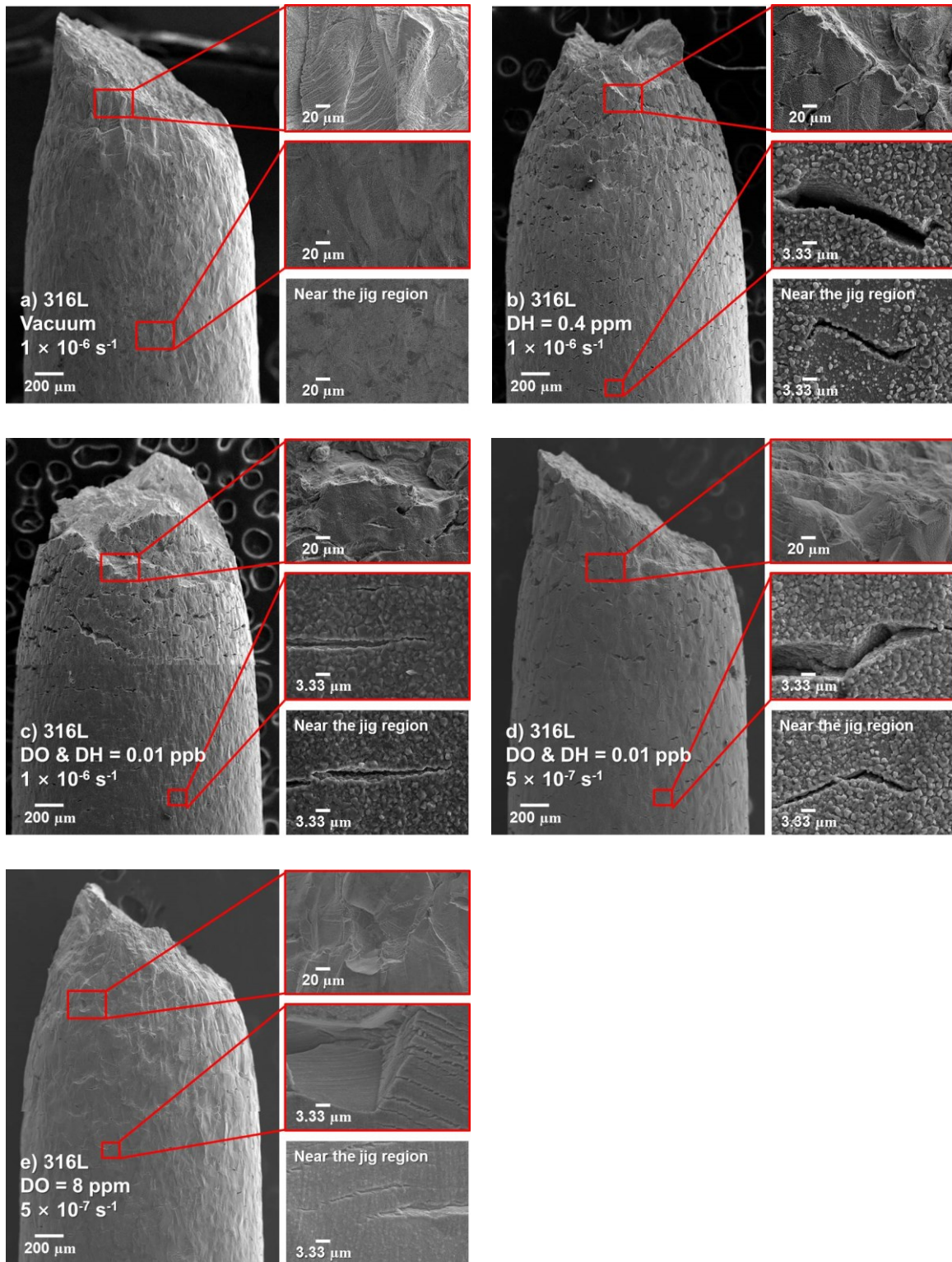
Fig. 4.10 Specimen side surface of SUS316L austenitic stainless steel after SSRT at lower strain rate of 1×10^{-6} s^{-1} or 5×10^{-7} s^{-1} in (a) vacuum, (b) SCPW with DH 0.4 ppm, (c, d) deaerated SCPW (DO & DH < 0.01 ppb) and (e) SCPW with DO 8 ppm.

Fig. 4.11 Specimen side surface of F82H ferritic / martensitic steel after SSRT at lower strain rate of 1 × 10^{-6} s^{-1} or 5 × 10^{-7} s^{-1} in a) vacuum, b) SCPW with DH 0.4 ppm, c) deaerated SCPW (DO & DH < 0.01 ppb) and d) SCPW with DO 8 ppm.
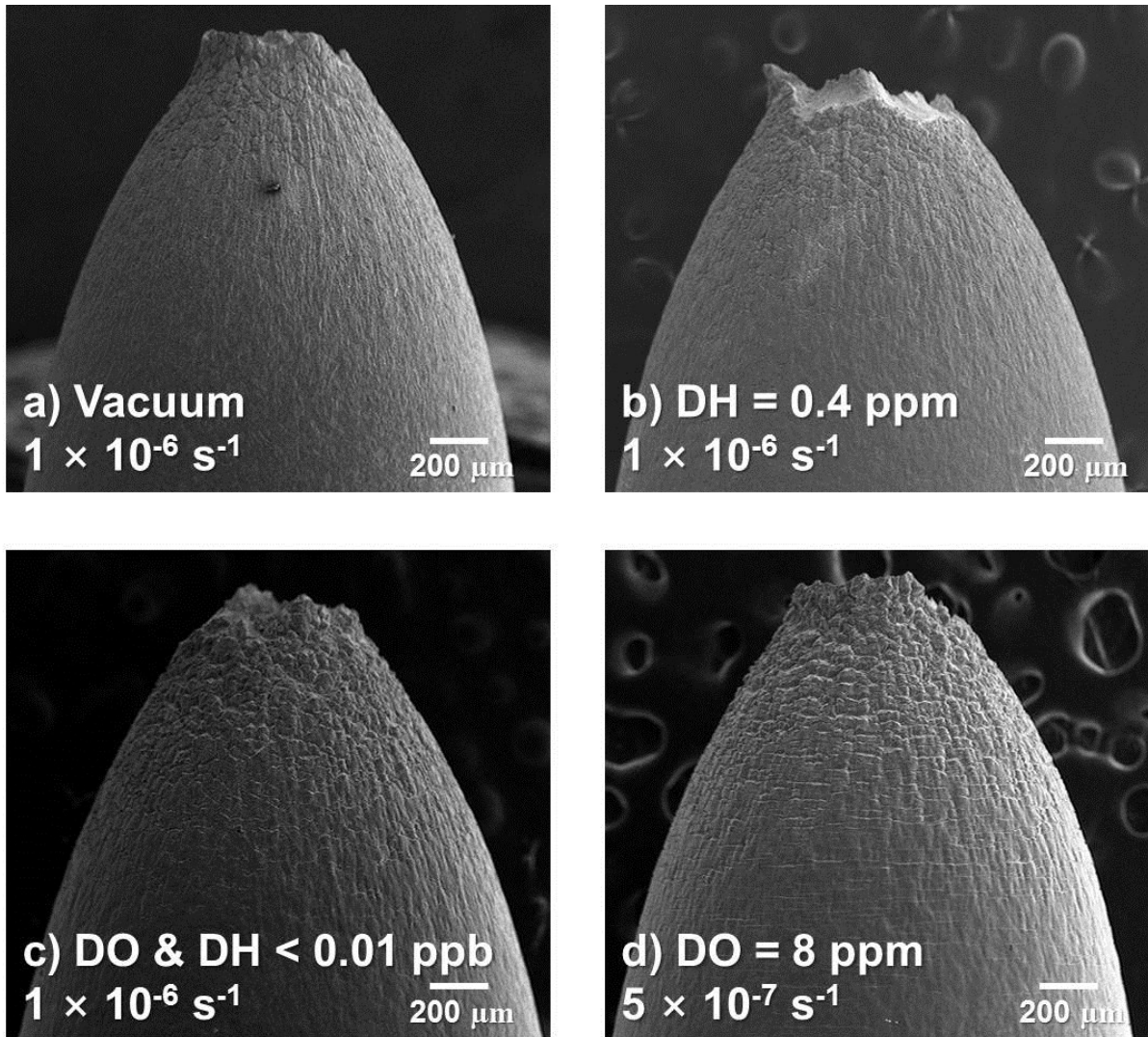
4.3.2.3 Cross sectional analysis

To make clear the role of corrosion products in the nucleation of cracks which were observed near the fracture surface, EPMA analysis was conducted for the cross-sectional areas of the tensile specimens after SSRT in SCPW at lower strain rate.

EPMA analysis results of cracks on SUS316L after SSRT at lower strain rate of 1×10^{-6} s^{-1} or 5×10^{-7} s^{-1} in SCPW was shown in Fig 4.12. All the corrosion products were Fe/Cr oxide layers, even in the dissolved hydrogen environment, and they are classified into two layers, an outer Fe-rich oxide layer and an inner Cr-rich oxide layer, which agreed well with previous studies on oxide films formed on SUS316 and SUS316L in SCW [20,21]. Kim found that the oxide film formed on type 304 austenitic stainless steel in 288 °C water containing 200 ppb O_2 and 150 ppb H_2 mainly consisted of two oxide layers: an inner layer of iron chromate ($FeCr_2O_4$) structure with an outer layer of hematite (α-Fe_2O_3) and magnetite (Fe_3O_4), respectively [22]. Terachi et al. reported that the oxide film formed on 316 stainless steel after exposure to a simulated PWR primary water at 320 °C had a double-layer structure: the outer layer was composed mainly of iron oxide (Fe_3O_4) and relatively chromium-rich oxide was recognized in the inner layer ($FeCr_2O_4$) [23]. In addition, Ni enrichment was observed at the interface between the metal matrix and inner layer. These results imply that the general oxidation mechanism of SUS316L in SCW is similar to that in high-temperature water. Much thinner oxide layers were observed on the secondary crack tip than the primary cracks of specimen surface, indicating that stress corrosion cracking was actually occurred. However, clear evidence of grain boundary oxidation was not observed ahead of the crack tip.

EPMA analysis of F82H revealed that the corrosion layer consisted of outer Fe-rich oxide layer and an inner Cr-rich oxide layer, as shown in Fig 4.13. T.R. Allen and G.S. Was reported that ferritic/martensitic steels exhibit two oxide layer when exposed to SCPW with an outer layer containing only magnetite (Fe_3O_4) and an inner layer containing a mixture of (Fe, Cr)$_3$O$_4$ spinel structure [7,9-11,24]. The thickness of oxide layer between crack tip and specimen surface was similar, which suggests that the cracks are oxide layer rupture but not SCC.

The number and depth of SUS316L cracks were measured according to the distance from fractured surface to 2.5 mm away from the rupture region after SSRT deformed at lower strain rate of 1×10^{-6} s^{-1} or 5×10^{-7} s^{-1} in SCPW, and shown in Fig. 4.14. A crack with the penetration depth of 67 μm was measured in the specimen tested in deaerated SCPW at the strain rate of 1×10^{-6} s^{-1} (Fig 4.14-b). The largest number of cracks was existed on the specimen tested in SCPW with 0.4 ppm DH

environment (Fig 4.14-a). However, the number and depth of cracks do not show a clear trend to SCC susceptibility.

The fracture mode of crack was investigated by EBSD for the cracks on SUS316L after SSRT at lower strain rate of 1×10^{-6} s^{-1} or 5×10^{-7} s^{-1} in SCPW with different water chemistry, as shown in Fig. 4.15 – 4.18. Intergranular SCC mainly occurred in SUS316L in the SCPW with dissolved hydrogen environment. On the other hand, the fracture mode at crack initiation stage in SCPW with dissolved oxygen contents was intermixed with intergranular and transgranular SCC.
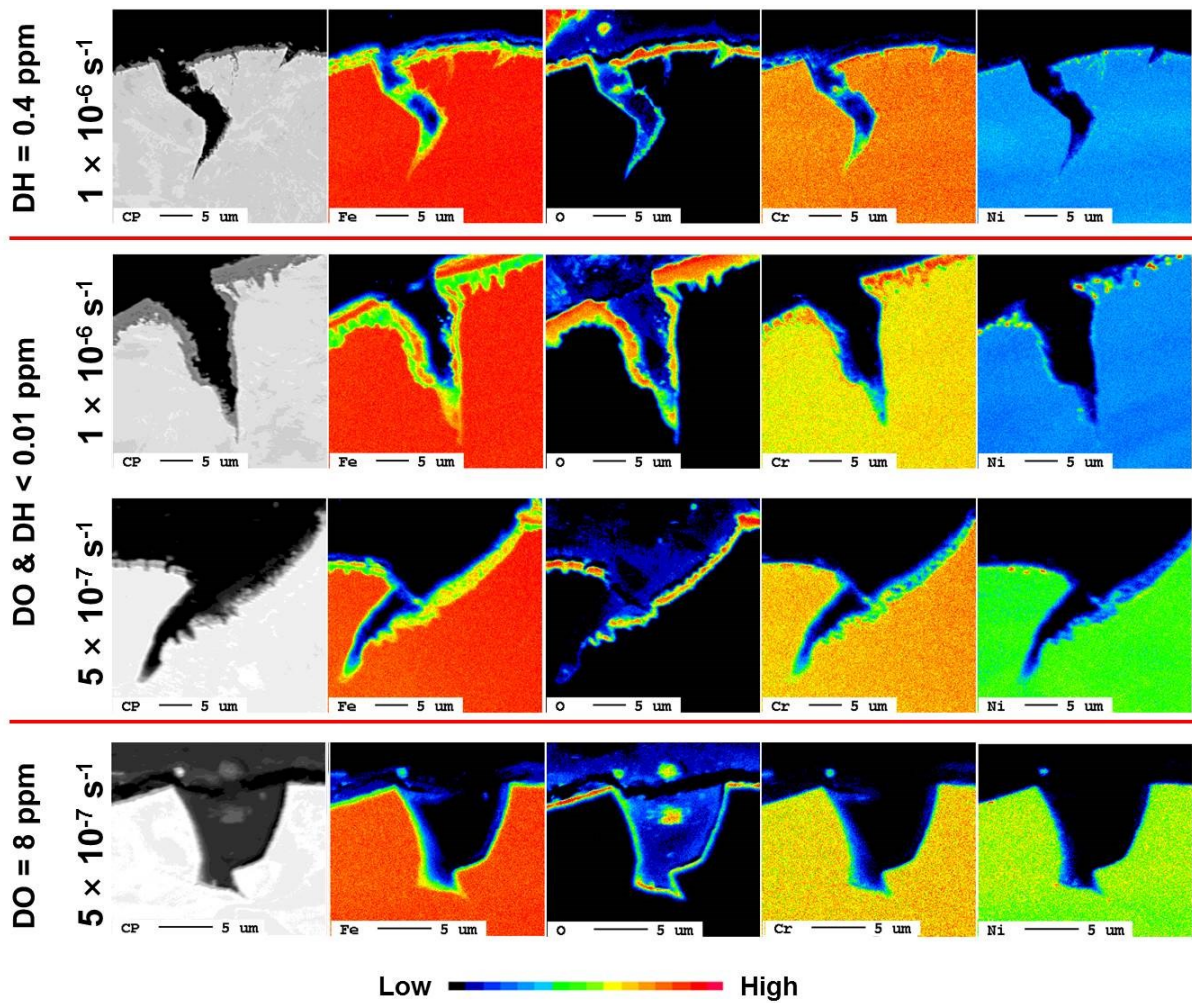
Fig. 4.12 EPMA analysis results of cracks on SUS316L after SSRT at lower strain rate of 1×10^{-6} s^{-1} or 5×10^{-7} s^{-1} in SCPW
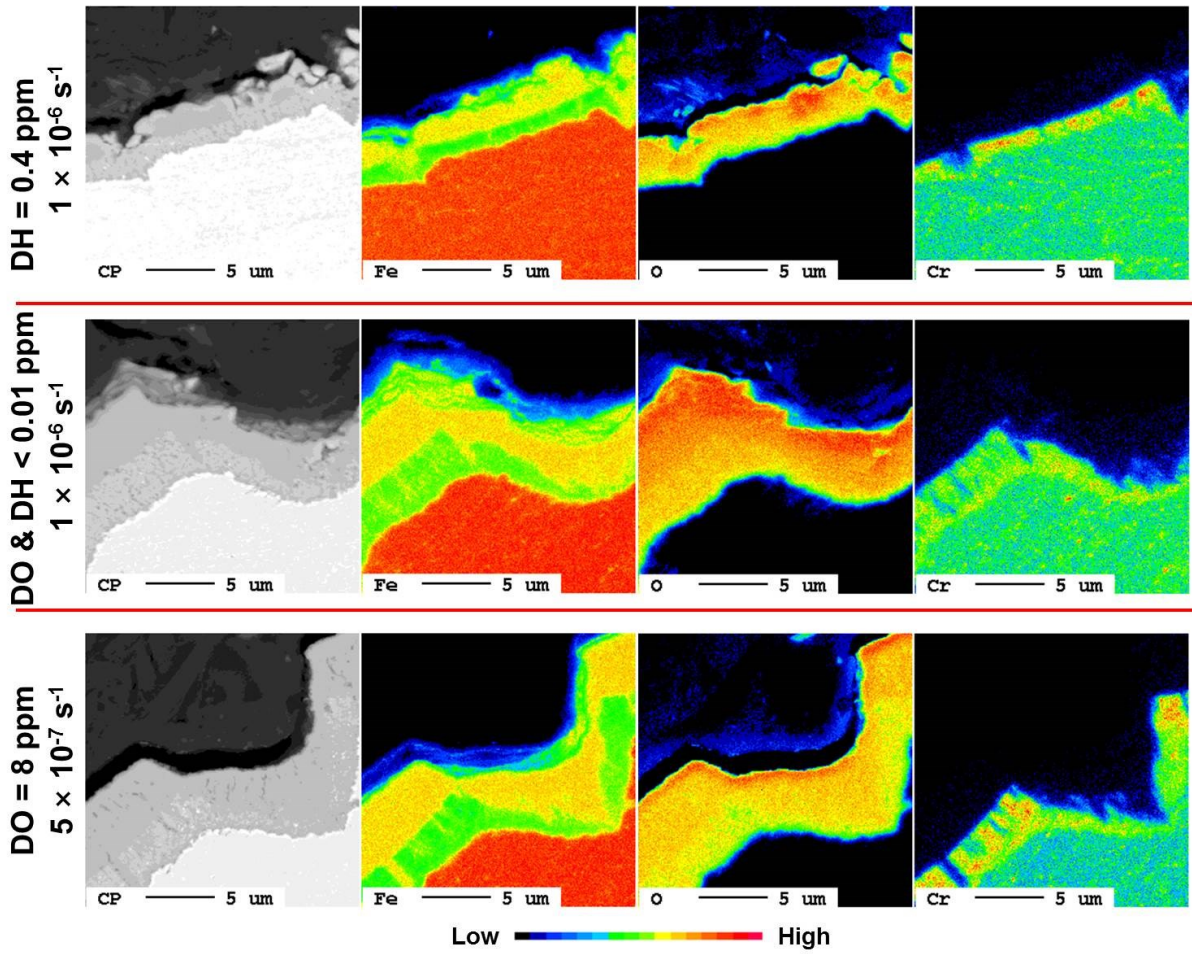
Fig. 4.13 EPMA analysis results of cracks on F82H after SSRT at lower strain rate of 1×10^{-6} s^{-1} or 5×10^{-7} s^{-1} in SCPW
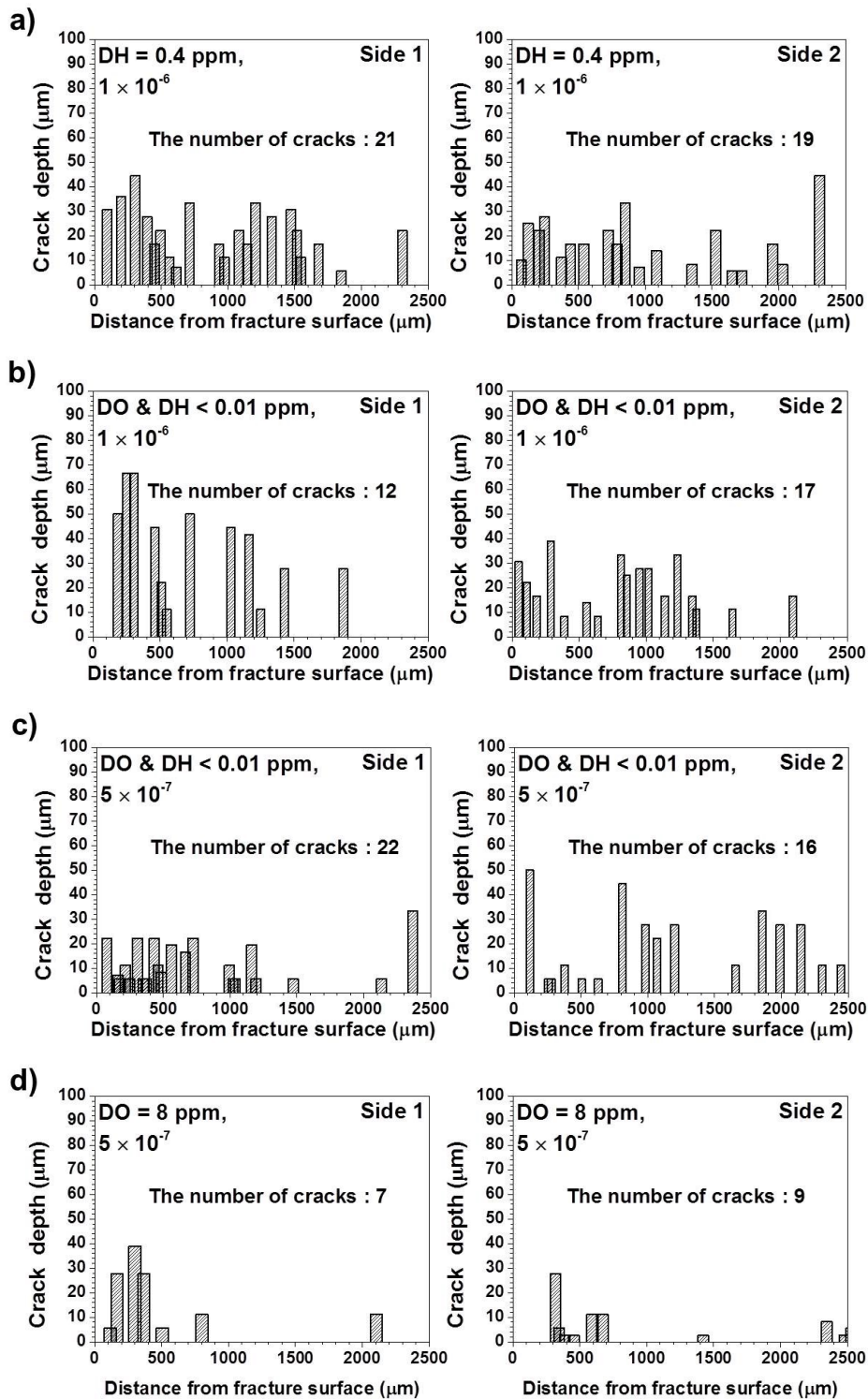
Fig. 4.14 The number and depth of SUS316L cracks according to the distance from fractured surface to the region 2.5 mm away from the fracture after SSRT deformed at lower strain rate of 1×10^{-6} s^{-1} or 5×10^{-7} s^{-1} in SCPW with a) DH 0.4 ppm, b & c) deaerated and d) DO 8 ppm. Side 1 and 2 are the bottom and top side of the cross sectional area of the specimens (refer to Fig. 4.15 – 4.18)
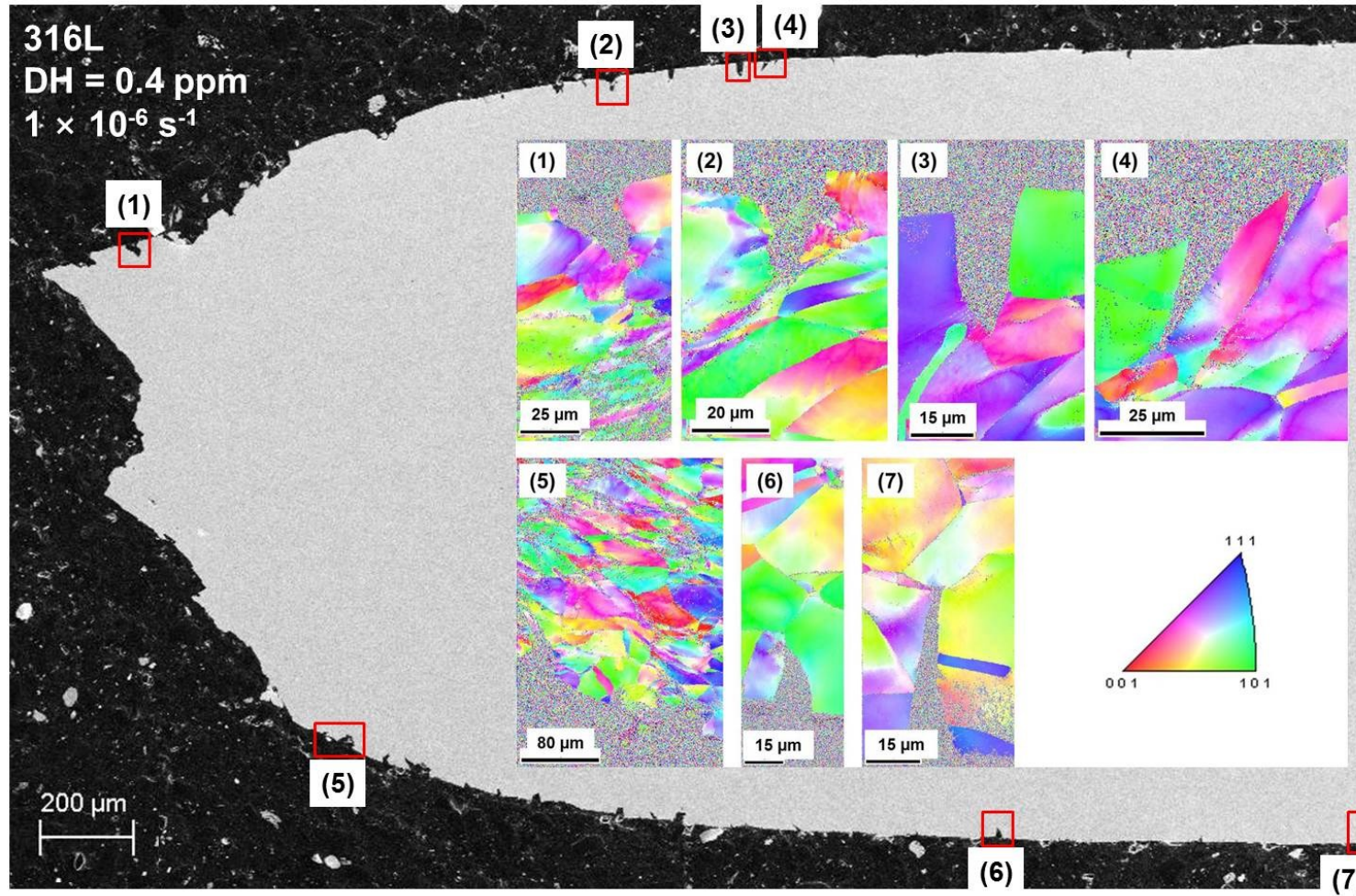
Fig. 4.15 EBSD analysis results of cracks on SUS316L after SSRT at lower strain rate of 1×10^{-6} s^{-1} in SCPW with 0.4 ppm dissolved hydrogen.

Fig. 4.16 EBSD analysis results of cracks on SUS316L after SSRT at lower strain rate of 1×10^{-6} s^{-1} in deaerated SCPW (DO & DH < 0.01 ppm)

Fig. 4.17 EBSD analysis results of cracks on SUS316L after SSRT at lower strain rate of 5×10^{-7} s^{-1} in deaerated SCPW (DO & DH < 0.01 ppm)
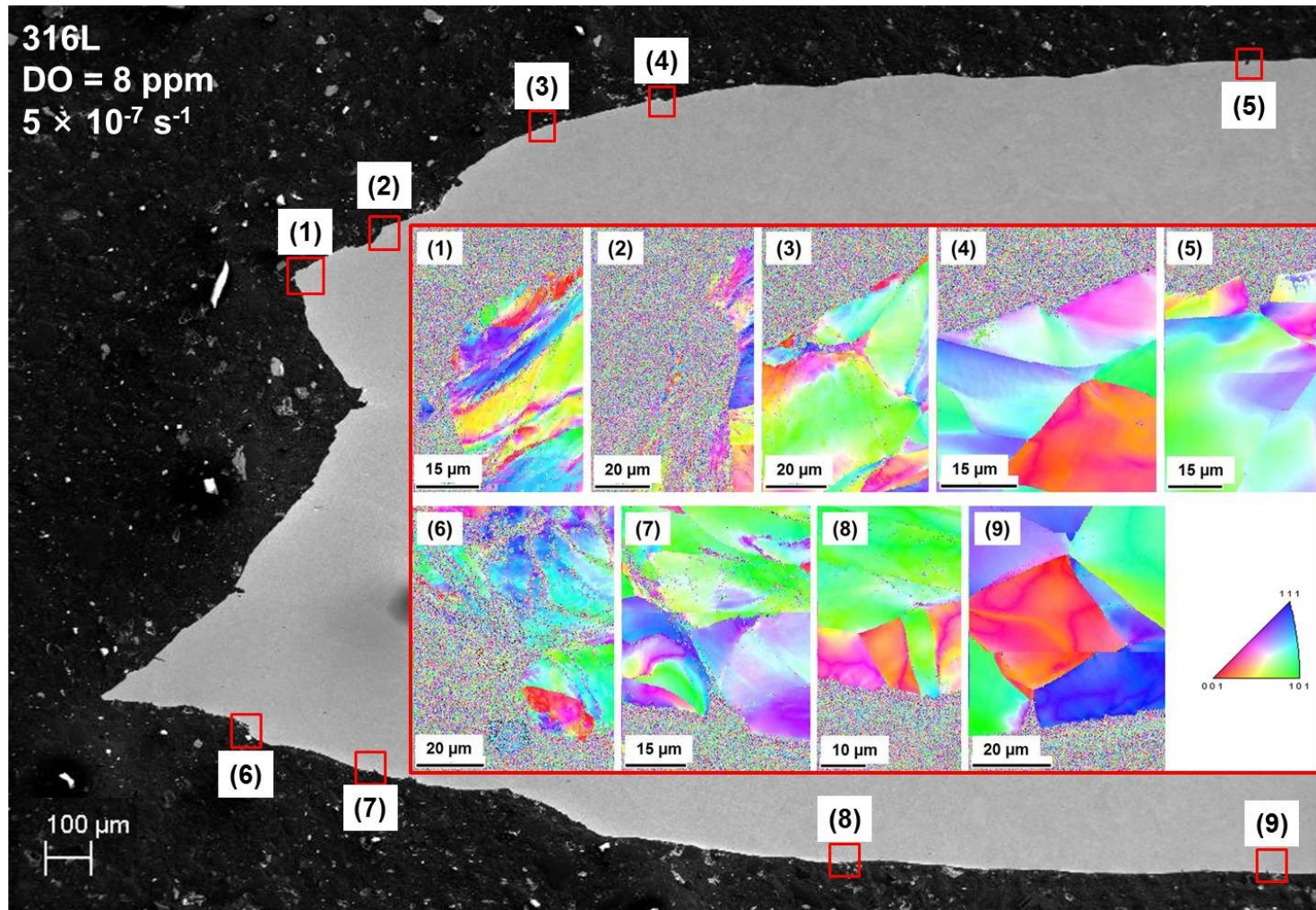
Fig. 4.18 EBSD analysis results of cracks on SUS316L after SSRT at lower strain rate of 5×10^{-7} s^{-1} in SCPW with 8 ppm dissolved oxygen.

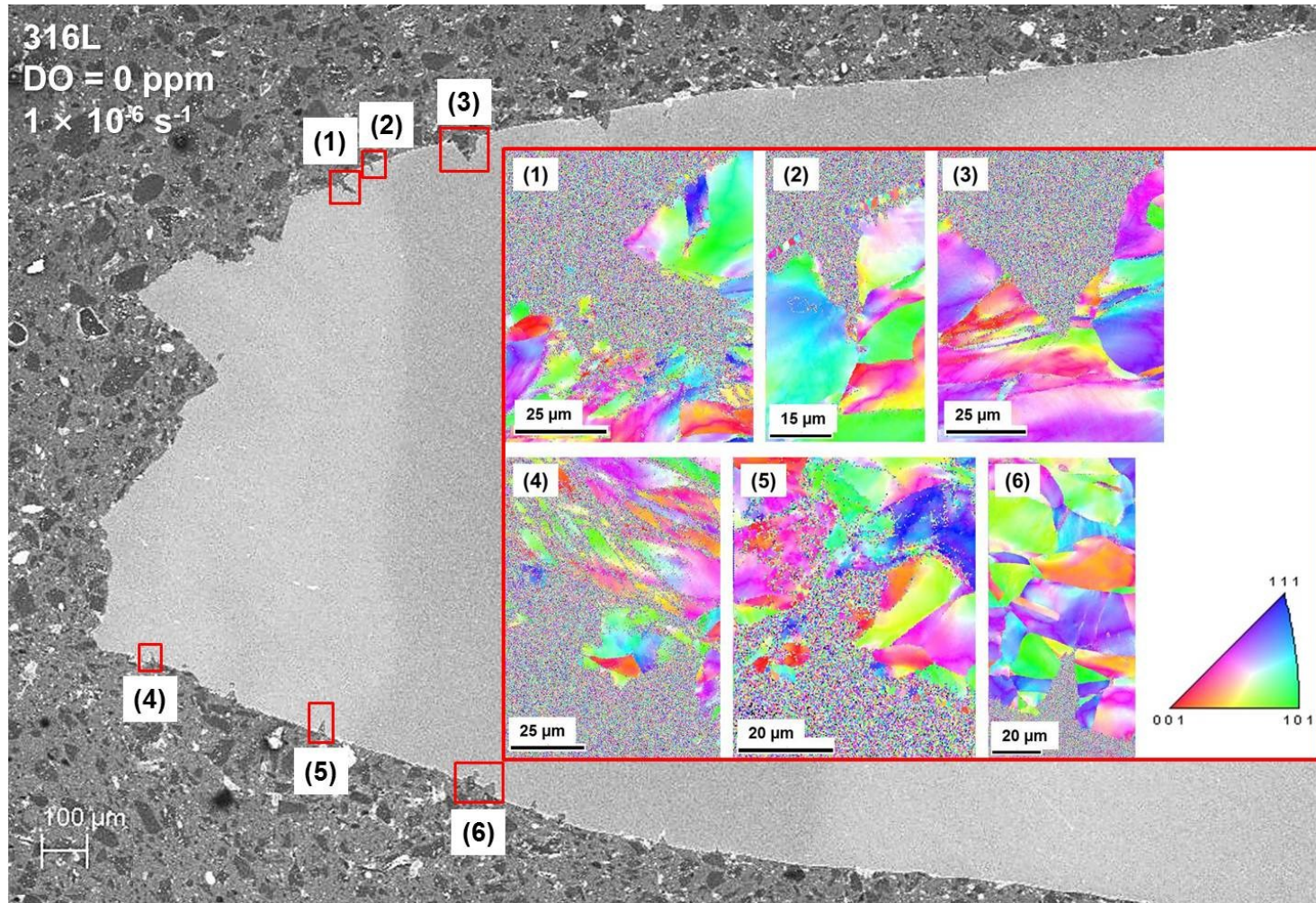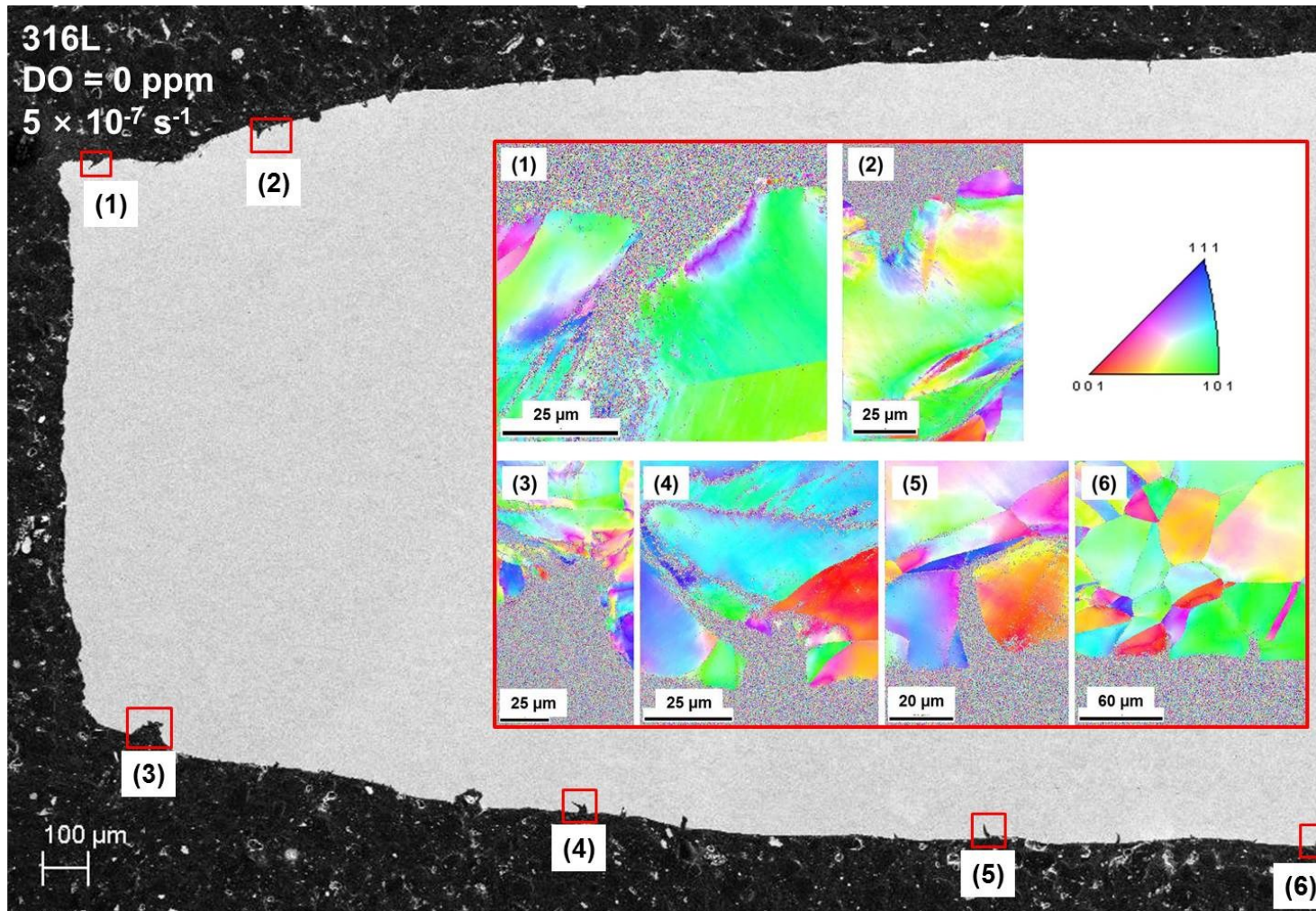**4.3.2.4 SCC susceptibility dependence on material**

As shown in the above sections, the susceptibility to SCC depended on the material among three candidates, F82H, SUS316L and ODS steel. In this section, the material dependence of the SCC susceptibility is discussed based on the results obtained in this study and the previous studies reported by the other researchers.

Many models have been proposed to explain the mechanisms of SCC, but each of these models has its own limitations because of the complexity in the mechanism that is strongly affected by the experimental conditions such as water chemistry, test temperature and specimen surface conditions. Since no single mechanism of SCC can be applied to all cases of SCC, a few models are summarized as follows:

SCC mechanisms can be classified into two cases. One case is a crack advance due to the removal of metal substrate by dissolution or oxidation. This process requires slip-dissolution or grain boundary localized corrosion. According to slip-dissolution model, crack growth is accompanied by extremely localized anodic dissolution with a cyclic process of film rupturing, dissolution and film repairing (Fig. 4.19). The stress assisted intergranular corrosion model applies to the IGSCC in certain aqueous environments in the form of intergranular corrosion, as depicted in Fig. 4.20.
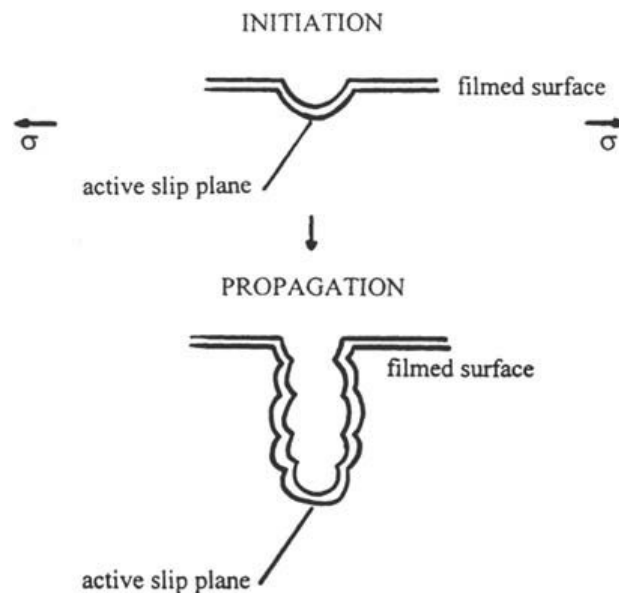
Fig. 4.19 Schematic drawing of crack initiation and growth by slip-dissolution. [25]
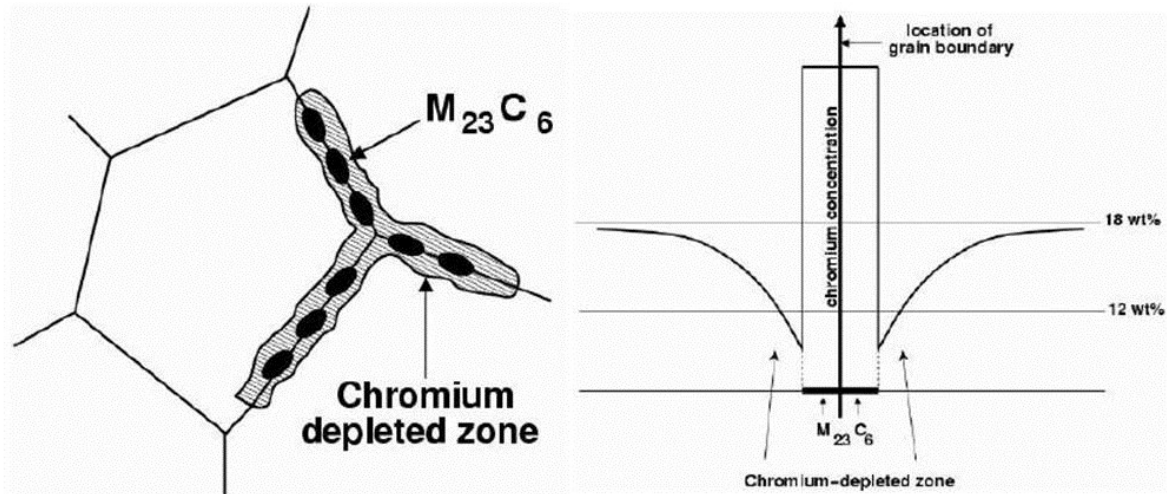
Fig.4.20 Schematic illustration of grain boundary chromium carbides precipitation and corresponding Cr profile. Chromium-depleted zones adjacent to grain boundaries are susceptible to intergranular corrosion [26]

The other case is a crack advance by micro-cracking which may be due to; 1) Hydrogen embrittlement, 2) Cleavage induced by the rupture of a nanoporous surface layer, and 3) Change of surface energy due to adsorption. The representative model of this case, film-induced cleavage model, is originated with the suggestion by Edeleanu and Forty [27] and illustrated in Fig.4.21. They believed that the material through which this crack was propagating (between slip bands) was embrittled by short-range ordering [28]. From this model, sometimes the evidence for stepwise (discontinuous) crack advance was shown in the fracture surfaces, especially in TGSCC [29–33] (Fig. 4.22).
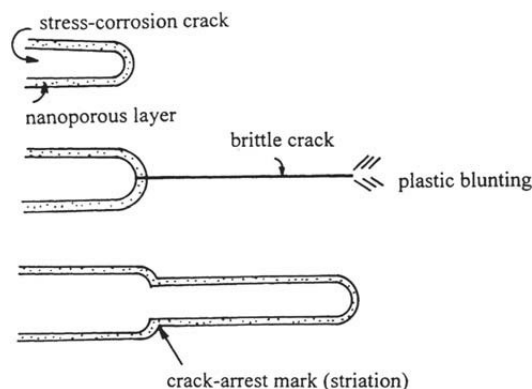
Fig. 4.21 Schematic drawing of crack growth by film-induced cleavage in an fcc metal or alloy. [34]
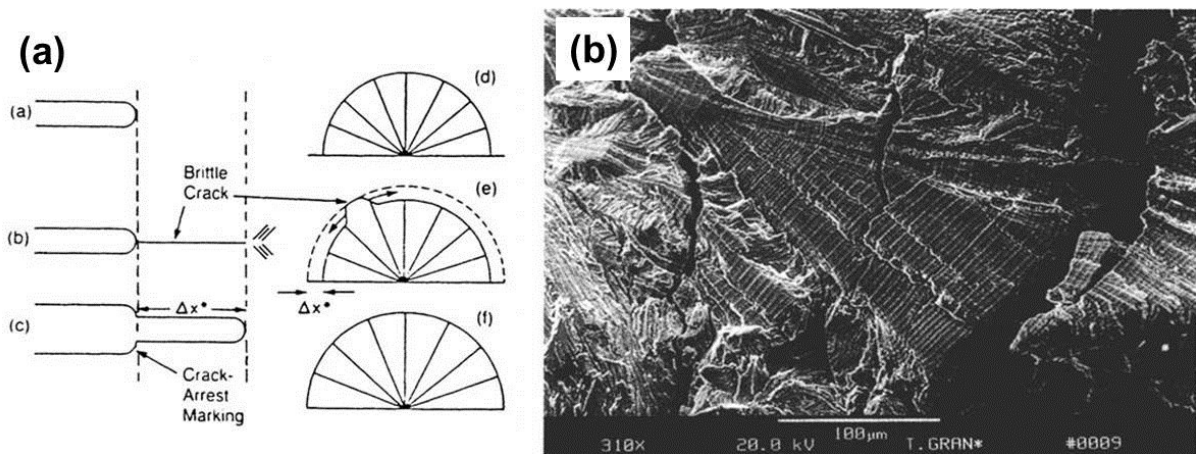
Fig. 4.22 (a) schematic drawing of the transgranular SCC process and the mechanism of striation formation. (After Refs. 29–33. Courtesy of NACE.) (b) Crack arrest marks on a transgranular SCC surface, observed near the overload region on a slow strain rate specimen (10^{-5} s^{-1}) of 70–30 brass tested in pH 7.2 Mattsson's [35] solution with 0.05M NaCl

In this research, the crack arrest marks were observed on a TGSCC (see Fig 4.22-b) fracture surface of SUS316L austenitic stainless steel after SSRT at lower strain rate of 5×10^{-7} s^{-1} in both deaerated SCPW and SCPW with DO 8 ppm, as shown in Fig 4.23. The cracks with slip step and/or grain boundary sliding, which could be formed thorough the metal removal by dissolution model, were also observed on all the specimens of SUS316L tested in SCPW, as shown in Fig 4.24. However, stress assisted intergranular corrosion was not identified from the results of EPMA analysis (see Fig 4.12). Therefore, on the basis of the summarized SCC models as mentioned above, the SCC of SUS316L in SCPW in this research can be explained by the combination of metal removal by dissolution model and film-induced cleavage model.
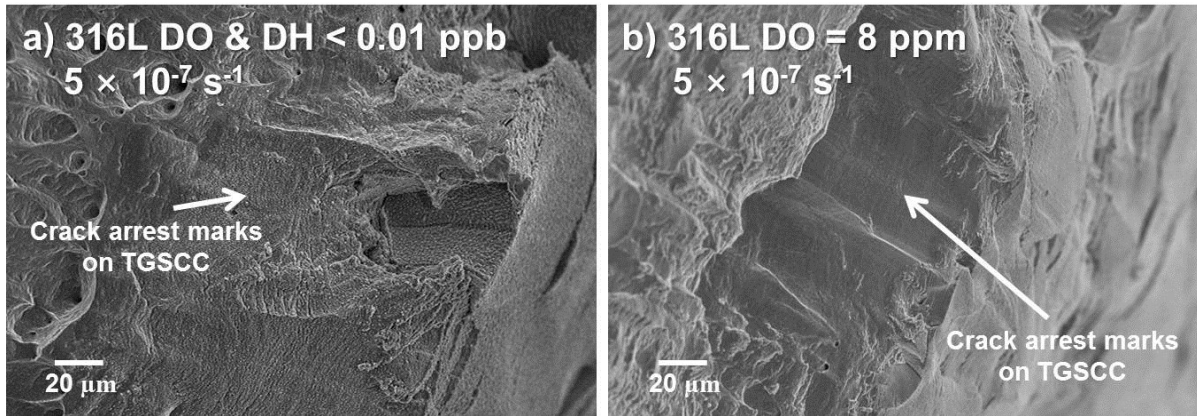
Fig. 4.23 Fracture surface of SUS316L austenitic stainless steel after SSRT at lower strain rate of 5 × 10^{-7} s^{-1} in (a) deaerated SCPW (DO & DH < 0.01 ppb) and (b) SCPW with DO 8 ppm.
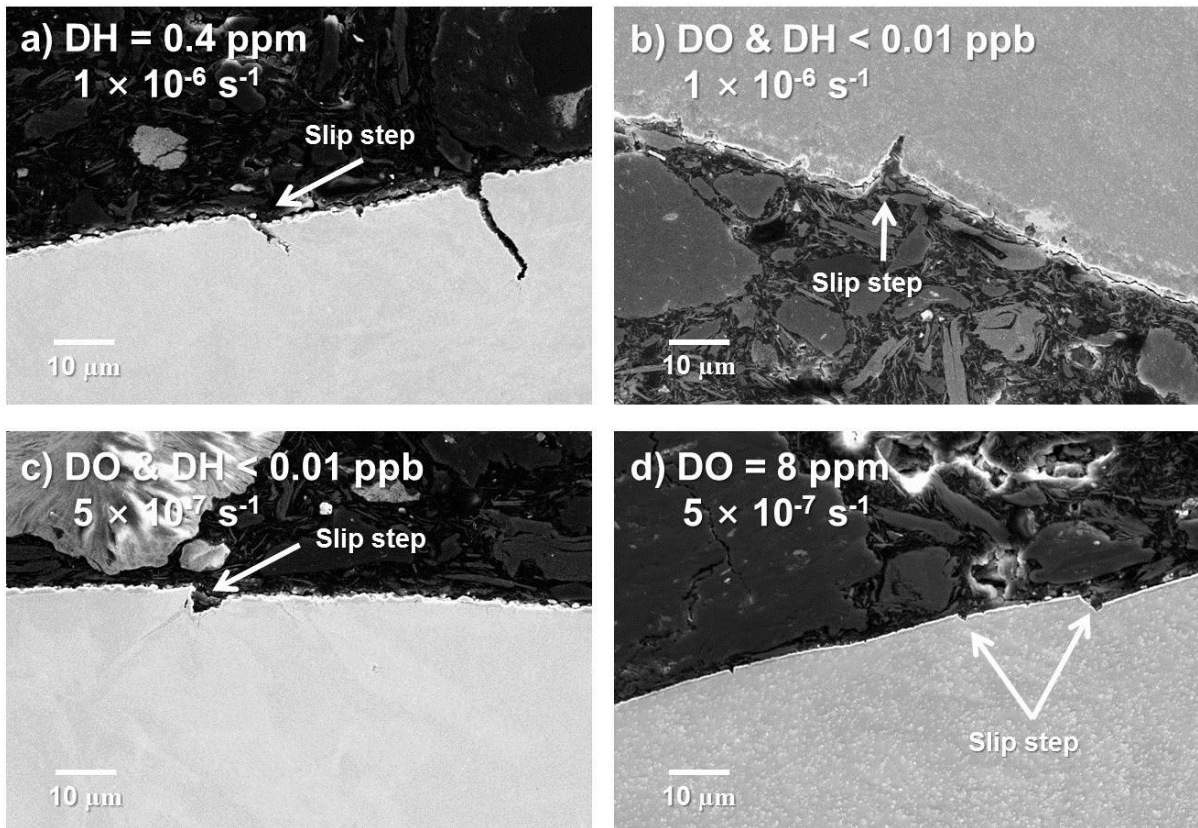
Fig. 4.24 Cross-sectional crack observation formed on SUS316L at lower strain rate of 1 × 10^{-6} s^{-1} or 5 × 10^{-7} s^{-1} in SCPW with a) DH 0.4 ppm, b & c) deaerated and d) DO 8 ppm.

With increasing Cr and Mo contents, the stainless steels become increasingly resistant to the SCC in aggressive solutions. However, the localized loss of chromium, that is Cr-depletion, causes loss of corrosion resistance, because the chromium is crucial in promoting the formation of a Cr-rich passive film on the surface of stainless steels. The effect of Cr content on the SCC is described in Fig. 4.20, when the Cr-depleted zones were formed at grain boundaries. The effect of Ni content upon the SCC of iron-chromium-nickel in $MgCl_2$ is shown in Fig. 4.25, indicating the higher Ni content reduces the risk of SCC. Swann [36] also reports that at high nickel contents the stacking-fault energy is high and planar groups of dislocations are not observed. Molybdenum decreases the SCC susceptibility in the critical Ni concentration level mainly indicating the increase in the critical K_{ISCC} threshold, as shown in Fig 4.26.

The effect of Ni has been interpreted in terms of the planar slip in FCC. The deformation in the FCC metals is controlled by edge dislocations, while that is screw dislocations in BCC metals. Since the Burger's vector of screw dislocations is parallel to the dislocation line, screw dislocations are easily cross slipped, which results in the very fine deformation steps on the specimen surface. In FCC metals, however, cross slip is difficult for edge dislocations, which causes planar slip on the same slip plane, resulting in a big slip step on the specimen surface. In a high stacking faulted energy lattices, an edge dislocation has a narrower disordered region. This causes cross slip be easier for edge dislocation, which reduces surface new steps and suppress the SCC.

However, the relationships between the susceptibility to SCC and steel compositions, condition, and microstructures are complex, as has been often known to be only empirical and sometimes not reproducible. The influence of the composition of an austenitic stainless steel on its susceptibility to SCC is not well-defined. High Ni and Cr contents improve resistance to SCC but, judging from published information, the influences of other alloy components, including Mo and C, which are often components of austenitic stainless steels, do not seem to be reproducible, perhaps because of uncertainties in interactions between the components of the alloys [37].
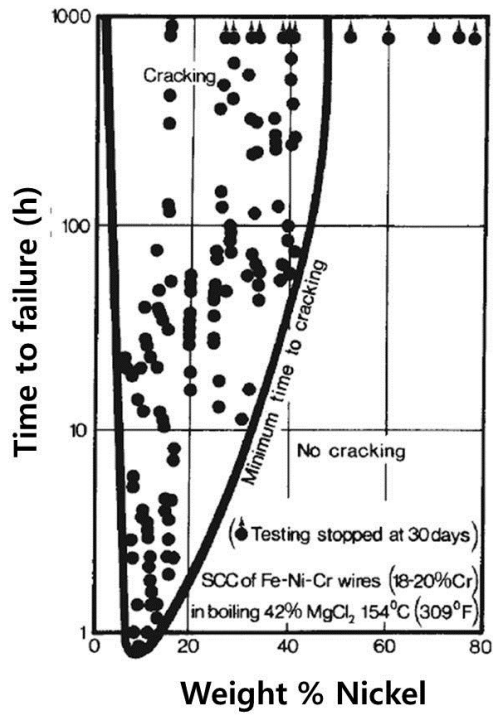
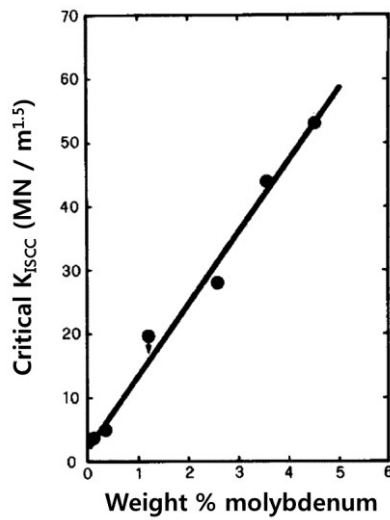Fig. 4.25 Stress-corrosion cracking of iron-chromium-nickel wires in boiling 42% MgCl₂ at 154 °C [38]

Fig. 4.26 The relationship between molybdenum contents and critical KISCC of CrNiMo steel with 15.5-21%Ni 22%Cr in aerated NaCl solution at 105 ℃

Austenitic stainless steels are sensitive to SCC in a specific aggressive environment such as chlorides, while carbon steels, ferritic and ferritic/austenitic (duplex) stainless steels are much resistant to the SCC in chlorides environment. This is because ferritic stainless steels have a ferritic structure with a body centered cubic (bcc) crystal lattice, whereas austenitic stainless steels have a face centered cubic (fcc) crystal lattice. FCC lattice metals are considered to be sensitive for chloride SCC because in this crystal lattice more easily shear occurs along a slip plane with a larger number of atoms [39]. Considering this crystalline structure aspect, F82H ferritic/martensitic steel has better resistance against SCC than 316L austenitic stainless steel. However, some ferritic/martensitic steel exhibits SCC. For example, in SCC of HT-9 ferritic/martensitic steel, IGSCC likely results from grain boundary carbides [40]. From the SCC models summarized above, the possible explanation of the IGSCC of the HT-9 ferritic/martensitic steel can be explained in terms of intergranular corrosion along the carbon segregated zones that provides a stress concentration. It should be noted that the carbon composition of F82H (0.1 wt% C) is half of the HT-9 (0.2 wt% C).

The grain size is also a factor in determining the resistance to SCC. A fine grain size has been shown to increase the resistance to SCC of carbon steels in solutions containing H_2S or nitrates [41], of brass in ammonia [42], and of stainless steels in boiling magnesium chloride [43]. The effect of a coarse grain size on increased susceptibility to SCC has been attributed to the changes in the grain boundary compositions and microstructure. That is, the total quantity of a precipitated phase that is responsible for SCC will become more enriched at grain boundaries as the grains become larger. [44]

In the chapter 3, SCC was not occurred on the ODS ferritic steel in SCPW. Most of all the SCC initiation and development behavior were closely related with the following material aspects, dislocation behavior, slip plane, grain boundary segregation and crystalline structure. Therefore, it is predictable that the ODS ferritic steel shows better resistant against SCC than the other metallic materials, of which the mechanisms are interpreted in terms of acceleration of cross slip by nano-sized oxide particles through the pinning effect, large total area of grain boundaries caused by very fine grains and BCC structure.

4.4 Conclusions

The effect of supercritical water chemistry on the SCC susceptibility of 316L austenitic stainless steel and F82H ferritic/martensitic steel was investigated by the same test method as described in chapter 3.

1) IG-SCC mainly occurred in SUS316L in the SCPW with dissolved hydrogen. On the other hand, the fracture mode at crack initiation stage in SCPW with dissolved oxygen was intermixed with intergranular and transgranular SCC.

2) Although SUS316L exhibits SCC in SCPW with different water chemistry, the susceptibility to SCC was highest in the water with dissolved hydrogen concentration followed by that in the deaerated SCPW, while SCC was so limited in the water with dissolved oxygen.

3) In contrast, F82H ferritic/martensitic steel is resistant to SCC in the SCPW dissolved with hydrogen and oxygen in this test condition, while it suffers from much severe oxidation. The surface cracks observed after the test were oxide layer crack limited to the corrosion products.

4) The SCC of SUS316L in SCPW in this research can be explained by the combination of metal removal by dissolution model and film-induced cleavage model. The resistance to SCC of F82H ferritic/martensitic steels was explained by crystalline structure of lattice: BCC lattice is less sensitive to SCC through the easiness of cross slip.

5) It was predictable that the ODS ferritic steel shows better resistant against SCC than the other metallic materials because nano-size oxide particles can trap dislocations by pinning effect, very fine grain size prevents crack development and ferritic structure is also less sensitive to SCC.

References

1. R. Novotny, P. Hahner, J. Siegl, P. Haušild, S. Ripplinger, S. Penttila, A. Toivonen, Stress corrosion cracking susceptibility of austenitic stainless steels in supercritical water conditions, J. Nucl. Mater. 409 (2011) 117–123

2. N. Muthukumar, J.H. Lee, A. Kimura, SCC behavior of austenitic and martensitic steels in supercritical pressurized water, J. Nucl. Mater. 417 (2011) 1221–1224

3. E.A. West, G.S. Was, IGSCC of grain boundary engineered 316L and 690 in supercritical water, J. Nucl. Mater. 392 (2009) 264–271

4. S. Teysseyre, Z. Jiao, E. West, G.S. Was, Effect of irradiation on stress corrosion cracking in supercritical water, J. Nucl. Mater. 371 (2007) 107–117

5. Rongsheng Zhou, Elaine A. West, Zhijie Jiao, Gary S. Was, Irradiation-assisted stress corrosion cracking of austenitic alloys in supercritical water, , J. Nucl. Mater. 395 (2009) 11–22

6. Yutaka Watanabe, Hiroshi Abe, Yuzo Daigo, Environmentally Assisted Cracking of Sensitized Stainless Steel in Supercritical Water: Effects of Physical Property of Water, GENES4/ANP2003, Sep. 15-19, (2003) 1183

7. G.S. Was, P. Ampornrat, G. Gupta, S. Teysseyre, E.A. West, T.R. Allen, K. Sridharan, L. Tan, Y. Chen, X. Ren, C. Pister J. Nucl. Mater. 371 (2007) 176–201

8. Pantip Ampornrat, Gaurav Gupta, Gary S. Was, Tensile and stress corrosion cracking behavior of ferritic–martensitic steels in supercritical water, J. Nucl. Mater. 395 (2009) 30–36

9. P. Ampornrat, C. B. Bahn, G. S. Was, CORROSION AND STRESS CORROSION CRACKING OF FERRITIC-MARTENSITIC ALLOYS IN SUPERCRITICAL WATER, Proceedings of the 12th International Conference on Environmental Degradation of Materials in Nuclear Power System – Water Reactors – (2005) 1387-1396

10. T. Hirose, K. Shiba, M. Enoeda, M. Akiba, Corrosion and stress corrosion cracking of ferritic/martensitic steel in super critical pressurized water, J. Nucl. Mater. 367-370 (2007)

1185–1189

11. Seong Sik Hwang, Byung Hak Lee, Jung Gu Kim, Jinsung Jang, SCC and corrosion evaluations of the F/M steels for a supercritical water reactor, , J. Nucl. Mater. 372 (2008) 177–181

12. G. Gupta, P. Ampornrat, X. Ren, K. Sridharan, T.R. Allen, G.S. Was, Role of grain boundary engineering in the SCC behavior of ferritic–martensitic alloy HT-9, J. Nucl. Mater. 361 (2007) 160–173

13. W. Bilanin, D. Cubicciotfi, R.L. Jones, A.J. Machiels, L. Nelson and C.J. Wood, HYDROGEN WATER CHEMISTRY FOR BWRS, Prog. Nucl. Energy, Vol. 20 (1987) 43-70

14. K. Dozaki, D. Akutagawa, N. Nogata, H. Takiguchi, and K. Norring, Effects of Dissolved Hydrogen Content in PWR Primary Water on PWSCC Initiation Property, E-Journal of Adv. Maintenance Vol.2 (2010) 65-76

15. Yubing Qiu, Tetsuo Shoji, Zhanpeng Lu, Effect of dissolved hydrogen on the electrochemical behaviour of Alloy 600 in simulated PWR primary water at 290 °C, Corr. Sci. 53 (2011) 1983-1989

16. T. Tsuruta, Proc. of Spring Technical Meeting, Japan Society of Corrosion Engineering, (1983) p78

17. A. Molander, International Workshop on Optimization of Dissolved Hydrogen Content in PWR Primary Coolant, Sendai, 2007

18. C. Soustelle, M. Foucault, A. Gelpi, P. Combrade, and T. Magnin, PWSCC of Alloy 600: A Parametric Study, Proc. Of EUROCORR'98, the Netherlands, (1998)

19. Fanjiang Meng, Zhanpeng Lu, Tetsuo Shoji, Jianqiu Wang, En-hou Han, Wei Ke, Stress corrosion cracking of uni-directionally cold worked 316NG stainless steel in simulated PWR primary water with various dissolved hydrogen concentrations, Corr. Sci. 53 (2011) 2558-2565

20. Xin Gao, Xinqiang Wu, Zhaoen Zhang, Hui Guan, En-hou Han, Characterization of oxide films grown on 316L stainless steel exposed to H_2O_2-containing supercritical water, J. Supercritical Fluids 42 (2007) 157-163

21. Mingcheng Sun, Xinqiang Wu, Zhaoen Zhang, En-Hou Han, Oxidation of 316 stainless steel in supercritical water, Corr. Sci. 51 (2009) 1069-1072

22. Y.J. Kim, Analysis of oxide film formed on type 304 stainless steel in 288 °C water containing oxygen, hydrogen, and hydrogen peroxide, Corrosion 55 (1999) 81-88.

23. T. Terachi, K. Fujii, K. Arioka, Microstructral characterization of SCC crack tip and oxide film for SUS 316 stainless steel in simulated PWR primary water at 320 ∘C, J. Nucl. Sci. Technol. 42 (2005) 225–232.

24. L. Tan, X. Ren, T.R. Allen, Corrosion behavior of 9–12% Cr ferritic–martensitic steels in supercritical water, , Corr. Sci. 52 (2010) 1520-1528

25. R. W. Staehle, in Ref. 4, p. 180.

26. J. R. Myers, "Fundamentals and Forms of Corrosion", Air Force Institute of Technology, Wright-Patterson Air Force Base, Ohio, October (1974).

27. C. Edeleanu and A. J. Forty, *Philos. Mag. 46*:521 (1960).

28. Corrosion Mechanisms in Theory and Practice, Second Edition, 399-450

29. J. A. Beavers, and E. N. Pugh, Metall. Trans. A 11A:809 (1980).

30. E. N. Pugh, *Atomistic of Fracture* (R. M. Latanision and J. R. Pickens, eds.), Plenum, New York, 1983, p. 997.

31. M. T. Hahn and E. N. Pugh, Corrosion 36:380 (1980).

32. D. V. Beggs, M. T. Hahn and E. N. Pugh, *Proceedings of the A. R. Troiano Honorary Symposium on Hydrogen Embrittlement and Stress-Corrosion Cracking* (R.Gibala and R. F. Hehemann, eds.), ASM, Metals Park, OH, 1984.

33. E. N. Pugh, *Corrosion 41*:517 (1985).

34. E. N. Pugh, *Atomistic of Fracture* (R. M. Latanision and J. R. Pickens, eds.), Plenum, New York, 1983, p. 997.

35. E. Mattsson, *Electrochim. Acta 3*:279 (1961).

36. Swann, P. R., Corrosion, 19, 102t (1963)

37. David Talbot and James Talbot, Corrosion Science and Technology, 1998.

38. H. Copson , in Physical Metallurgy of Stress Corrosion Fracture , T. Rhodin , editor, Interscience , New York , 1959 , p. 247 .

39. Mark Brouwer, http://stainless-steel-world.net/pdf/urea_Chlorides.pdf, Chlorides in urea plants, Mechanical Paper May 2009.

40. G. Gupta, P. Ampornrat, X. Ren, K. Sridharan, T.R. Allen, G.S. Was, Role of grain boundary engineering in the SCC behavior of ferritic–martensitic alloy HT-9, J. Nucl. Mater. 361 (2007) 160–173

41. S. W. Ciaraldi in "Stress-Corrosion Cracking", R. H. Jones, Ed., p. 41, ASM International, Materials Park, OH (1992).

42. E. N. Pugh, J. V. Craig, and A. J. Sedriks in "Fundamental Aspects of Stress Corrosion Cracking", R.W. Staehle, A. J. Forty, and D. van Rooyen, Eds., p. 118, NACE, Houston, TX (1969).

43. R. M. Latanision and R. W. Staehle in "Fundamental Aspects of Stress Corrosion Cracking", R. W. Staehle, A. J. Forty, and D. van Rooyen, Eds., p. 214, NACE, Houston, TX (1969).

44. E. McCafferty, Introduction to Corrosion Science, 336

Chapter 5

Effects of Specimen Geometry and Surface Condition on the SCC Susceptibility in SCPW

5.1 Introduction

Increasing interest in the application of oxide dispersion strengthened (ODS) steels to the advanced nuclear power system requires a sound understanding of the material's mechanical behavior, including the effect of specimen morphology.

Using the miniaturized specimens offers many advantages for the research of fission and fusion reactor materials. For example, many of specimens can be irradiated at once despite a very small irradiation volume in a testing reactor. Also, direct observation of deformation behavior after applying a load is possible without additional preparatory procedures which may bring about mechanical damage [1]. Hence, various types of miniaturized mechanical tests have been developed for the research of fission and fusion reactor materials [2,3]. Among them, a miniaturized tensile specimen with a gauge section of $5 \times 1.2 \times 0.25$ mm has been proposed and has been utilized in Japan [4]. Most of the size effect considered for metal produced by cast. Therefore, the size effect of oxide dispersion strengthened (ODS) steels which produced by mechanical alloy method is worth considering.

On the other hand, corrosion resistance and SCC of steel and its correlation with surface topography have been important concerns for structural metallic materials. In the case of stainless steel, this is because the dense chromium oxide layer on the stainless steel surface prevents corrosion and surface roughness can affect this layer [5].

In this present work, the morphologic effects such as surface roughness and specimen size and shape were discussed for the structural metallic materials base on the result from SSRT in vacuum and SCPW.

5.2 Specimen preparation

The chemical composition of SOC-16 oxide dispersion strengthened ferritic steel, SUS316L austenitic steel and F82H ferritic-martensitic steel are listed in Table 5.1. The 2 different kinds of tensile specimens were prepared to evaluate the shape and side effect of the tested materials. One is a plate shape with 5 mm of gauge length, 1.2 mm of width and 0.45 mm of thickness, called SSJ2 specimen. Another is a round bar specimen which had a gauge section of 2.1 mm diameter by 10 mm, as shown in Fig. 5.1. The surface of the round bar and SSJ2 specimens was mechanically polished by SiC abrasive paper to #4000 and by buff with diamond abrasive of 0.25 μm, respectively. In case of SOC-16 and F82H, tensile specimens were cut out from the extruded bars in the longitudinal

directions. Solid solution heat treatment was done for SUS316L.

Table 5.1. Chemical compositions of SOC-16 ODS ferritic steel, F82H ferritic-martensitic steel, and SUS316L austenitic steel. (wt %)

Material	C	Si	Cr	W	Al	Ti	Y	O	N	Ar	Hf	Zr	Y_2O_3
SOC-16	0.043	—	14.54	1.93	3.01	0.13	0.28	0.17	0.006	0.0064	0.62	—	0.36
Material	C	Si	Mn	Cr	Ni	P	S	W	V	Ta	N	B	Mo
F82H	0.10	0.2	0.5	8.0	—	—	—	2.0	0.20	0.04	<0.01	0.003	—
SUS316L	0.01	0.73	1.06	17.41	12.13	0.032	0.004	—	—	—	—	—	2.05
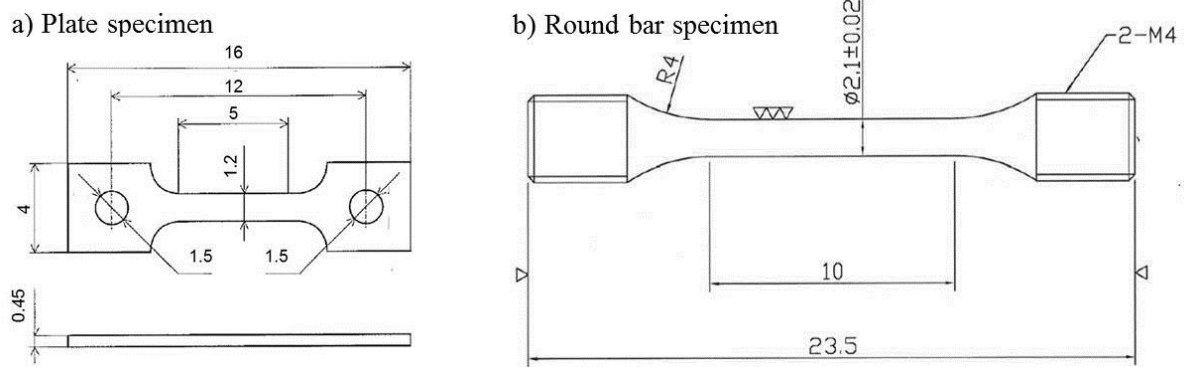
Fig 5.1. The geometry of tensile specimens for SSRT

5.3 Strain rate behavior on the different size and shape of specimens in vacuum.

With the different size and shape of specimens, steady strain rate test was carried out at a temperature of 773 K with strain rate ranging from 1×10^{-3} s^{-1} to 1×10^{-6} s^{-1} in a vacuum in order to evaluate the morphological effect.

5.3.1 Results and discussion.

The stress-strain curves of SOC-16, F82H and SUS316L after SSRT in vacuum was compared between the plate specimen and the round bar specimen, as shown in Fig 5.2.

110

For both plate and round bar specimen, the results of SSRT in a vacuum indicate that the ultimate tensile strength and yield strength decreased with increasing strain rate for the ODS ferritic steel and F82H ferritic/martensitic steel, while SUS316L austenitic stainless steel shows higher UTS at lower strain rate. This phenomenon for SUS316L may explained by the difference of microstructure and/or the typical work hardening which is the strengthening of a metal by plastic deformation.

A miniaturized tensile specimen of 5 mm gauge length, 1 mm width and 0.4 mm thickness was recommended by P. Jung and G.E. Lucas et. al [6] if grain size is less than 0.06 mm. The miniaturized specimen was considered with a number of factors such as 1) grain size effects on yield stress by a Hall-Petch relation, 2) the ratio of thickness, width and length to grain size, 3) the ratio of thickness to width, called aspect ratio and 4) the ratio of gauge length to area. The recommended miniaturized tensile specimen is very similar to the plate specimen in this work. And the SSRT results from SUS316L and F82H corresponded well between plate specimen and round bar specimen. It implies that both plate and round bar specimen are effective to evaluate the deformation behavior by SSRT in inactive environment such as vacuum.

In contrast, SOC-16 ODS ferritic steel exhibits slight different stain rate dependence between plate and round bar specimen, although the grain size of ODS steel much less than the miniaturized specimen's grain size of 0.06 mm. The SSRT results from plate specimen show relatively constant elongation with different stain rates, while that of round bar specimen demonstrated the typical strain rate effect. This difference to the plate specimen of ODS steel may explained by the pinning effect of the oxide particles along with Hall-Petch relation in high temperature condition. Therefore, the miniaturized tensile specimen for the ODS steel needs to be considered.
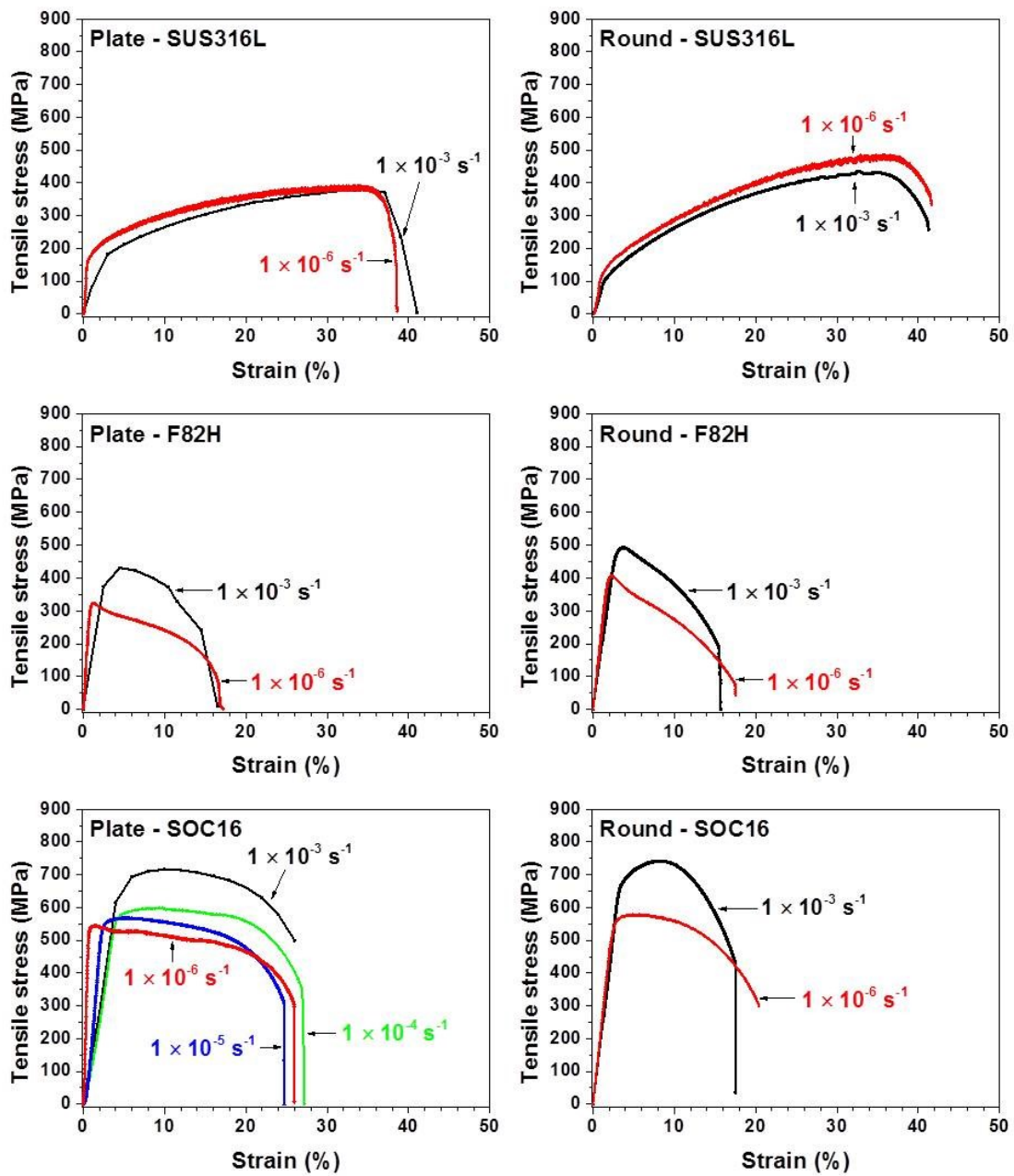
Fig 5.2. Stress-strain curves of SOC-16, F82H and SUS316L after SSRT in vacuum with different specimen morphology.

5.4 Fracture behavior observation after SSRT in SCPW for the different size and shape of specimens

After SSRT for the plate and round bar specimen in SCPW, fracture surface and side region observation was conducted by SEM. The stress–strain curves for plate specimens tested in SCPW were not obtained because it was too small to detect the applied load for the owned equipment. To investigate the surface roughness effect for the ODS steel in SCPW, machined specimen and ground specimen (#4000) after forming processing were compared for the round bar specimen. The SCPW was controlled at a pressure of 25 MPa, 773 K and the dissolved oxygen (DO) concentration below 0.01 ppm by injections of high pure nitrogen gas to the conditioning tank.

5.4.1 Results and discussion

The SEM images of fracture surface and gauge section after SSRT in SCPW with plate specimen and round bar specimen were shown in Fig 5.3 and 5.4, respectively. At higher strain rate, necking was observed for all the tested materials in a SCPW, regardless of specimen morphology. However, necking was not observed on the ODS steel tested by plate specimen at lower strain rate while round bar specimen exhibits cup and corn fracture shape with necking at the same test environment and condition. Reduction in area measurement shows good agreement to the SEM observation, indicating that the RA value of ODS steel drastically decreased with decreasing strain rate for the plate specimen, as shown in Fig 5.5.

Most of work for the SCC susceptibility of metal by means of SSRT technic adopted a specimen with round shape of gauge section. And several works with plate tensile specimen were also conducted for ferritic–martensitic (F/M) and austenitic steels at a high temperature water and SCPW [7-12]. Among them, a few research group used SSJ2 specimen [10-12]. For research on the irradiation-assisted stress corrosion cracking (IASCC), all the tested plate tensile specimens were larger than SSJ2 and the recommended miniaturized specimen [13-15]. From the observed deformation and strain rate behavior above, SSJ2 specimen demonstrates reliable fracture and deformation behavior for the austenitic stainless steels and ferritic/martensitic steels. Meanwhile, the specimen miniaturization of ODS steel for SSRT in corrosive environment could be considerable.
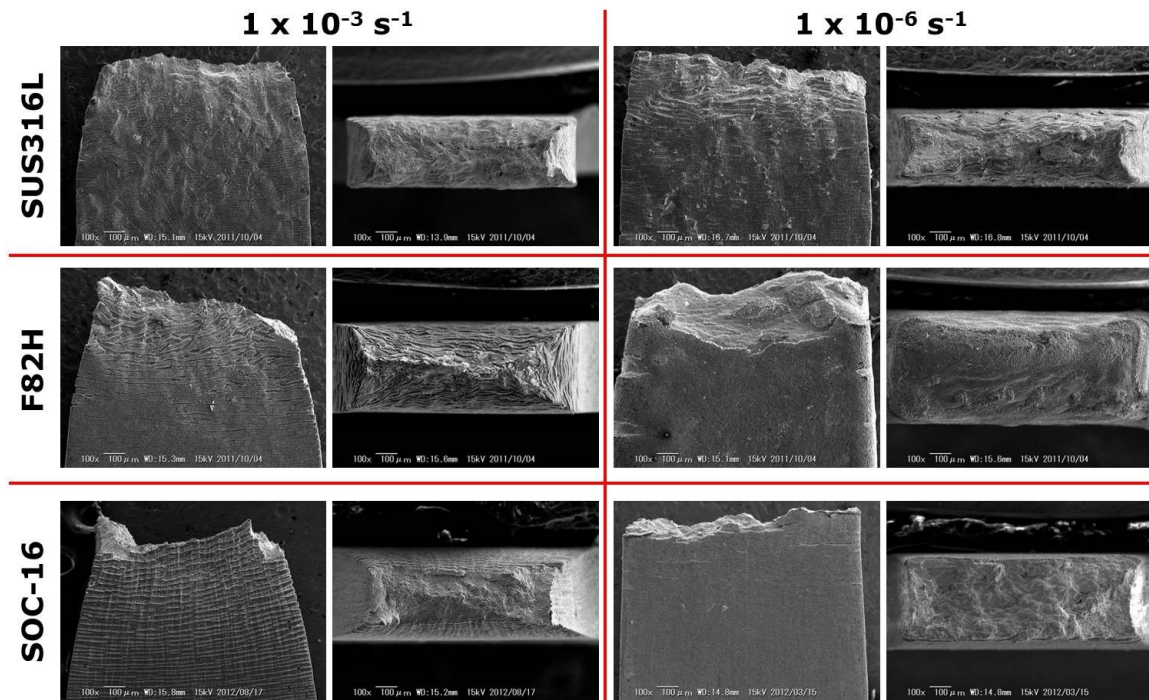
Fig. 5.3. Fracture surface and gauge section of the plate specimen after SSRT in SCPW at higher strain rate (1×10^{-3} s^{-1}) and lower strain rate (1×10^{-6} s^{-1})
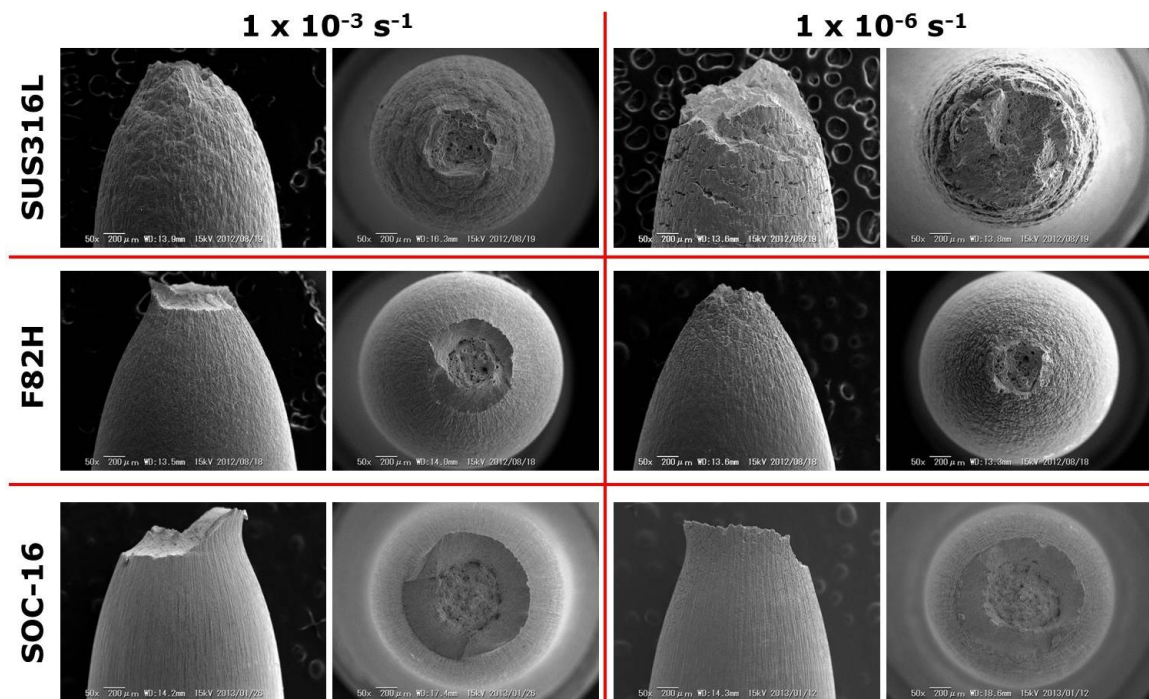
Fig. 5.4. Fracture surface and gauge section of the round bar specimen after SSRT in SCPW at higher strain rate (1×10^{-3} s^{-1}) and lower strain rate (1×10^{-6} s^{-1})
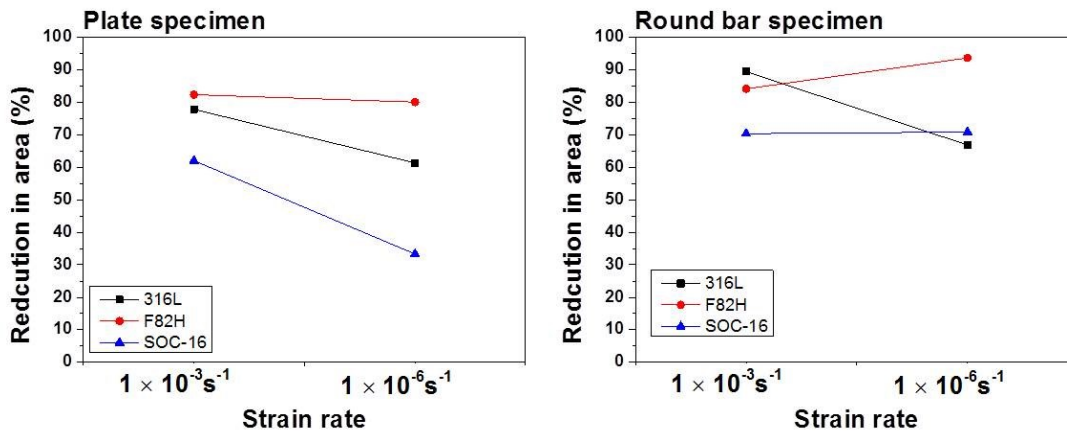
Fig. 5.5 Reduction in area as a function of strain rate with different specimen shapes.

Since SCC is a surface phenomenon, the crack initiation can be influenced by surface area ratio, the periphery length/cross sectional area, as a surface effect. Fig 5.6 indicates that surface effect can be more remarkable in the plate type specimens than round bar type specimens. Especially for corrosion issue, plate specimens suffer much corrosion than round bar specimens. The oxide film cracking can be interpreted in terms of specimen geometry effect.
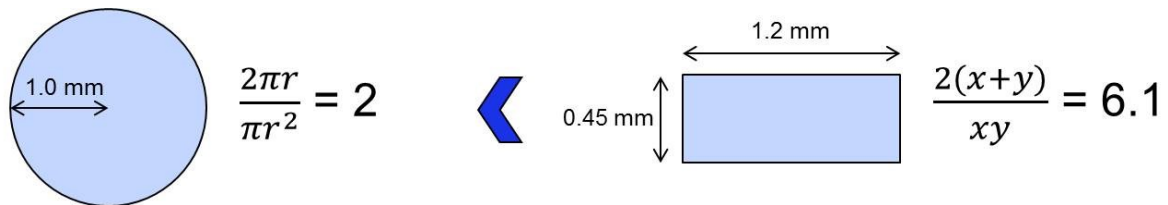
Fig. 5.6 The surface area ratio of the tested round bar and plate specimen.

With rectangular test pieces, the corners prevent uniform flow from occurring, and consequently, after fracture, the shape of the reduced area is not rectangular and deformation and fracture are concentrated in the area far from the corners, as shown in Fig 5.7. This may accelerate oxide film cracking. It is considered that the combined effect of the specimen surface area ratio effect and specimen corner effect is possible explanation of the degradation to the plate specimen of ODS steel in active environment.
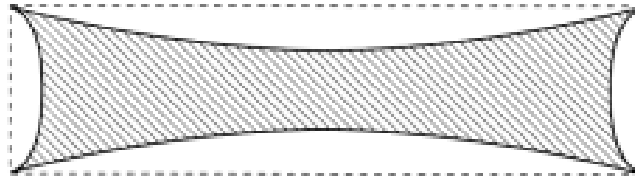
Fig. 5.7. Sketch of end view of rectangular test piece after fracture showing constraint at corners indicating the difficulty of determining reduced area.

Fig. 5.8 shows the surface roughness effect of ODS steel after SSRT in SCPW at lower strain rate. The ground specimen (#4000) exhibits cup and corn facture shape with necking. In contrast, less reduced area by deforming to fracture appears on the machined specimen (non-polished).

The effect of surface roughness for austenitic 301, 304, 316L stainless steels clearly shows the improved corrosion resistance by sound surface finishing [16-18]. T. Hong and M. Nagumo [16] demonstrated that the change in potential relates with the change in grit number of silicon carbide paper.

On the surface of the non-polished ODS tensile specimen, some level of residual stress fields could be generated during fabrication process. It is well known that residual stress fields can accelerate SCC, possibly in such situations as associated with the presence of hydrogen, where the corresponding strain field influences hydrogen entry and diffusion toward the fracture process zone [19]. Therefore, it is expected that the residual stress on non-polished ODS specimen can affect SCC susceptibility. However, in the previous chapter, it was demonstrated that the ODS steel shows excellent resistance to SCC with the aspects of tensile stress and SCPW environment. According to the literature survey results, which described at above, and SEM observation results of ODS steel, the surface roughness or the residual stress of ODS steel could be a factor to determine the SCC susceptibility to the SCPW.
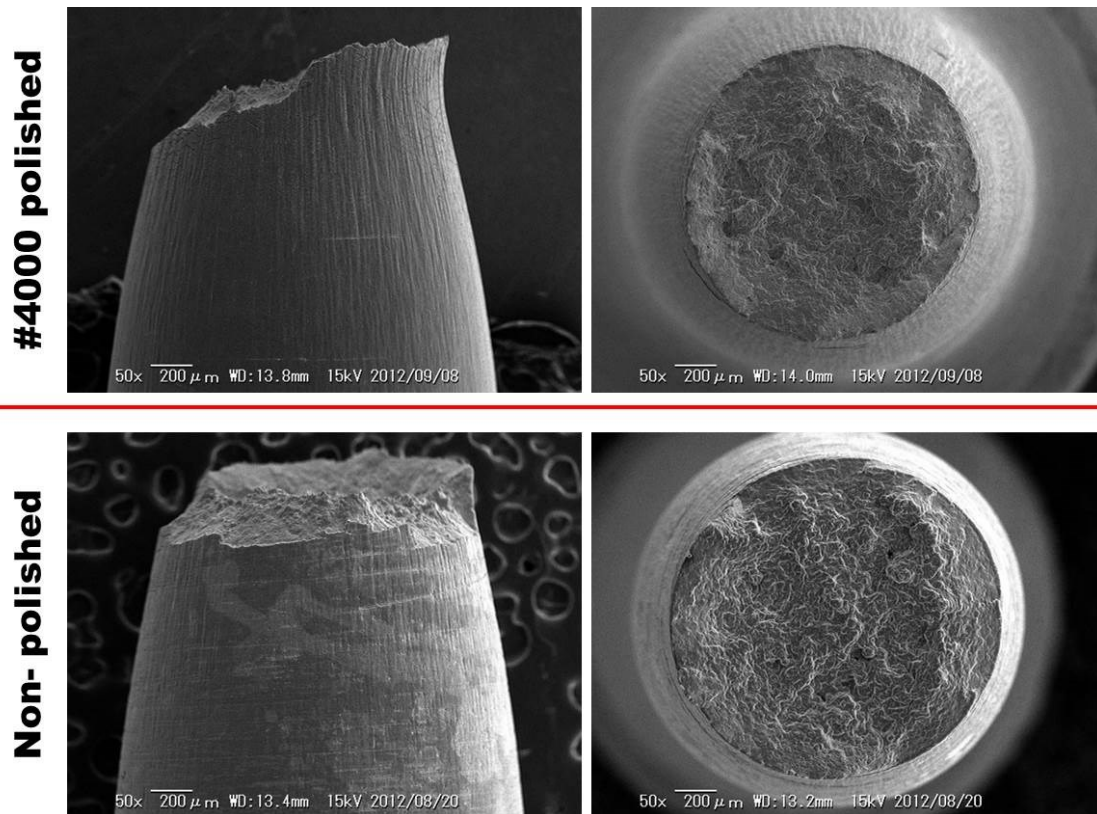
Fig. 5.8. Fracture surface and gauge section of the round bar specimen with different surface condition after SSRT in SCPW at lower strain rate (1×10^{-6} s^{-1})

5.5 Conclusions

In this chapter, the morphologic effects such as surface roughness and specimen size and shape were discussed for the structural metallic materials base on the result from SSRT in vacuum and SCPW.

1) In the case of austenitic stainless steel and ferritic/martensitic steel, the miniaturized specimen can give reliable deformation and fracture behavior information to the SCC susceptibility by means of SSRT.

2) However, ODS steel needs careful consideration of miniaturization and surface finishing in order to evaluate the SCC susceptibility with using SSRT technique.

3) Surface roughness or residual stress of ODS steel could be a factor to determine the SCC susceptibility to the SCPW.

117

References

1. Akira Okata, Keiji Kanao, "Speicmen size dependence of Tensile properties of Au, Cu, Ni and Fe irradiated with D-T Neutrons." Materials Transactions, JIM, Vol.30, No.8 (1989) 549-556

2. For example, W.R. Corwin and G. E. Lucas ed.: The Use of Small Specimens for Testing Irradiated Materials, ASTM Special Technical Publication 888, Phil., Pa., (1986).

3. A. Kohyama and N. Igata : J. Atomic Soc. Japan, 25 (1983) 329.

4. A. Kohyama, K. Hamada and H Matsui, Specimen size effects on tensile properties of neutron-irradiated steels. J. Nucl.Mater., 179-181 (1991) 417-420.

5. Surface roughness and the corrosion resistance of 21Cr ferritic stainless steel

6. Recommendation of miniaturized techniques for mechanical testing of fusion materials in an intense neutron source

7. Effect of irradiation on SCC in SCW

8. SCC evaluation of type 304 and 316 austenitic STS in acidic chloride solutions using the SSRT

9. Crack initiation model for sensitized 304 strainless steel in high temperature wate

10. SCC behavior of austenitic and martensitic steels in supercritical pressurized water

11. Improvement of compatibility of advanced ferritic steels with SCPW toward a high thermally efficient water-cooled blanket system (2006)

12. SCC behavior of SUS316L in the high temperature pressurized water environment (2011)

13. Effects of water and irradiation temperatures on IASCC susceptibility of 316 STS_2004

14. Investigation of liquid LBE embrittlement effects on irradiated F-M steels by SSRT_2012

15. SCC on irradiated 316 STS_2001

16. Effect of surface roughness on early stages of pitting corrosion of SUS301

17. Electropolishing effects on corrosion behavior of 304 stainless steel in high Temp. hydrogenated water

18. Impact of surface condition on sulphide stress corrosion cracking of 316L stainless steel. (2013)

19. J. Toribio, Residual Stress Effects in Stress-Corrosion Cracking, JMEPEG (1998) 7: 173-182

Chapter 6

Deformation and Fracture Behavior of ODS Steels in Vacuum

6.1 Introduction

Since the Industrial Revolution in the 17th century, CO_2 concentration in the atmosphere has been increased as a result of human activities, such as the burning of oil, coal and gases, as well as deforestation. Recently, global atmospheric concentration of CO_2 was about 35% higher than that before the Industrial Revolution. Nuclear power is considered to be contributing to environmental benefits with reducing CO_2 emission.

One of the critical issues towards high burn-up operation of nuclear power plant has been considered to be development of fuel clad material that can overcome the requirement of materials performance, such as low susceptibility to stress corrosion cracking (SCC) and high temperature performance. Oxide dispersion strengthened (ODS) steels have been developed for the application to fuel cladding material [1-6]. Since high-strength ODS steels are considered to be susceptible to SCC, evaluation of SCC behavior of ODS steels is important for practical application to the life-extension and the safety operation of nuclear power plants. Strain rate dependence of the fracture mode is a characteristic trend of SCC of metallic materials. Before investigating the SCC behavior in corrosion environment, such as supercritical pressurized water, strain rate dependence in a vacuum should be investigated as basal information of material behavior.

In this study, the effect of strain rate on the deformation behavior was investigated at high-temperatures in order to get fundamental data for research on the susceptibility to SCC of ODS steels and to apply it to advanced fossil and nuclear power plants.

6.2 Experimental

The materials used were three kinds of 15Cr-4Al-2W-ODSsteels of which the other chemical compositions were slightly changed by the addition of small amount of alloying elements. The chemical compositions were shown in Table 6.1. The details of the fabrication process of the ODS steels are given in the previous papers [1-3]. All of the ODS steels were finally heat treated at 1323K for 1h, then air-cooled. The tensile specimens with a gauge length of 5 mm, a width of 1.2 mm and a thickness of 0.45 mm were cut out from the extruded bars in the longitudinal directions. To prevent the effect of surface defect on the deformation process during the tensile test, the surface of specimens was mechanically polished using 0.25 μm alumina abrasive particles.

Table 6.1 Chemical compositions of ODS steels (SOC-9, SOC-14 and SOC-16) (wt%)

Material	C	Cr	W	Al	Ti	Y	O	N	Ar	Hf	Zr	Y$_2$O$_3$
SOC-9	0.03	15.42	1.85	3.8	0.1	0.28	0.16	0.004	0.0068	—	—	0.36
SOC-14	0.052	14.85	1.84	3.73	0.09	0.27	0.17	0.009	0.0061	—	0.63	0.34
SOC-16	0.043	14.54	1.93	3.01	0.13	0.28	0.17	0.006	0.0064	0.62	—	0.36

Steady strain rate tests (SSRT) were performed at a strain rate ranging from 1×10^{-3} s^{-1} to 1×10^{-6} s^{-1} in a vacuum of 2.3×10^{-3} Pa at a temperature of 773K. The test temperature was controlled within in an error of ±3 K.

The fractured surface was observed by scanning electron microscope (SEM), and the reduction in area of the tested specimens was measured to investigate the effects of strain rate on the fracture mode in inactive environment.

6.3 Results

6.3.1 Tensile properties

Fig. 6.1 (a), (b), and (c) show the stress-strain curves of ODS steels at 773K in a vacuum with the different strain rate ranging from 1×10^{-3} s^{-1} to 1×10^{-6} s^{-1}, as a function of materials which are SOC-9, SOC-14 and SOC-16, indicating the lower the strain rate, the lower the ultimate tensile strength for all the materials used in this research at the test conditions. However, the tensile strength of all the materials is very similar at each strain rate and no strain rate dependence is observed for the steels, although the tensile elongation is different among the materials more or less at each strain rate. The yield strength of the ODS steels decreased with decreasing strain rate, as shown in Fig. 6.1 (d).
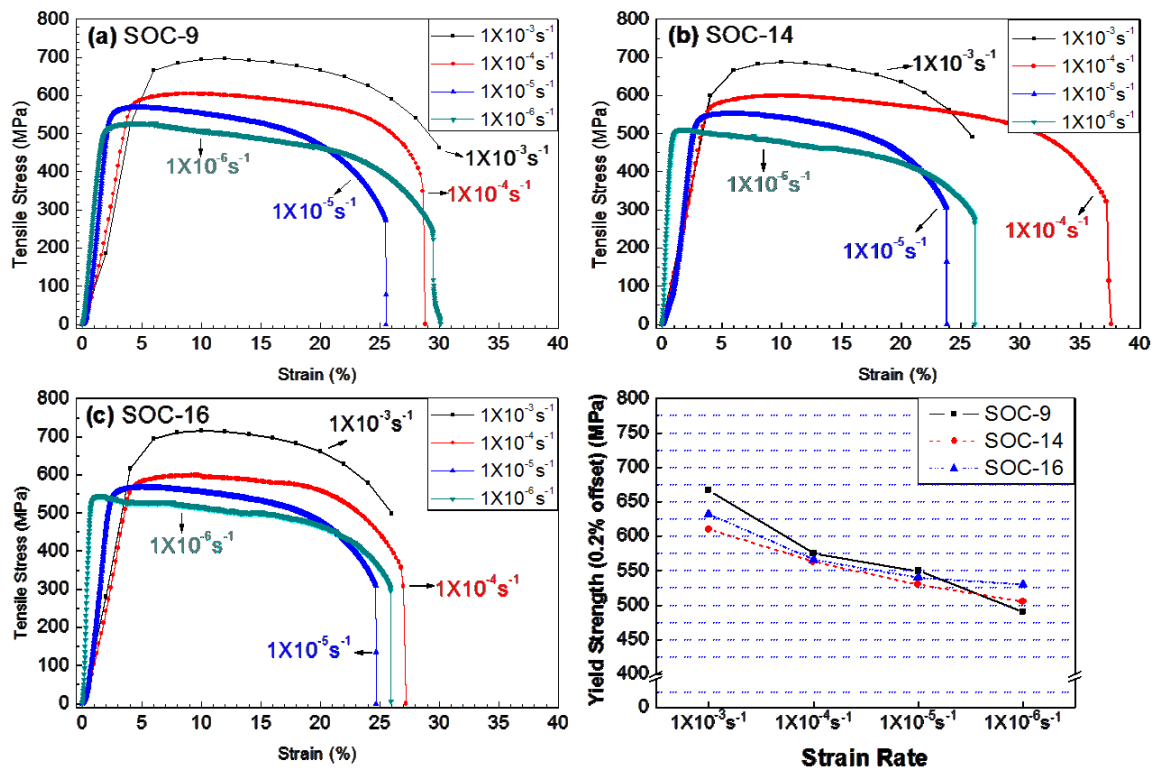
Fig. 6.1   Tensile test results of steady strain rate test for ODS steels at 773K in a vacuum at different strain rates ranging from $1 \times 10^{-3}\,s^{-1}$ to $1 \times 10^{-6}\,s^{-1}$: (a) SOC-9, (b) SOC-14, (c) SOC-16, and (d) yield stress of ODS steels as a function of strain rate

In the previous works on tensile tests at 973K, the tensile strength of Al-added ODS steels (SOC-9) was increased by the addition of Zr (SOC-14) or Hf (SOC-16). However, in this study the tensile strength of these materials is almost same at test temperature of 773K. At 973K, the deformation mechanism of ferritic steels has been considered to be grain boundary sliding which accelerates creep deformation at a lower applied stress than yield stress. SOC-14 and -16 ODS steels showed a higher creep strength than SOC-9 ODS steel, which is due to the suppression of the grain boundary sliding by the precipitation of Zr or Hf carbides and oxides at grain boundaries but not strengthening.

6.3.2 Fracture mode

The susceptibility of SCC can be evaluated by the observation of fracture mode change from ductile to brittle grain boundary and/or cleavage fracture and measuring reduction in area. Reduction in area after SSRT of ODS steels in a vacuum was shown in Fig. 6.2(a). Relatively constant value from 65% to 80% was obtained without regarding to material.

Fig. 6.2(b) is representative fracture surface and specimen side surface of SOC-14 which was deformed at strain rates of $1 \times 10^{-3}\,s^{-1}$ and $1 \times 10^{-6}\,s^{-1}$. The dimple size of the fracture surface which tested at the strain rate of $1 \times 10^{-3}\,s^{-1}$ is smaller than that of the fracture surface which tested at the strain rate of $1 \times 10^{-6}\,s^{-1}$. However, according to the result of reduction in area and the observation of fractured surface, all the specimens tested in this study exhibit ductile fracture mode, indicating high reduction in area and many dimples on the fracture surface.

(a) Reduction in area after tensile test of the specimens (b) SEM images of SOC-14 after fracture
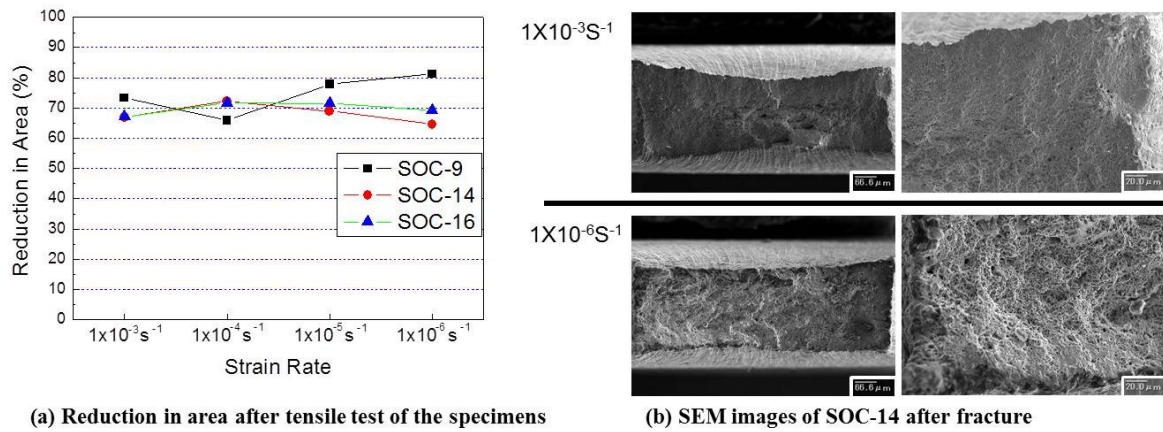
Fig. 6.2 Analysis of fracture mode : (a) Reduction in area after tensile test of the specimens, (b) SEM images of SOC-14 after tests at the strain rate of 1×10^{-3} and $1 \times 10^{-6}\,s^{-1}$

6.4 Discussion

There is a simple relationship between the plastic strain and the dislocation density. It is based on the fact that when a dislocation moves, two atoms on sites adjacent across the plane of motion are displaced relative to each other by the Burgers vector b. With this relationship, therefore, it is well known that the strain rate ($\dot{\varepsilon}$) can be expressed by

$$\dot{\varepsilon} = \rho_m b \bar{v} \qquad (1)$$

124

where b is Burgers vector, ρ_m is density of mobile dislocations, and $\bar{\upsilon}$ is average velocity of dislocation.

By repeating the experiment for different times and stress levels the velocity can be determined as a function of stress as shown in Fig. 6.3. In the range of velocity between 10^{-7} and 10^{-3} cm s^{-1}, the logarithm of the velocity varies linearly with the logarithm of the applied stress, thus

$$v \propto \left(\frac{\tau}{\tau_0}\right)^m \qquad\qquad (2)$$

where v is the velocity of dislocations, τ is the applied shear stress resolved in the slip plane, τ_0 is the shear stress for $\upsilon = 1$ cm s^{-1}, m is a constant [7]. The value of $m \approx 31$ was revealed by means of plotting from the results of SSRT for ODS steels. The dislocation velocity of ODS steels at tested conditions was very sensitive to the applied shear stress, compare to the other materials. This implies that the deformation mechanism of the ODS steels could be interpreted in terms of thermally activated dislocation motion and/or possibly grain boundary sliding, namely "dislocation mechanism".
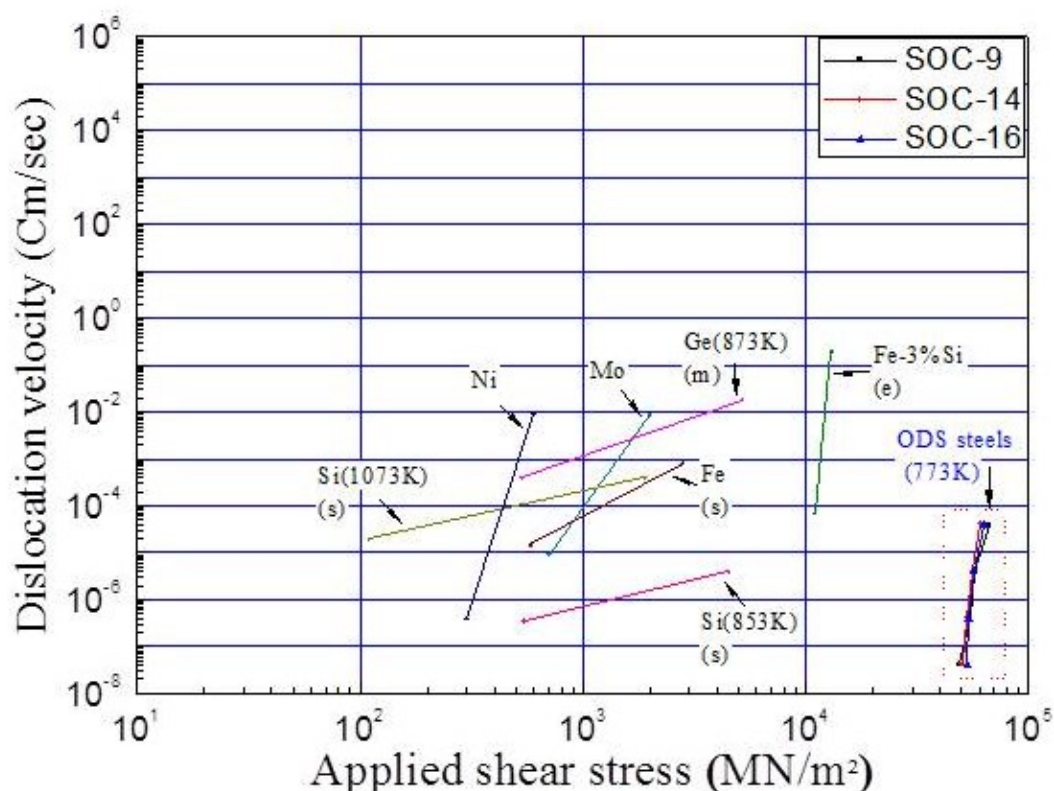

Fig. 6.3. The dependence of dislocation velocity on applied shear stress with various kinds of materials and ODS steels

125

6.5 Conclusions

In this study, the strain rate effects on high-temperature tensile properties of high-Cr ODS steels were investigated as a basal information of SCC research for ODS steels. The susceptibility of SCC is generally evaluated by SSRT at different strain rates. Before the tests in corrosive environment, the test was carried out in a vacuum to investigate strain rate effects without any corrosive environment. And the main results obtained are the following:

1) The result of SSRT in a vacuum at 773K with the different ODS steels (SOC-9, SOC-14, SOC-16) shows that the lower the strain rate, the lower the tensile strength. However, no material dependence was shown with the tested specimens.

2) Tensile yield stress is remarkably dependent on the strain rate, showing a large increase with increasing strain rate, while tensile elongation is not remarkably influenced by strain rate.

3) Reduction in area after SSRT in a vacuum at 773K was relatively constant, regardless of strain rate.

4) According to the precise observations of fractured surface, there was no strain rate effect on the fracture mode, and only ductile fracture was observed for all the specimens tested in the study. This trend was independent of material.

5) The m value in Eq. (2) for the ODS steels was 31 that is very large, implying that the deformation mechanism is related with thermally-activated dislocation motion and/or possibly grain boundary sliding.

References

1. Kimura A, Cho H.S, Lee J.S, Kasada R, Ukai S, Fujiwara M (2004) R&D of Oxide Dispersion Strengthened Steels for High Burn-up Fuel Claddings. Proceedings of ICAPP '04, Paper 4009 : 2070-2076.

2. Takaya S, Furukawa T, Inoue M, Fujisawa T, Okuda T, Abe F, Ohnuki S, Kimura A (2008) Corrosion resistance of Al-alloying high Cr-ODS steels in stagnant lead-bismuth、J. Nucl. Mater., 83, 1471-1476.

3. Iwata N.Y, Kasada R, Kimura A, Okuda T, Inoue M, Abe F, Ukai S, Fujisawa T (2009), Characterization of mechanically-alloyed powders for high-Cr oxide dispersion strengthened ferritic steel, ISIJ International, Vol.49, 12, 914-919.

4. Takaya S, Furukawa T, Aoto K, Müller G, Weisenburger A, Heinzel A, Inoue M, Okuda T, Abe F, Ohnuki S, Fujisawa T, Kimura A (2009) Corrosion behavior of Al-alloying high Cr-ODS steels in lead-bismuth eutectic, J. Nucl. Mater, 386-388, 507-510.

5. Chen J, Pouchon M.A, Kimura A, Jung P, Hoffelner W (2009) Irradiation creep and microstructural changes in an advanced ODS ferritic steel during helium implantation under stress, J. Nucl. Mater, 386-388, 143-146.

6. Oh S, Lee J.S, Jang C, Kimura A (2009) Irradiation hardening and embrittlement in high-Cr oxide dispersion strengthened steels, J. Nucl. Mater, 386-388, 503-506.

7. Hull D, Bacon D.J (2001) Introduction to dislocations 4th edition, 49-59

Chapter 7

Summary and Conclusions

The foremost consideration in the successful development and deployment of advanced nuclear reactor is the safety, performance and reliability of the systems. One of the critical issues for these requirements can be the soundness of structural materials, which endure high-temperature, high neutron doses and extremely corrosive environment. Therefore, oxide dispersion strengthened steels have been considered to be candidates for several advanced nuclear systems with higher thermal efficiency, because of their excellent performance as structural component in such a severe environments. However, the experimental data on the SCC susceptibility of "ODS steels" in supercritical pressurized water (SCPW) has not been reported to our knowledge. And all of the tests for SCC susceptibility in SCPW were conducted in SCPW dissolved with oxygen but not in SCPW dissolved with hydrogen.

In this research, the stress corrosion cracking susceptibility and fracture mode of ODS ferritic steel and conventional structural steels such as F82H ferritic/martensitic steel and SUS316L austenitic stainless steel in supercritical pressurized water (25 MPa, 500 °C) dissolved with various oxygen and hydrogen contents were investigated by means of steady strain rate tests (SSRT), which were performed at a higher strain rate of 1×10^{-3} s^{-1} and lower strain rates of 1×10^{-6} s^{-1} or 5×10^{-7} s^{-1}. The DO and DH contents of the water are DH = 0.4 ppm, DO and DH < 0.01 ppb and DO = 8 ppm. In addition, high temperature tensile test in vacuum was also performed at 500 °C to compare the deformation and fracture behavior with those of the corrosive environment of SCPW. And the specimen geometry effects on the SCC susceptibility and the deformation mechanism in vacuum of ODS steels were investigated by means of slow strain rate test (SSRT) in vacuum and SCPW. The following results are obtained:

1. SCC susceptibility and fracture mode of a 15Cr-4Al-2W ODS ferritic steel in SCPW with different water chemistry.

   (1) The deformation and fracture behavior of the ODS steel are independent of the test conditions, such as strain rate, environment namely vacuum or SCPW and DH/DO contents in SCPW. All the tested specimens shows a ductile fracture showing a cup and corn shape of fractured region.

   (2) The effect of DH and DO contents on the fracture behavior is negligible for the ODS steel.

   (3) The high resolution EPMA observations revealed that oxide layer thickness depends on the DO/DH contents and the thickness of the Cr/Al complex oxide film is thickest for the specimen tested in DH=0.4 ppm. In other words, SCPW dissolved with extremely low

oxygen contents interrupts the creation of the Cr/Al complex oxide layer and gives rise to thicker outer oxide layer in DH = 0.4 ppm and DO & DH < 0.01 ppm.

(4) The detailed EPMA and SEM analysis showed that small "corrosion layer cracking" was observed in the necking region of all the tested specimens except for that tested in vacuum at higher strain rate. The number of the oxide layer cracks was not influenced by the change in the strain rate ranging from 1×10^{-3} s^{-1} to 5×10^{-7} s^{-1}.

(5) The diffusion process of the ODS steel in SCPW follows grain boundary diffusion mechanism. Although grain boundary diffusion, which is faster than the bulk or effective diffusion, was mainly occurred, the thickness of oxide layers on the ODS steel is very thin and similar, regardless of the water chemistry. Therefore, it can be suggested that the grain boundary diffusion mechanism of the 15Cr-4Al ODS steel could be affected by nano-particles and presence of Al-Cr rich complex oxide layer.

(6) After the test in vacuum at a strain rate of 5×10^{-7} s^{-1}, the corrosion layer cracking was observed, indicating that the small amount of oxygen in the vacuum may cause corrosion and corrosion layer cracking in necking area.

(7) The 15Cr-ODS ferritic steel shows no susceptibility to SCC in SCPW in the test condition of this research.

2. The effect of SCPW chemistry on the SCC susceptibility of SUS316L and F82H.

(1) IG-SCC mainly occurred in SUS316L in the SCPW with dissolved hydrogen. On the other hand, the fracture mode at crack initiation stage in SCPW with dissolved oxygen was intermixed with intergranular and transgranular SCC.

(2) Although SUS316L exhibits SCC in SCPW with different water chemistry, the susceptibility to SCC was highest in the water with dissolved hydrogen concentration followed by that in the deaerated SCPW, while SCC was so limited in the water with dissolved oxygen.

(3) In contrast, F82H ferritic/martensitic steel is resistant to SCC in the SCPW dissolved with hydrogen and oxygen in this test condition, while it suffers from much severe oxidation. The surface cracks observed after the test were oxide layer crack limited to the corrosion products.

(4) The SCC of SUS316L in SCPW in this research can be explained by the combination of slip-dissolution model and film-induced cleavage model. The resistance to SCC of F82H ferritic/martensitic steels was explained by crystalline structure of lattice: BCC lattice is less sensitive to SCC through the easiness of cross slip.

(5) It was predictable that the ODS ferritic steel shows better resistant against SCC than the other metallic materials because nano-size oxide particles can trap dislocations by pinning effect,

very fine grain size prevents crack development and ferritic structure is also less sensitive to SCC.

3. The effect of specimen geometry and surface condition on the SCC susceptibility in SCPW

   (1) In the case of austenitic stainless steel and ferritic/martensitic steel, the miniaturized specimen can give reliable deformation and fracture behavior information to the SCC susceptibility by means of SSRT.

   (2) However, ODS steel needs careful consideration of miniaturization and surface finishing in order to evaluate the SCC susceptibility with using SSRT technic.

   (3) Surface roughness or residual stress of ODS steel could be a factor to determine the SCC susceptibility to the SCPW.

4. Deformation mechanism in vacuum of the materials studied in this research as a reference of the experimental data for comparison between vacuum and SCPW.

   (1) The result of SSRT in a vacuum at 773K with the different ODS steels (SOC-9, SOC-14, SOC-16) shows that the lower the strain rate, the lower the tensile strength. However, no material dependence was shown with the tested specimens.

   (2) Tensile yield stress is remarkably dependent on the strain rate, showing a large increase with increasing strain rate, while tensile elongation is not remarkably influenced by strain rate.

   (3) Reduction in area after SSRT in a vacuum at 773K was relatively constant, regardless of strain rate.

   (4) According to the precise observations of fractured surface, there was no strain rate effect on the fracture mode, and only ductile fracture was observed for all the specimens tested in the study. This trend was independent of material.

   (5) The m value in Eq. (2) for the ODS steels was 31 that is very large, implying that the deformation mechanism is related with thermally-activated dislocation motion and/or possibly grain boundary sliding.

The obtained main results of this study are summarized as follows:

   1. Slow strain rate tests in supercritical pressurized water revealed that 15Cr-ODS ferritic steel did not show the susceptibility to SCC at all the test conditions in this study such as strain rate and water chemistry, indicating that all the tested specimens show a ductile fracture with a cup and corn shape of fracture region. Although cracks are observed in the necking

region, the cracks do not affect the tensile properties of ODS ferritic steel because it was revealed, in this study, that the crack development mechanism of the ODS steel is the "corrosion layer cracking" of the very thin oxide film. Therefore, degradation of tensile properties of the ODS steel is only influenced by the thickness of oxide film in the researched water condition.

2. SUS316L austenitic stainless steel exhibits greater susceptibility for SCC than ODS ferritic steel and F82H ferritic/martensitic steel, while it shows good resistance to corrosion. However, SCC susceptibility of SUS316L shows complex behavior to the strain rate change and the different water chemistry. It indicates that water chemistry control is essential for the SUS316L to apply to supercritical water cooled system.

3. Although F82H ferritic/martensitic steel did not show any susceptibility to SCC in SCPW, it severely suffers from oxidation that is inadequately significant for practical applications.

4. Additionally, ODS steel needs careful consideration on the specimen size effect and surface finishing condition in order to evaluate the SCC susceptibility by means of SSRT.

In conclusion, ODS ferritic steel shows no susceptibility to SCC in SCPW and the steel has noticeable feasibility as structural material for application to SCPW cooled nuclear systems, such as SCPW reactor, fusion blanket and also high burn-up light water reactors, where high corrosion resistance and high-temperature strength are simultaneously required.

List of publications

1. <u>Hwanil Je</u>, Akihiko Kimura, "The Strain Rate Effect on High-Temperature Tensile Properties of High-Cr Oxide Dispersion Strengthened Steels", Zero-Carbon Energy Kyoto 2011 Special Edition of Jointed Symposium of Kyoto University Global COE "Energy Science in the Age of Global Warming" and Ajou university BK21, Springer, 347, 2012 pp 329-335.

2. <u>Hwanil Je</u>, Akihiko Kimura, "Stress Corrosion Cracking Susceptibility of Oxide Dispersion Strengthened Ferritic Steel in Supercritical Pressurized Water Dissolved with Different Hydrogen and Oxygen Contents" Corrosion Science, 2013 (in progress)

3. <u>Hwanil Je</u>, Akihiko Kimura, "Effects of Strain Rate on the Tensile and Fracture Behavior of High-Cr ODS Ferritic Steels for Application to Cladding of Fast Reactor" Proceedings of 2013 International Congress on Advances in Nuclear Power Plants (ICAPP2013), The Special Edition for Korean Nuclear Society Journal, 2013 (in press)

4. <u>Hwanil Je</u>, Akihiko Kimura, "Stress corrosion cracking susceptibility of candidate structural materials in supercritical pressurized water" 16th International Conference on Fusion Reactor Materials (ICFRM16), Journal of Nuclear Materials, 2013 (to be submitted)

List of presentations (International conference)

1. <u>Hwan Il Je</u>, Akihiko Kimura, "The Strain Rate Effect on High-Temperature Tensile Properties of High-Cr Oxide Dispersion Strengthened Steels", 3rd G-COE International Symposium (Specially Jointed with BK21 Program at Ajou University) "ZERO CARBON ENERGY 2011" , August 18-19, 2011, Ajou University, Suwon, Korea.

2. <u>H.I. Je</u>, R. Kasada, A. Kimura, "The Effect of Strain Rate on the High Temperature Tensile Properties of ODS Ferritic Steels", 15th International Conference on Fusion Reactor Materials (ICFRM-15), October 16-22, 2011, Hotel Charleston Mariotto, Charleston, SC, USA.

3. <u>Hwanil Je</u>, Akihiko Kimura, "High temperature deformation behavior of ODS and conventional steels at different strain rates", Ajou-KIT-Kyoto University Joint International Symposium, January 31 – February 1, 2012, Uji, Japan.

4. <u>Hwanil Je</u>, Akihiko Kimura, "Deformation and Fracture Behavior of Oxide Dispersion Strengthened Steels in Supercritical Pressurized Water", The 4th International Symposium of Kyoto University G-COE of Energy Science, "Zero-Carbon Energy Kyoto 2012", May 22-23, 2012, Bangkok, Thailand.

5. <u>Hwanil Je</u>, Akihiko Kimura, " Strain rate effect on fracture behavior of ODS steel in super critical water", The 27th Symposium on Fusion Technology, September 24-28, 2012, Liege, Belgium.

6. <u>H.I. Je</u>, A. Kimura, "Strain rate effect on fracture behavior of ODS steel in supercritical pressurized water", The 2nd Japanese-German Workshop on Energy Materials Science, December 11-14, 2012, Karlsruher, Germany.

7. <u>Hwanil Je</u>, Akihiko Kimura, "Effects of Strain Rate on the Tensile and Fracture Behavior of High-Cr ODS Ferritic Steels for Application to Cladding of Fast Reactor", 2013 International Congress on Advances in Nuclear Power Plants (ICAPP2013), May 14-19, 2013, Jeju, Korea.

8. <u>Hwanil Je</u>, Akihiko Kimura, "The effect of Dissolved Hydrogen and Oxygen on Stress Corrosion Cracking Susceptibility of ODS ferritic steel in SCPW", 8th Pacific Rim International Congress on Advanced Materials and Processing (PRICM-8), August 4-9, 2013, Hawaii, USA.

Acknowledgement

First and foremost I would like to express the deepest appreciation to my Ph.D advisor, Professor AKIHIKO KIMURA, for the continuous support of my study and research, for his patience, motivation, enthusiasm, and immense knowledge. Especially, I was fully impressed by his ability to motivation. Without his guidance and persistent help this dissertation would not have been possible.

I would also like to thank the members of my thesis committee, Prof. Konishi, and Prof. Hoshide, for their helpful comments and suggestions.

I have to acknowledge Prof. Kasada, Prof. Iwata and Prof. Morishita for their encouragement and practical advice.

I am deeply grateful to Professor NAM Ki-Woo for his continuous encouragement and guidance to my life.

I would also like to thank to the members of the Kimura lab., (Dr. Noh, Dr. Kim, Dr. Yabuuchi, Dr. Han, Mr. Noto, Ms. Ha, Mr. Yamamoto, Mr. Chen, Mr, Zhang, Mr. Nakagawa, Mr. Takayama, Mr. Himei, Mr. Sakamoto, Mr. Sugino, Mr. Tsuda, Mr. Maekawa, Mr. Murai, Mr. Kubo, Mr. Taniguchi, Mr. Yamaguchi, Mr. Nakasuji, Mr. Okunishi), for their assistances in many aspects. Especially, I must offer my thanks to Dr. Kim Byung-jun and Ms. Ha Yoo-sung for spending time in discussion.

My sincere thanks also goes to Mrs. Wada for offering me so much convenience not only for my academic life but also for life in Japan.

I am also indebted to Japanese teachers, Mrs. Konagai and Mrs. Taniguchi, for their excellent lesson that helped me improve my knowledge in the area of research and also life in Japan.

I appreciate the financial support from the Japanese Government (Monbukagakusho : MEXT) and Global-COE(Centers of Excellence) program that funded parts of the research discussed in this dissertation.

Most importantly, I wish to thank my parents, JE Pan-mo and KIM Soon-nam, and my parents-in-law, LEE Sang-soo and KIM Soon-hee, for unconditional support. Their love provided my inspiration and was my driving force. I owe them everything and wish I could show them just how much I love and appreciate them. I also want to thank to my younger brother, Je Hwan-wook, and sisters-in-laws, Lee So-ra and Lee Bo-ram, for their encouragement and support.

Last but not least, my wife, LEE Bo-kyung, whose love and encouragement allowed me to finish this journey. She already has my heart so I will just give her a heartfelt "thanks." Finally, I would like to express my love to my lovely daughter, JE Yun-ji, for giving me unlimited happiness and pleasure.